NASA/TP - 2020 - 5001740

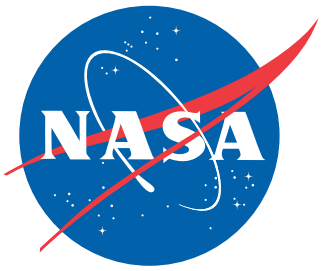

Double-Differential FRaGmentation (DDFRG) Models for Proton and Light Ion Production in High Energy Nuclear Collisions Valid for Both Small and Large Angles

John W. Norbury
Langley Research Center, Hampton, Virginia

May 2020

NASA STI Program . . . in Profile

Since its founding, NASA has been dedicated to the advancement of aeronautics and space science. The NASA scientific and technical information (STI) program plays a key part in helping NASA maintain this important role.

The NASA STI program operates under the auspices of the Agency Chief Information Officer. It collects, organizes, provides for archiving, and disseminates NASA's STI. The NASA STI program provides access to the NTRS Registered and its public interface, the NASA Technical Reports Server, thus providing one of the largest collections of aeronautical and space science STI in the world. Results are published in both non-NASA channels and by NASA in the NASA STI Report Series, which includes the following report types:

- TECHNICAL PUBLICATION. Reports of completed research or a major significant phase of research that present the results of NASA Programs and include extensive data or theoretical analysis. Includes compilations of significant scientific and technical data and information deemed to be of continuing reference value. NASA counter-part of peer-reviewed formal professional papers but has less stringent limitations on manuscript length and extent of graphic presentations.

- TECHNICAL MEMORANDUM. Scientific and technical findings that are preliminary or of specialized interest, e.g., quick release reports, working papers, and bibliographies that contain minimal annotation. Does not contain extensive analysis.

- CONTRACTOR REPORT. Scientific and technical findings by NASA-sponsored contractors and grantees.

- CONFERENCE PUBLICATION. Collected papers from scientific and technical conferences, symposia, seminars, or other meetings sponsored or co-sponsored by NASA.

- SPECIAL PUBLICATION. Scientific, technical, or historical information from NASA programs, projects, and missions, often concerned with subjects having substantial public interest.

- TECHNICAL TRANSLATION. English-language translations of foreign scientific and technical material pertinent to NASA's mission.

Specialized services also include organizing and publishing research results, distributing specialized research announcements and feeds, providing information desk and personal search support, and enabling data exchange services.

For more information about the NASA STI program, see the following:

- Access the NASA STI program home page at http://www.sti.nasa.gov

- E-mail your question to help@sti.nasa.gov

- Phone the NASA STI Information Desk at 757-864-9658

- Write to:
  NASA STI Information Desk
  Mail Stop 148
  NASA Langley Research Center
  Hampton, VA 23681-2199

NASA/TP - 2020 - 5001740

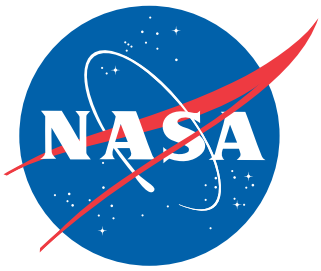

Double-Differential FRaGmentation (DDFRG) Models for Proton and Light Ion Production in High Energy Nuclear Collisions Valid for Both Small and Large Angles

John W. Norbury
Langley Research Center, Hampton, Virginia

National Aeronautics and
Space Administration

Langley Research Center
Hampton, Virginia 23681-2199

May 2020

Acknowledgments

I wish to thank Drs. Charles Werneth, Tony Slaba, Ryan Norman, and Steve Smith for reviewing the manuscript. This work was supported by the Advanced Exploration Systems (AES) Division under the Human Exploration and Operations Mission Directorate of NASA.

Available from:

NASA STI Program / Mail Stop 148
NASA Langley Research Center
Hampton, VA 23681-2199
Fax: 757-864-6500

Contents

List of Tables

List of Figures

Nomenclature

A	Mass number = total number of nucleons (neutrons, protons) in nucleus
α	Alpha (^{4}He) particle symbol
β	Speed
c	Speed of light (units throughout paper are such that $c \equiv 1$)
$\tilde{c}_A$	Constant used for calculation of the coalescence coefficient C_A
C_A	Coalescence coefficient
$\mathcal{C}$	Central fireball rest frame, or general symbol for central region
d	Deuteron (^{2}H) symbol
$\mathcal{D}$	General symbol for direct knockout
E	Total energy
γ	Relativistic factor $\gamma \equiv 1/\sqrt{1-\beta^2}$
h	Helion (^{3}He) symbol
K_1	Modified Bessel function of the second kind
L	Laboratory (lab) rest frame (identical to target rest frame, assuming stationary target)
m_p	Proton mass
N	Normalization constant
Ω	Solid angle
j	Particle (fragment) index
p	Proton symbol
$\mathbf{p}$	3-momentum vector
p	Magnitude of 3-momentum vector $p \equiv \lvert\mathbf{p}\rvert$
$p_{\mathrm{p}L}$	Proton 3-momentum measured in laboratory frame
$\lvert\lvert$	Longitudinal (parallel) component of a vector
$\perp$	Perpendicular component of a vector
$p_{\mathrm{p}L}^{\lvert\lvert}$	Longitudinal (parallel) component of proton 3-momentum measured in laboratory frame
$p_{\mathrm{p}L}^{\perp}$	Transverse component of proton 3-momentum measured in laboratory frame
$\mathcal{P}$	Projectile rest frame, or general symbol for projectile
ϕ	Azimuthal angle
$*$	Arbitrary rest frame (can be $\mathcal{C}, \mathcal{P}, \mathcal{T}$ or L)
σ_p	Total cross-section for proton production
t	Triton (^{3}H) symbol
T	Kinetic energy
$T_{\mathrm{p}L}$	Proton kinetic energy measured in laboratory frame
$\mathcal{T}$	Target rest frame, or general symbol for target
θ	Longitudinal angle
$\theta_{\mathrm{p}L}$	Proton longitudinal angle in laboratory frame
Θ	Temperature

Nomenclature continued

$w_{\mathcal{D}}^{(\mathrm{p})}$	Proton direct production weighting factor
$w_{\mathcal{C}}$	Light ion coalescence weighting factor for central fireball
$w_{\mathcal{D}}$	Light ion coalescence weighting factor for direct production
$w_{\mathcal{P}}$	Light ion coalescence weighting factor for projectile
$w_{\mathcal{T}}$	Light ion coalescence weighting factor for target

Abstract

A new set of Double-Differential FRaGmentation (DDFRG) models for proton and light ion production from high energy nucleus-nucleus collisions, relevant to space radiation, is introduced. The proton model employs thermal production from the projectile, central fireball and target sources, as well as quasi-elastic direct knockout production. The light ion model uses a hybrid coalescence model. The data show a prominent quasi-elastic peak at small angles which becomes highly suppressed at large angles. The models are able to describe this wide range of experimental data with only a limited set of model parameters. Closed-form analytic formulas for double-differential energy and angle cross-sections as well as single-differential spectral cross-sections are developed. These analytic formulas enable highly efficient computation for space radiation transport codes.

1 Introduction

Recent work [1, 2] has shown that neutrons and light ions[1] provide the dominant contribution to space radiation dose equivalent for realistic spacecraft shielding of about 20 g/cm^2 or more. However, comparisons between radiation transport codes [3, 4] and measured data [5] have shown that light ion production represents the largest physics uncertainty in space radiation studies.

Light ions are scattered at both small and large angles, and therefore, double-differential cross-sections for light ion production need to be used as input into three-dimensional transport codes [6, 7, 8, 9, 10], which run most efficiently if simple model cross-section parameterizations are available. Such parameterizations were recently developed [11, 12] and compared very well to experimental cross-section data [13, 14]. However, the experimental data that were used for model comparisons only included light ions scattered at relatively large angles $\geq 10^\circ$, as measured in the laboratory frame. It has been noted that neutron [15] and light ion [16] production cross-sections behave quite differently at very small angles near 0°, displaying a well pronounced quasi-elastic peak at the beam rapidity.

The present work seeks to extend the previously developed models [11, 12] so that they compare well to cross-section data measured at all angles. It will turn out that the most challenging task is to extend the models to account for the quasi-elastic peak at the beam rapidity.

[1]Light ions are defined to be isotopes of Hydrogen (H) and Helium (He); ions heavier than He are called heavy ions. The proton (^{1}H) is a simple light ion. The most important composite light ions are the deuteron (^{2}H $\equiv$ d), triton (^{3}H $\equiv$ t), helion (^{3}He $\equiv$ h), and alpha (^{4}He $\equiv \alpha$). Throughout the text, the term *light ion* will refer to *composite light ion*, unless otherwise noted.

1.1 Review of previously developed models

The main features of the previously developed models [12] were the following:

1. Comparisons of double-differential cross-section data between proton production and light ion production showed that the light ion data were very well represented by scaling the proton data, assuming that light ions are produced via coalescence. These comparisons were done only using experimental proton data versus light ion data; there was no theoretical model used in comparing the proton data to the light ion data, except for a simple scaling of proton data as

$$E_A \frac{d^3\sigma_A}{dp_A^3} = C_A \left(E_{\rm p} \frac{d^3\sigma_{\rm p}}{dp_{\rm p}^3} \right)^A, \qquad \text{with } p_A \equiv A p_{\rm p} \text{ and } E_A \equiv A E_{\rm p}, \tag{1}$$

   where $E_{\rm p}\, d^3\sigma_{\rm p}/dp_{\rm p}^3$ are experimental data[2] for the Lorentz-invariant double-differential cross-section for proton production, and $E_A \frac{d^3\sigma_A}{dp_A^3}$ are experimental data for the Lorentz-invariant double-differential cross-section for light ion production of mass number A. Also, E and $p \equiv |\mathbf{p}|$ are the energy and 3-momentum magnitude of the emitted fragment, and p^3 is the momentum volume element [12]. C_A is the coalescence model coefficient.

2. The empirical relation between proton and light ion data observed in equation (1) implies that it is not necessary to develop a separate theoretical model for light ion production. One only requires a model for proton production. If that proton model compares well to data, then Item 1 implies that the scaled proton model will automatically compare well to light ion data. In other words, the light ion model is obtained simply by scaling the proton model, and this works for *all* composite light ions. A separate light ion model is not required.

3. However, the light ion model is not obtained without some effort. To demonstrate scaling of the experimental data, one typically uses a fitted coalescence coefficient, C_A for each light ion. Therefore, in order to develop a fully predictive model, this coefficient must be calculated with a theoretical model developed separately [12].

4. The only requirement is an accurate proton model: A thermal proton production model was developed [12], with protons being produced from 3 separate sources of projectile, target and central fireball. The thermal model for each source is

$$E_{\rm p} \frac{d^3\sigma_{\rm p}}{dp_{\rm p}^3} = N\, e^{-T_{\rm p}/\Theta}, \tag{2}$$

[2] There are no models or fits to data used here. Only experimental data are used.

where $T_{\rm p}$ is the kinetic energy of the emitted proton[3], Θ is the source temperature and N is a constant. Adding contributions from the 3 sources, Lorentz transforming to the laboratory frame, and inserting the relation between N and the total proton production cross-section $\sigma_{\rm p}$, gives a single formula for the complete proton production cross-section,

$$\begin{aligned} E_{\rm p}\frac{d^3\sigma_{\rm p}}{dp_{\rm p}^3}(p_{{\rm p}L},\theta_{{\rm p}L}) &= \left[E_{\rm p}\frac{d^3\sigma_{\rm p}}{dp_{\rm p}^3}(p_{{\rm p}L},\theta_{{\rm p}L})\right]_{\mathcal{P}} + \left[E_{\rm p}\frac{d^3\sigma_{\rm p}}{dp_{\rm p}^3}(p_{{\rm p}L},\theta_{{\rm p}L})\right]_{\mathcal{C}} \\ &\quad + \left[E_{\rm p}\frac{d^3\sigma_{\rm p}}{dp_{\rm p}^3}(p_{{\rm p}L},\theta_{{\rm p}L})\right]_{\mathcal{T}} \\ &= N_3\Big\{\exp[(m_{\rm p}-\gamma_{\mathcal{P}L}\sqrt{p_{{\rm p}L}^2+m_{\rm p}^2}+\gamma_{\mathcal{P}L}\,\beta_{\mathcal{P}L}\,p_{{\rm p}L}\cos\theta_{{\rm p}L})/\Theta_{\mathcal{P}}] \\ &\quad + \exp[(m_{\rm p}-\gamma_{\mathcal{C}L}\sqrt{p_{{\rm p}L}^2+m_{\rm p}^2}+\gamma_{\mathcal{C}L}\,\beta_{\mathcal{C}L}\,p_{{\rm p}L}\cos\theta_{{\rm p}L})/\Theta_{\mathcal{C}}] \\ &\quad + \exp[(m_{\rm p}-\gamma_{\mathcal{T}L}\sqrt{p_{{\rm p}L}^2+m_{\rm p}^2}+\gamma_{\mathcal{T}L}\,\beta_{\mathcal{T}L}\,p_{{\rm p}L}\cos\theta_{{\rm p}L})/\Theta_{\mathcal{T}}]\Big\}, \end{aligned} \tag{3}$$

with

$$N_3 \equiv \frac{\sigma_{\rm p}}{4\pi m_{\rm p}}\left[\Theta_{\mathcal{P}}\,e^{\frac{m_{\rm p}}{\Theta_{\mathcal{P}}}}\,K_1\left(\frac{m_{\rm p}}{\Theta_{\mathcal{P}}}\right)+\Theta_{\mathcal{C}}\,e^{\frac{m_{\rm p}}{\Theta_{\mathcal{C}}}}\,K_1\left(\frac{m_{\rm p}}{\Theta_{\mathcal{C}}}\right)+\,\Theta_{\mathcal{T}}\,e^{\frac{m_{\rm p}}{\Theta_{\mathcal{T}}}}\,K_1\left(\frac{m_{\rm p}}{\Theta_{\mathcal{T}}}\right)\right]^{-1}. \tag{4}$$

In the above equations, $p_{{\rm p}L}$ and $\theta_{{\rm p}L}$ are the momentum and angle of the proton (p) in the lab frame, L. The proton mass is $m_{\rm p}$. The notation $(p_{{\rm p}L},\theta_{{\rm p}L})$ indicates that the functions must be written as explicit functions of the lab frame L variables $p_{{\rm p}L}$ and $\theta_{{\rm p}L}$ because these are the variables used for the experimental cross-sections, with which the thermal model is to be compared. The projectile, target and central fireball frames are denoted with the symbols $\mathcal{P},\mathcal{T},\mathcal{C}$ respectively. The speed of the projectile frame relative to the lab frame is $\beta_{\mathcal{P}L}$, and the relativistic γ factor is related to the speed via $\gamma = 1/\sqrt{1-\beta^2}$. Similar nomenclature is used for the target and central fireball frames. The projectile, target and central fireball source temperatures are denoted as $\Theta_{\mathcal{P}},\Theta_{\mathcal{T}},\Theta_{\mathcal{C}}$. Also, $K_1\left(\frac{m_{\rm p}}{\Theta}\right)$ is the modified Bessel function of the second kind [18] of order 1 as a function of $\frac{m_{\rm p}}{\Theta}$.

[3]The model of equation (2) is the thermal model evaluated in the frame being considered, namely projectile, fireball or target. Therefore, $T_{\rm p}$ is the kinetic energy of the proton in that frame. The temperatures can also be different in each frame. Each of the 3 expressions for the cross-section is Lorentz-transformed to the lab (target) frame and added together to compare to lab data.

5. The light ion model is simply obtained upon insertion of equation (3) into the right hand side of equation (1), as in[4]

$$
\begin{aligned}
E_A \frac{d^3\sigma_A}{dp_A^3} &= C_A \left\{ \left[E_{\rm p} \frac{d^3\sigma_{\rm p}}{dp_{\rm p}^3}(p_{{\rm p}L}, \theta_{{\rm p}L}) \right]_{\mathcal{P}} + \left[E_{\rm p} \frac{d^3\sigma_{\rm p}}{dp_{\rm p}^3}(p_{{\rm p}L}, \theta_{{\rm p}L}) \right]_{\mathcal{C}} \right. \\
&\qquad \left. + \left[E_{\rm p} \frac{d^3\sigma_{\rm p}}{dp_{\rm p}^3}(p_{{\rm p}L}, \theta_{{\rm p}L}) \right]_{\mathcal{T}} \right\}^A \\
&= C_A N_3^A \left\{ \exp[-(\gamma_{\mathcal{P}L} \sqrt{p_{{\rm p}L}^2 + m_{\rm p}^2} - \gamma_{\mathcal{P}L}\, \beta_{\mathcal{P}L}\, p_{{\rm p}L} \cos\theta_{{\rm p}L} - m_{\rm p})/\Theta_{\mathcal{P}}] \right. \\
&\qquad + \exp[-(\gamma_{\mathcal{C}L} \sqrt{p_{{\rm p}L}^2 + m_{\rm p}^2} - \gamma_{\mathcal{C}L}\, \beta_{\mathcal{C}L}\, p_{{\rm p}L} \cos\theta_{{\rm p}L} - m_{\rm p})/\Theta_{\mathcal{C}}] \\
&\qquad \left. + \exp[-(\gamma_{\mathcal{T}L} \sqrt{p_{{\rm p}L}^2 + m_{\rm p}^2} - \gamma_{\mathcal{T}L}\, \beta_{\mathcal{T}L}\, p_{{\rm p}L} \cos\theta_{{\rm p}L} - m_{\rm p})/\Theta_{\mathcal{T}}] \right\}^A .
\end{aligned}
\tag{5}
$$

1.2 Display of Anderson et al. [16] small angle data

Most of the double-differential cross-section data obtained by Anderson et al. [16] gives particle production as a function of transverse momentum instead of the more intuitive angle variable. The reason for this is because transverse momentum is Lorentz invariant, whereas angle is not. The use of transverse momentum presents significant complications when trying to analyze and compare theoretical models written in terms of angle, and a major effort was undertaken to transform the transverse momentum variables to angle variables, as discussed in the Appendix of Section 7. Even though it is simple to produce transverse momentum variables from theoretical models [12], the use of angle variables is much more intuitive and gives much better insight into the behavior of both the data and the models, at least as far as space radiation applications are concerned.

Transverse momentum, $p^\perp$, is defined as $p^\perp \equiv p \sin\theta$, where p is the total momentum. Inverting gives $\theta = \arcsin(p^\perp/p)$, which is a double-valued function in the range 0° - 180°. If p is fixed, then θ has two values (forward and backward) for a single value of $p^\perp$. With p varying, then a single value of transverse momentum contains a variety of different angles. For example, a single transverse momentum value might contain all the angles 1°, 1.4°, 1.6°, 1.7°, 1.8°, 2.0°, 2.3°, 2.4°, 2.5°, 2.7°, 3.0°, 3.2°, 3.5°, 3.8°, etc. However, one wishes to plot cross-sections as a function of angle, for all particles produced at 1° and at 2° and 3° and 4°, etc. The way this is done in the present work is as follows: Data labeled 1° will actually include, for example, 1°, 1.4°, 1.6°, 1.7°, 1.8°. Data labeled 2° will include 2.0°,

[4]The physical interpretation of raising the proton cross-section to the power A is as follows: As with the previous model [11, 12], the complete proton cross-section is raised to the power A, and so there will be coalescence contributions coming not only from the various different sources, but also from "cross" terms. Consider, for example, deuteron (i.e. bound state of a proton and neutron) coalescence formation. Both the proton and neutron can come from the same central fireball source, for example. But due to the cross terms, a proton could come from the central fireball and coalesce with a neutron from the projectile.

2.3°, 2.4°, 2.5°, 2.7°. Data labeled 3° will include 3.0°, 3.2°, 3.5°, 3.8°, etc. This is an accurate representation, because variation of the data over one degree ranges is negligible.

Strictly speaking, it is not correct to convert the $p^{\perp}$ data of Anderson et al. [16] to angle. This is because, for a fixed value of p, there are two values of angle for each single value of $p^{\perp}$, as mentioned above. However, the Anderson et al. [16] data is restricted to small values of $p^{\perp}$, corresponding to small angle values in the range 0° - 10°. Therefore, the second corresponding backward angles are 170° - 180°, and the Lorentz-invariant double-differential cross-sections at these backward angles are so small as to be negligible, *for the range of p values* reported by Anderson et al. [16]. Therefore, it is a very good approximation to convert the $p^{\perp}$ data of Anderson et al. [16] to angle, because only small forward angles make significant contributions to the cross-sections.

2 Coalescence scaling of small angle data

The key to the success of the previously developed light ion model was due to the fact that the light ion data could be very well reproduced simply by scaling proton data. This meant that one only needed to develop a single proton model: The light ion model was obtained simply by scaling the proton model, in the same way as the data scaled. Data analyzed previously was limited to large angles. The key question is the following: Do the proton and light ion data also exhibit simple scaling at small angles? The answer will turn out to depend on the type of projectile.

Figures 1 - 7 (reproduced from reference [12]) show proton (blue) and light ion (black) production cross-section data [13, 14] for large angles. The proton data is scaled according to equation (1) and shown as the red points. As discussed previously [12], one can see the remarkable results of the coalescence idea; the scaled proton data (red) lies directly on top of the experimental light ion data (black).

The overlap of scaled proton data (red) on top of light ion data (black) seems miraculous. The blue proton curves move to the right (becoming the red curves) comes about because of the definitions in equation (1), namely that $p_A \equiv Ap_{\rm p}$ and $E_A \equiv AE_{\rm p}$. But this is really only a choice of units. In Figures 1 - 7, the light ion momentum p_A is in units of GeV; because those are units in which data were originally given [13, 16].

Units of GeV/n are preferred, because they clearly show the similarity of the behavior of the light ion and proton data. Later when examining the quasi-elastic peaks, it will be seen that the peak of the light ion data is far removed from the proton peak using GeV units. However, with GeV/n units, both peaks will lie on top of each other leading to much better physical insight important for model development. Therefore, the experimental proton and light ion data and also the scaled proton data from Figures 1 - 7 are re-plotted using units of GeV/n and are shown in Figures 8 - 14. The units of the vertical axes have also been modified to include GeV/n. Of course, the comparison of the scaled proton data with the light ion data are just as accurate as before, but now, with GeV/n

units, the scaling behavior seems less miraculous because one observes that the shapes of the proton and light ion data are similar and certainly have similar high momentum fall-offs. Scaling the proton data by a single coalescence coefficient (and raising to a power) to reproduce light ion data now seems more obvious. However, the use of a *single* coalescence coefficient to describe all angles of a given light ion[5] remains remarkable.

The data [13, 14] discussed so far has been for relatively large angles $\geq 10^\circ$. Now examine the small angle data of Anderson et al. [16], which is plotted in Figures 15 - 17, with units of GeV and in Figures 18 - 20, with units of GeV/n. For the moment, just focus on the proton (blue) and light ion (black) data and ignore the scaled data (red). The most obvious new feature of the data is the *appearance of a large peak, especially at the smallest angles.* As the angle gets larger the shape of the Anderson et al. data [16] becomes similar in shape to the Nagamiya data [13, 14]. Another obvious feature shown in Figures 18 - 20, is that in units of GeV/n, the *light ion and proton data have a peak at the same momentum per nucleon.* The small angle data has also been scaled according to the coalescence scaling of equation (1). The scaled data appear as red points in Figures 15 - 20. It can be seen that *coalescence scaling fails for small angles!*

All data discussed so far has involved heavy ion projectiles producing light ions. Anderson et al. [16] have also measured light ion fragments from *light ion projectiles* at the very smallest angle of 0°. However, ^{4}He was the only light ion projectile used, but, fortunately this is the most important composite light ion projectile [17] for space radiation applications. The data are shown in Figure 21 in units of GeV, and in Figure 22 in units of GeV/n. Again, a large peak is observed at 0°, with both the light ion and proton data showing the peak at the same momentum per nucleon. However, this time *for light ion projectiles, coalescence scaling works again!*

The small angle Anderson data [16] that shows failure of coalescence scaling is shown as a function of angle in Figures 15 - 20. However, as mentioned in Section 1.2, the data were measured as a function of transverse momentum, and not angle. This will alter the conclusions about the failure of coalescence scaling, and this is verified in Figures 23 - 25, which are shown as a function of transverse momentum, instead of angle, in units of GeV, and in Figures 26 - 28 in units of GeV/n. The α + C reactions shown in Figures 21 - 22 are at an angle of 0° corresponding exactly to a single value $p^\perp \equiv p \sin\theta = 0$, regardless of the value of p, and thereby not requiring separate transverse momentum plots.

In summary, the small angle data [16] display the following four new features:

1. A large peak appears at the smallest angles.

2. The light ion and proton data have a peak at the same momentum per nucleon.

3. Coalescence scaling fails for small angle fragments with heavy ion projectiles.

4. Coalescence scaling is valid for small angle fragments with light ion projectiles.

[5]Each light ion has a different coefficient, which remains constant, independent of angle.

The previously developed thermal/coalescence model [11, 12] included a 3-source thermal proton production model, which was then scaled according to coalescence to give the light ion model. The thermal/coalescence model described the large angle data [13, 14] very well. There are major difficulties in extending the previous model to the small angle data set. Firstly, the 3-source thermal proton model cannot describe the quasi-elastic peak observed at small angles. Secondly, even if the 3-source thermal proton model could describe the peak, the model still cannot be scaled with coalescence, because the data, as seen in Figures 15 - 20 and 23 - 28, show that coalescence scaling fails at small angles. Thirdly, even if one could somehow devise a successful light ion model, which does not rely on coalescence scaling, the model would fail for light ion projectiles, because coalescence scaling reverts to being mysteriously valid for light ion projectiles producing small angle fragments. A major effort is required to extend the previous model [12] to describe both small and large angle data for both light and heavy projectiles. The new model must be capable of describing the four new small angle features discussed above, as well as re-produce the previous [11, 12] successful description of the large angle data. That is the subject of the present work.

3 New Models

What is the origin of the new peak seen at small angles, and how does one develop an appropriate model to describe it? Figures 18 - 20 and 22, *plotted in units of GeV/n* give the main clue. It can be seen that all the light ion peaks occur at the same lab momentum per nucleon, and the value of that lab momentum per nucleon is the same as the proton peak. The Einstein relations are

$$E \equiv T + m = \gamma m, \tag{6}$$

and

$$E^2 \equiv \mathbf{p}^2 + m^2, \tag{7}$$

where E is the total energy, T is the kinetic energy, and m is the mass. A convention in the present work is $p \equiv |\mathbf{p}|$. Units are chosen with the speed of light $c \equiv 1$; this standard convention is used throughout this paper. A projectile kinetic energy $T = 1.05$ GeV/n, gives a lab momentum of $p = 1.75$ GeV/n, which is precisely the location of all the peaks in Figures 18 - 20 and 22. *Therefore, the small angle peaks must be due to fragments knocked directly out of the projectile.* An *elastic* process is one in which the projectile undergoes no interactions and continues on with its original kinetic energy after the reaction[6]. The direct knockout of fragments with the same[7] kinetic energy as the

[6]This assumes that no energy is transferred to the target, or equivalently represents the limit of an infinitely massive target. In reality, some energy can be transferred.

[7]Again assume no energy transfer to the target.

original projectile is called *quasi-elastic*. Figures 18 - 20 and 22 show that the small angle peaks are due to quasi-elastic direct knockout. This is in contrast to the large angle data, where the fragments arise from a hot thermal source which decays after reaching thermal equilibrium. As discussed previously, there are 3 thermal sources, namely a source in the projectile, a source in the target and a much hotter fireball source near the center of momentum.

3.1 New proton thermal plus direct knockout model

3.1.1 Maxwellian versus Gaussian distribution

The general form of a Gaussian distribution, also often called a Normal distribution, is

$$f(x) = \frac{1}{\tilde{\sigma}\sqrt{2\pi}}\, e^{-(x-\nu)^2/2\tilde{\sigma}^2}, \tag{8}$$

where x is the variable value, $f(x)$ is the probability distribution function, $\tilde{\sigma}$ is the standard deviation of x, and ν is the mean value of x. In terms of a momentum distribution p, where p is the magnitude of the 3-momentum $p \equiv |\mathbf{p}|$, with an average value $\nu = 0$, the distribution is [19, 20, 21]

$$f_{\rm G}(p) = \frac{1}{\tilde{\sigma}\sqrt{2\pi}}\, e^{-p^2/2\tilde{\sigma}^2}. \tag{9}$$

The relativistic kinetic energy can be expanded as a power series in the momentum,

$$T = \frac{p^2}{2m}(1 - \frac{p^2}{4m_j^2} + \cdots) \tag{10}$$

with the first term corresponding to the non-relativstic approximation

$$T_{\rm NR} \approx \frac{p^2}{2m}. \tag{11}$$

The thermal Maxwellian distribution is

$$f_{\rm M}(p) = Ne^{-T/\Theta}, \tag{12}$$

with normalization constant N, and temperature Θ. Comparison of equations (9) and (12) shows that a *Gaussian (Normal) distribution is equivalent to a Maxwell distribution in the non-relativistic approximation.* The Maxwell temperature is trivially related to the Gaussian distribution width, or standard deviation, $\tilde{\sigma}$. One often sees Gaussian distributions [19, 20, 21, 22] used for the momentum distributions of fragments, including direct knockout of neutrons [15, 22], and Maxwell distributions [13, 22] used for thermal decay of hot sources, but because these descriptions are equivalent at the non-relativistic level, either formalism can be used. Therefore, the present work will use thermal Maxwell distributions for all fragment production including both thermal sources and direct knockout sources. The temperature used for the direct knockout source can be regarded as an "effective" temperature.

3.1.2 Thermal plus direct knockout proton model

A new thermal plus direct knockout model for proton production is now developed in direct analogy to the previously developed model of reference [12]. The new model also uses some of the methods developed to describe neutron production cross-sections [15, 22, 23, 24, 25, 26], where a total of 4 sources were used corresponding to 3 thermal sources of projectile, target and fireball and an additional source due to direct ($\mathcal{D}$) knockout from the projectile. Cross-sections for protons from the 4 sources are added together as

$$\begin{aligned} E_{\rm p}\frac{d^3\sigma_{\rm p}}{dp_{\rm p}^3}(p_{{\rm p}L},\theta_{{\rm p}L}) &= \left[E_{\rm p}\frac{d^3\sigma_{\rm p}}{dp_{\rm p}^3}(p_{{\rm p}L},\theta_{{\rm p}L})\right]_{\mathcal{P}} + \left[E_{\rm p}\frac{d^3\sigma_{\rm p}}{dp_{\rm p}^3}(p_{{\rm p}L},\theta_{{\rm p}L})\right]_{\mathcal{C}} \\ &\quad + \left[E_{\rm p}\frac{d^3\sigma_{\rm p}}{dp_{\rm p}^3}(p_{{\rm p}L},\theta_{{\rm p}L})\right]_{\mathcal{T}} + w_{\mathcal{D}}^{({\rm p})}\left[E_{\rm p}\frac{d^3\sigma_{\rm p}}{dp_{\rm p}^3}(p_{{\rm p}L},\theta_{{\rm p}L})\right]_{\mathcal{D}} \\ &= N_4\left[e^{-T_{{\rm p}\mathcal{P}L}/\Theta_{\mathcal{P}}} + e^{-T_{{\rm p}\mathcal{C}L}/\Theta_{\mathcal{C}}} + e^{-T_{{\rm p}\mathcal{T}L}/\Theta_{\mathcal{T}}} + w_{\mathcal{D}}^{({\rm p})}\, e^{-T_{{\rm p}\mathcal{P}L}/\Theta_{\mathcal{D}}}\right], \end{aligned} \tag{13}$$

where $\mathcal{P}$, $\mathcal{C}$, $\mathcal{T}$, $\mathcal{D}$ symbols representing projectile, central fireball, target, and direct knockout respectively, and $w_{\mathcal{D}}^{({\rm p})}$ is the direct knockout weighting value listed in Table 1. The kinetic energy of the proton in the projectile frame relative to the lab frame is denoted as $T_{{\rm p}\mathcal{P}L}$, and similarly for the other frames. Note that $T_{{\rm p}\mathcal{P}L}$ also appears in the direct term because it originates from the projectile. Following the methods of reference [12] and inserting Lorentz transformations gives

$$\begin{aligned} E_{\rm p}\frac{d^3\sigma_{\rm p}}{dp_{\rm p}^3}(p_{{\rm p}L},\theta_{{\rm p}L}) &= N_4\Big\{\exp[(m_{\rm p} - \gamma_{\mathcal{P}L}\sqrt{p_{{\rm p}L}^2+m_{\rm p}^2} + \gamma_{\mathcal{P}L}\,\beta_{\mathcal{P}L}\,p_{{\rm p}L}\cos\theta_{{\rm p}L})/\Theta_{\mathcal{P}}] \\ &\quad + \exp[(m_{\rm p} - \gamma_{\mathcal{C}L}\sqrt{p_{{\rm p}L}^2+m_{\rm p}^2} + \gamma_{\mathcal{C}L}\,\beta_{\mathcal{C}L}\,p_{{\rm p}L}\cos\theta_{{\rm p}L})/\Theta_{\mathcal{C}}] \\ &\quad + \exp[(m_{\rm p} - \gamma_{\mathcal{T}L}\sqrt{p_{{\rm p}L}^2+m_{\rm p}^2} + \gamma_{\mathcal{T}L}\,\beta_{\mathcal{T}L}\,p_{{\rm p}L}\cos\theta_{{\rm p}L})/\Theta_{\mathcal{T}}] \\ &\quad + w_{\mathcal{D}}^{({\rm p})}\exp[(m_{\rm p} - \gamma_{\mathcal{P}L}\sqrt{p_{{\rm p}L}^2+m_{\rm p}^2} + \gamma_{\mathcal{P}L}\,\beta_{\mathcal{P}L}\,p_{{\rm p}L}\cos\theta_{{\rm p}L})/\Theta_{\mathcal{D}}]\Big\}. \end{aligned} \tag{14}$$

In terms of the projectile kinetic energy, $T_{\mathcal{P}L}$, the relativistic factors are

$$\gamma_{\mathcal{P}L} = 1 + \frac{T_{\mathcal{P}L}}{m_n}, \qquad \gamma_{\mathcal{C}L} = \sqrt{1+\frac{T_{\mathcal{P}L}}{2m_n}}, \qquad \gamma_{\mathcal{T}L} = 1, \qquad \beta = \sqrt{1-\frac{1}{\gamma^2}}. \tag{15}$$

Equation (14) represents the thermal plus direct knockout model with contributions from the projectile, target and central sources, all Lorentz-transformed to the lab frame.

The normalization coefficient N_4 is obtained from the requirement that the total proton production cross-section $\sigma_{\rm p}$ is the fully integrated differential cross-section. Using the

methods of reference [12], the new normalization becomes

$$N_4 = \frac{\sigma_{\rm p}}{4\pi m_{\rm p}}\left[\Theta_{\mathcal{P}}\, e^{\frac{m_{\rm p}}{\Theta_{\mathcal{P}}}}\, K_1\left(\frac{m_{\rm p}}{\Theta_{\mathcal{P}}}\right) + \Theta_{\mathcal{C}}\, e^{\frac{m_{\rm p}}{\Theta_{\mathcal{C}}}}\, K_1\left(\frac{m_{\rm p}}{\Theta_{\mathcal{C}}}\right) + \Theta_{\mathcal{T}}\, e^{\frac{m_{\rm p}}{\Theta_{\mathcal{T}}}}\, K_1\left(\frac{m_{\rm p}}{\Theta_{\mathcal{T}}}\right) + w_{\mathcal{D}}^{(\rm p)}\, \Theta_{\mathcal{D}}\, e^{\frac{m_{\rm p}}{\Theta_{\mathcal{D}}}}\, K_1\left(\frac{m_{\rm p}}{\Theta_{\mathcal{D}}}\right)\right]^{-1}. \quad (16)$$

Equations (14) and (16) represent the final 4-source thermal proton model in terms of lab variables, and correctly normalized so that the integral of the Lorentz-invariant differential cross-section gives the total cross-section.

3.2 New light ion hybrid coalescence model

The results of Section 2 clearly showed that fragment cross-sections produced at small angles for heavy projectiles do not obey the simple scaling behavior as predicted in the coalescence model. Nevertheless, a hybrid scaling model can still be developed. Auble et al. [27] were among the first to show that fragment cross-sections could be described by multiple sources, although they considered only the two fireball and projectile sources. They also used scaling, but weighted each contribution to scaling differently, which required the use of more adjustable parameters. Neutron production work [15, 22, 23, 24, 25, 26], also made use of different adjustable parameter weight factors for each source.

3.2.1 $(p_{{\rm p}L}, \theta_{{\rm p}L})$ variables

The new hybrid scaling model is (with $p_A \equiv Ap_{\rm p}$ and $E_A \equiv AE_{\rm p}$)

$$E_A\frac{d^3\sigma_A}{dp_A^3} = C_A\left\{w_{\mathcal{P}}\left[E\frac{d^3\sigma}{dp^3}(p_{{\rm p}L},\theta_{{\rm p}L})\right]_{\mathcal{P}} + w_{\mathcal{C}}\left[E\frac{d^3\sigma}{dp^3}(p_{{\rm p}L},\theta_{{\rm p}L})\right]_{\mathcal{C}} + w_{\mathcal{T}}\left[E\frac{d^3\sigma}{dp^3}(p_{{\rm p}L},\theta_{{\rm p}L})\right]_{\mathcal{T}} + w_{\mathcal{D}}\left[E\frac{d^3\sigma}{dp^3}(p_{{\rm p}L},\theta_{{\rm p}L})\right]_{\mathcal{D}}\right\}^A, \quad (17)$$

This equation is very similar to the coalescence scaling model in equations (1) and (5), except that now adjustable weighting factors w are used for all sources. This is why it is called a hybrid coalescence model. Substituting equation (14) into (17) gives the final result for the light ion hybrid scaling model in terms of $(p_{{\rm p}L}, \theta_{{\rm p}L})$ variables

$$\begin{aligned} E_A\frac{d^3\sigma_A}{dp_A^3} = {} & C_A N_4^A\left\{w_{\mathcal{P}}\exp[(m_{\rm p} - \gamma_{\mathcal{P}L}\sqrt{p_{{\rm p}L}^2+m_{\rm p}^2} + \gamma_{\mathcal{P}L}\,\beta_{\mathcal{P}L}\,p_{{\rm p}L}\cos\theta_{{\rm p}L})/\Theta_{\mathcal{P}}]\right. \\ & + w_{\mathcal{C}}\exp[(m_{\rm p} - \gamma_{\mathcal{C}L}\sqrt{p_{{\rm p}L}^2+m_{\rm p}^2} + \gamma_{\mathcal{C}L}\,\beta_{\mathcal{C}L}\,p_{{\rm p}L}\cos\theta_{{\rm p}L})/\Theta_{\mathcal{C}}] \\ & + w_{\mathcal{T}}\exp[(m_{\rm p} - \gamma_{\mathcal{T}L}\sqrt{p_{{\rm p}L}^2+m_{\rm p}^2} + \gamma_{\mathcal{T}L}\,\beta_{\mathcal{T}L}\,p_{{\rm p}L}\cos\theta_{{\rm p}L})/\Theta_{\mathcal{T}}] \\ & \left. + w_{\mathcal{D}}w_{\mathcal{D}}^{(\rm p)}\exp[(m_{\rm p} - \gamma_{\mathcal{P}L}\sqrt{p_{{\rm p}L}^2+m_{\rm p}^2} + \gamma_{\mathcal{P}L}\,\beta_{\mathcal{P}L}\,p_{{\rm p}L}\cos\theta_{{\rm p}L})/\Theta_{\mathcal{D}}]\right\}^A. \end{aligned} \quad (18)$$

3.2.2 $(p_{\mathrm{p}L}, p_{\mathrm{p}L}^{\perp})$ variables

As discussed in the Appendix, the transverse momentum, $p_{\mathrm{p}L}^{\perp}$, is a double valued function of angle $\theta_{\mathrm{p}L}$: Two different angles correspond to the same value of transverse momentum. One angle is in the forward (+) direction and the other is in the backward (−) direction. Let $*$ be an arbitrary reference frame (either projectile, target, fireball). The proton cross-sections in the $*$ frame are added incoherently,

$$E\frac{d^3\sigma_{*p}}{dp^3}(p_{\mathrm{p}L}, p_{\mathrm{p}L}^{\perp}) = E\frac{d^3\sigma_{*p}^{+}}{dp^3}(p_{\mathrm{p}L}, p_{\mathrm{p}L}^{\perp}) + E\frac{d^3\sigma_{*p}^{-}}{dp^3}(p_{\mathrm{p}L}, p_{\mathrm{p}L}^{\perp}), \tag{19}$$

to form the complete cross-section corresponding a specific value of $p_{\mathrm{p}L}^{\perp}$.

Equation (17) contains cross terms, so that coalesced light ions can receive contributions, for example, not only from a single reference frame, but also different reference frames. For example, a deuteron can be formed from two nucleons both originating in the projectile, but also can be formed from a nucleon in the projectile coalescing with a nucleon from the target. This makes sense physically. However, it does *not* make sense to allow for cross terms from the forward and backward directions. Define the double valued light ion cross-section

$$\begin{aligned} E_A\frac{d^3\sigma_A^{\pm}}{dp_A^3}(p_{\mathrm{p}L}, p_{\mathrm{p}L}^{\perp}) \;\equiv\; & C_A\left\{w_{\mathcal{P}}\left[E\frac{d^3\sigma^{\pm}}{dp^3}(p_{\mathrm{p}L}, p_{\mathrm{p}L}^{\perp})\right]_{\mathcal{P}} + w_{\mathcal{C}}\left[E\frac{d^3\sigma^{\pm}}{dp^3}(p_{\mathrm{p}L}, p_{\mathrm{p}L}^{\perp})\right]_{\mathcal{C}}\right. \\ & \left. + w_{\mathcal{T}}\left[E\frac{d^3\sigma^{\pm}}{dp^3}(p_{\mathrm{p}L}, p_{\mathrm{p}L}^{\perp})\right]_{\mathcal{T}} + w_{\mathcal{D}}\left[E\frac{d^3\sigma^{\pm}}{dp^3}(p_{\mathrm{p}L}, p_{\mathrm{p}L}^{\perp})\right]_{\mathcal{D}}\right\}^A, \end{aligned} \tag{20}$$

to give the light ion transverse momentum cross-section

$$\begin{aligned} E_A\frac{d^3\sigma_A}{dp_A^3}(p_{\mathrm{p}L}, p_{\mathrm{p}L}^{\perp}) \;=\; & E_A\frac{d^3\sigma_A^{+}}{dp_A^3}(p_{\mathrm{p}L}, p_{\mathrm{p}L}^{\perp}) + E_A\frac{d^3\sigma_A^{-}}{dp_A^3}(p_{\mathrm{p}L}, p_{\mathrm{p}L}^{\perp}) \\ \;=\; & C_A\left\{w_{\mathcal{P}}\left[E\frac{d^3\sigma^{+}}{dp^3}(p_{\mathrm{p}L}, p_{\mathrm{p}L}^{\perp})\right]_{\mathcal{P}} + w_{\mathcal{C}}\left[E\frac{d^3\sigma^{+}}{dp^3}(p_{\mathrm{p}L}, p_{\mathrm{p}L}^{\perp})\right]_{\mathcal{C}}\right. \\ & \left. + w_{\mathcal{T}}\left[E\frac{d^3\sigma^{+}}{dp^3}(p_{\mathrm{p}L}, p_{\mathrm{p}L}^{\perp})\right]_{\mathcal{T}} + w_{\mathcal{D}}\left[E\frac{d^3\sigma^{+}}{dp^3}(p_{\mathrm{p}L}, p_{\mathrm{p}L}^{\perp})\right]_{\mathcal{D}}\right\}^A \\ & + C_A\left\{w_{\mathcal{P}}\left[E\frac{d^3\sigma^{-}}{dp^3}(p_{\mathrm{p}L}, p_{\mathrm{p}L}^{\perp})\right]_{\mathcal{P}} + w_{\mathcal{C}}\left[E\frac{d^3\sigma^{-}}{dp^3}(p_{\mathrm{p}L}, p_{\mathrm{p}L}^{\perp})\right]_{\mathcal{C}}\right. \\ & \left. + w_{\mathcal{T}}\left[E\frac{d^3\sigma^{-}}{dp^3}(p_{\mathrm{p}L}, p_{\mathrm{p}L}^{\perp})\right]_{\mathcal{T}} + w_{\mathcal{D}}\left[E\frac{d^3\sigma^{-}}{dp^3}(p_{\mathrm{p}L}, p_{\mathrm{p}L}^{\perp})\right]_{\mathcal{D}}\right\}^A, \end{aligned} \tag{21}$$

which contains no unphysical cross terms relating forward and backward angles.

3.3 Verification

A variety of verification tests were undertaken to ensure that the computer codes and mathematical formulas were correct. These tests are listed below.

- Computer codes were originally written in *Mathematica*. Independent codes were also written in *FORTRAN* and both codes were verified to be giving the same results.

- As described perviously, all differential cross-sections were written in terms of two independent sets of variables, namely momentum and angle, (p, θ), and also momentum and transverse momentum, $(p, p^{\perp})$. Given that $p^{\perp} \equiv p \cos\theta$, values of θ can be chosen and the corresponding value of $p^{\perp}$ can be calculated. Because $E\frac{d^3\sigma}{dp^3}$ is Lorentz invariant, the values should be the same in the different variable sets, and this was verified for a variety of cases. These tests also verified that the double valued cross-section functions introduced for transverse momentum variables (see Appendix) were correct.

- As described previously, there are three different reference frames used to implement the theoretical models, namely projectile, central fireball, and target (lab) frames. The thermal and coalescence models are calculated in each frame and then Lorentz-transformed to the lab frame in which experimental measurements are available and in which transport codes are evaluated. The differential cross-sections, $E\frac{d^3\sigma}{dp^3}$, are Lorentz-invariant, but $\frac{d^2\sigma}{dEd\Omega}$ and $\frac{d\sigma}{dE}$ are not Lorentz-invariant. How is one to check that the complicated set of Lorentz-transformations to the lab frame have been done correctly? This includes the complications of the two variable sets above. The most powerful test is to fully integrate all differential cross-sections over energy and angle to obtain the total cross-section σ, which *is* Lorentz-invariant. All the various differential cross-sections should give the same answer σ when they are integrated. Extensive verification tests were done, giving high confidence that all Lorentz-transformations and resulting formulas for differential cross-sections, including the analytic formulas described in Sections 5, are correct.

4 Validation: Models compared to experimental data

The new theoretical models developed in this work will now be compared to both the large angle data of Nagamiya et al. [13, 14], as well as the small angle data of Anderson et al. [16]. All of the Nagamiya et al. data was examined previously [13, 14], but only with the 3-source model, which was found to be in good agreement. The challenge of the present work is for the new models, which include the addition of a 4th direct knockout source, to maintain the previously observed good agreement with Nagamiya et al. [13, 14], as well as correctly predict the small angle Anderson et al. data [16], which has not yet been analyzed with these models.

The total cross-section, σ, is calculated from the NUCFRG3 model [28] with values listed in Table 2. Any other model, such as RAADFRG [29], could alternatively be used. Values for the coalescence coefficients are listed in Table 3.

4.1 Large angle data of Nagamiya et al. [13, 14]

4.1.1 Proton model compared to large angle data

The new proton thermal plus direct knockout 4-source model is now compared to the large angle data of Nagamiya et al. [13, 14], which was analyzed previously [11, 12] with the simpler 3-source thermal model.

Results for proton production are shown in Figures (29) - (30) for Ar + KCl and C + C, both with projectile kinetic energies of 800 MeV/n. The figures show contributions from the 4 individual sources which add together to form the total (red curve) according to equations (13) and (14). Comparisons with data are of the same good quality as reported previously with the simpler 3-source model [11, 12]. The key observation is the contribution of the direct knockout source, shown as the magenta curve in the figures. Direct knockout only makes large contributions at very small angles and is visible only at 10° for the Ar + KCl reaction, as the small magenta peak occurring at the projectile momentum. The width of the peak is narrow because of the small temperature (2.8 MeV) assigned to direct knockout discussed previously. For angles larger than 10° for Ar + KCl and for all angles for C + C, the direct knockout contribution is not visible because it is so small at these large angles. All of this makes sense physically: Direct knockout fragmentation products should continue in the forward direction at the same energy as the incident projectile. Direct knockout is highly suppressed as the angle increases. Thus, the new 4-source model is able to retain the success of the previous 3-source model for large angle data because the addition of the new direct source is highly suppressed at large angles.

4.1.2 Light ion model compared to large angle data

The new light ion hybrid coalescence 4-source model is now compared to the large angle data of Nagamiya et al. [13], which was analyzed previously [11, 12] with the simpler 3-source coalescence model.

Results for light ion production are shown in Figures (31) - (37) for Ar + KCl and C + C, both with projectile kinetic energies of 800 MeV/n. The figures show contributions from the 4 individual sources which, rather than simple addition, add according to equations (17) and (18) to form the total (red curve). As with the proton case, the direct knockout term mainy contributes at very small angles and is highly suppressed at the large angles represented by this data. In fact, it is so small as to not be visible in any of the light ion large angle figures.

For light ions, there are more parameters for the new 4-source model, as compared to the previous 3-source model. These were discussed previously and the weighting factor parameters are listed in Tables 4 and 5. With more parameters, better agreement with data is expected and this is seen in several of the figures, especially for t, h, α light ion production at 15° for both Ar + KCl (Figures 32, 33, 34) and C + C (Figures 36, 37), which now show much better agreement with 15° data compared to previous work [11]. This improved agreement is useful in space radiation applications, where the larger cross-sections at the smaller angles produce more contribution to dose. Of course, it is essential at the very small angles to be discussed next.

4.2 Small angle data of Anderson et al. [16]

4.2.1 Proton model compared to small angle data

The new proton thermal plus direct knockout 4-source model is now compared to the small angle data of Anderson et al. [16]. Although not shown graphically, the previously developed simpler 3-source model [11, 12] completely fails to describe the small angle data [16], which is why the new 4-source model was developed.

Results for proton production in C + C reactions at 1.05 GeV/n are shown in Figure 38 as a function of angle, and in Figure 39 as a function of transverse momentum. Results for proton production in α + C reactions at 1.05 GeV/n are shown in Figure 40 (top left panel) at an angle of 0°. The figures show contributions from the 4 individual sources which add together to form the total (red curve) according to equations (13) and (14).

The direct knockout contribution of the 4-source model is now clearly evident as the narrow magenta peak at the projectile momentum making a dominant contribution at the smallest angles. Overall, the agreement with heavy ion projectile data as a function of angle (Figure 38) and also as a function of transverse momentum (Figure 39) is very good. The models clearly show the steep drop in cross-section magnitude and shape as the angle gets larger. Also, even though the data is limited, the agreement with the light ion α projectile data at 0° in Figure 40 (top left panel) is also very good.

4.2.2 Light ion model compared to small angle data

The new light ion hybrid coalescence 4-source model is now compared to small angle data of Anderson et al. [16], which was not previously analyzed with these models. Although not shown here, the previously developed simpler 3-source model [11, 12] completely fails to describe the small angle data [16], which is why the new 4-source model was developed.

Results for light production in C + C reactions at 1.05 GeV/n are shown in Figures 41 - 43 as a function of angle, and again in Figures 44 - 46 as a function of transverse momentum. Results for light production in α + C reactions at 1.05 GeV/n are shown in Figure 40 at an angle of 0°. The figures show contributions from the 4 individual sources

which, rather than simple addition, add according to equation (17) and (18) to form the total (red curve).

The quality of agreement between models and data is similar to the proton small angle case, with overall very good agreement and a clear contribution of direct knockout at the smallest angles, with increasing suppression as the angle increases. Of course, the overall good agreement is not only due to the physical basis of the models, but also the choice of parameters, which were adjusted to give the best agreement. Nevertheless, it is quite remarkable that such a wide range of data, as shown in all the figures, agrees with the 4-source model and a limited parameter set.

5 Differential cross-sections for transport codes

The light ion differential cross-section models developed in the present work are intended for use in the 3-dimensional, deterministic transport code called 3DHZETRN [6, 7, 8, 9, 10]. Consequently, special effort was made to develop highly efficient model parameterizations capable of fast execution times on computers. Transport codes are evaluated in the lab frame and do not require Lorentz-invariant[8] differential cross-sections. Instead, the non-invariant double-differential cross-section $\frac{d^2\sigma}{dEd\Omega}$ and non-invariant single-differential spectral $\frac{d\sigma}{dE}$ and angular $\frac{d\sigma}{d\Omega}$ cross-sections are required. Expressions for $\frac{d^2\sigma}{dEd\Omega}$ and $\frac{d\sigma}{dE}$ will be derived below, while $\frac{d\sigma}{d\Omega}$ will be left for future work.

5.1 Parameters

When using the equations in this section for transport codes, one needs to be careful to use the correct weighting factor parameters from Tables 4 and 5 as follows:

- If the *projectile* is a light ion (such as He), then use weightings from Table 4.
  - The weightings are the same for all light ion fragments. For example, $w_{\mathcal{D}} = 0.2$ for d, t, h, α.
- If the *projectile* is a heavy ion (such as C or Ar), then use weightings from Table 5.
  - The weightings are different for each light ion fragment. For example, $w_{\mathcal{D}} = 0.2$ for d; $w_{\mathcal{D}} = 0.2$ for t and h; $w_{\mathcal{D}} = 0.4$ for α.
  - The $w_{\mathcal{P}}$ weightings are different depending on whether the projectile nucleon number, $A_{\mathcal{P}}$, is smaller or greater than 20. For example, $w_{\mathcal{P}} = 2$ for d; $w_{\mathcal{D}} = 3$ for t and h; $w_{\mathcal{D}} = 3.5$ for α, when $A_{\mathcal{P}} \leq 20$. But $w_{\mathcal{P}} = 1$ for d; $w_{\mathcal{D}} = 2$ for t and h; $w_{\mathcal{D}} = 3$ for α, when $A_{\mathcal{P}} > 20$.

[8]The models were developed in terms of Lorentz-invariant cross-sections because Lorentz-invariance makes the mathematical transformations between different reference frames much simpler.

5.2 Non-invariant double-differential cross-section

The non-invariant double-differential cross-section $\frac{d^2\sigma}{dEd\Omega}$ is related to the Lorentz-invariant differential cross-section [30] for the outgoing fragment j via[9]

$$\frac{d^2\sigma}{dEd\Omega} = \frac{d^2\sigma}{dTd\Omega} = |\mathbf{p}|\frac{d^3\sigma}{dp^3/E} = \sqrt{T_{jL}(T_{jL}+2m_j)}\,\frac{d^3\sigma}{dp^3/E}\,, \tag{22}$$

with $dp^3 = p^2 dp d\Omega$, and $p \equiv |\mathbf{p}|$. Also, using $E_{jL} \equiv T_{jL} + m_j = \sqrt{p_{jL}^2 + m_j^2}$, the substitution $|\mathbf{p}| \equiv p_{jL} = \sqrt{T_{jL}(T_{jL}+2m_j)}$ has been made in order to write cross-sections as functions of the fragment kinetic energy T_{jL} used in transport codes.

5.2.1 Proton double-differential cross-section

Writing equation (14) in terms of kinetic energy and substituting into (22) gives the final form of the proton double-differential cross-section to be used in transport codes,

$$\begin{aligned}
\frac{d^2\sigma}{dT_{\mathrm{p}L}d\Omega_{\mathrm{p}L}} &= N_4\sqrt{T_{\mathrm{p}L}(T_{\mathrm{p}L}+2m_{\mathrm{p}})} \\
&\quad\times\Bigg\{\exp\left[[m_{\mathrm{p}} - \gamma_{\mathcal{P}L}(T_{\mathrm{p}L}+m_{\mathrm{p}}) + \gamma_{\mathcal{P}L}\,\beta_{\mathcal{P}L}\sqrt{T_{\mathrm{p}L}(T_{\mathrm{p}L}+2m_{\mathrm{p}})}\cos\theta_{\mathrm{p}L}]/\Theta_{\mathcal{P}}\right] \\
&\quad+\exp\left[[m_{\mathrm{p}} - \gamma_{\mathcal{C}L}(T_{\mathrm{p}L}+m_{\mathrm{p}}) + \gamma_{\mathcal{C}L}\,\beta_{\mathcal{C}L}\,\sqrt{T_{\mathrm{p}L}(T_{\mathrm{p}L}+2m_{\mathrm{p}})}\cos\theta_{\mathrm{p}L}]/\Theta_{\mathcal{C}}\right] \\
&\quad+\exp\left[[m_{\mathrm{p}} - \gamma_{\mathcal{T}L}\,(T_{\mathrm{p}L}+m_{\mathrm{p}}) + \gamma_{\mathcal{T}L}\,\beta_{\mathcal{T}L}\,\sqrt{T_{\mathrm{p}L}(T_{\mathrm{p}L}+2m_{\mathrm{p}})}\cos\theta_{\mathrm{p}L}]/\Theta_{\mathcal{T}}\right] \\
&\quad+w_{\mathcal{D}}^{(\mathrm{p})}\exp\left[[m_{\mathrm{p}} - \gamma_{\mathcal{P}L}\,(T_{\mathrm{p}L}+m_{\mathrm{p}}) + \gamma_{\mathcal{P}L}\,\beta_{\mathcal{P}L}\,\sqrt{T_{\mathrm{p}L}(T_{\mathrm{p}L}+2m_{\mathrm{p}})}\cos\theta_{\mathrm{p}L}]/\Theta_{\mathcal{D}}\right]\Bigg\},
\end{aligned} \tag{23}$$

with the relativistic γ and β factors given in equation (15).

[9] The solid angle is $d\Omega = \sin\theta d\theta d\phi = -d\cos\theta d\phi = -2\pi d\cos\theta$ when integrated over $d\phi$. Integrating gives $\int d\Omega = \int_0^{2\pi} d\phi \int_0^{\pi} sin\theta d\theta = -2\pi\int_1^{-1} d\cos\theta = 2\pi\int_{-1}^{1} d\cos\theta = 2\pi\int_{-1}^{1} dz = 4\pi$, with $z \equiv \cos\theta$.

5.2.2 Light ion double-differential cross-section

Writing equation (18) in terms of kinetic energy and substituting into (22) gives the final form of the light ion double-differential cross-section, in units of MeV/n, to be used in transport codes,

$$\begin{aligned}\frac{d^2\sigma}{dT_{AL}d\Omega_{AL}}\left[\frac{\text{mb}}{\text{MeV/n}}\right] &= A^2\,C_A N_4^A\sqrt{T_{AL}(T_{AL}+2m_\text{p})}\\ &\times\Big\{w_\mathcal{P}\exp\Big[[m_\text{p}-\gamma_{\mathcal{P}L}(T_{\text{p}L}+m_\text{p})+\gamma_{\mathcal{P}L}\,\beta_{\mathcal{P}L}\sqrt{T_{\text{p}L}(T_{\text{p}L}+2m_\text{p})}\cos\theta_{\text{p}L}]/\Theta_\mathcal{P}\Big]\\ &+ w_\mathcal{C}\exp\Big[[m_\text{p}-\gamma_{\mathcal{C}L}(T_{\text{p}L}+m_\text{p})+\gamma_{\mathcal{C}L}\,\beta_{\mathcal{C}L}\,\sqrt{T_{\text{p}L}(T_{\text{p}L}+2m_\text{p})}\cos\theta_{\text{p}L}]/\Theta_\mathcal{C}\Big]\\ &+ w_\mathcal{T}\exp\Big[[m_\text{p}-\gamma_{\mathcal{T}L}\,(T_{\text{p}L}+m_\text{p})+\gamma_{\mathcal{T}L}\,\beta_{\mathcal{T}L}\,\sqrt{T_{\text{p}L}(T_{\text{p}L}+2m_\text{p})}\cos\theta_{\text{p}L}]/\Theta_\mathcal{T}\Big]\\ &+ w_\mathcal{D}w_\mathcal{D}^{(\text{p})}\exp\Big[[m_\text{p}-\gamma_{\mathcal{P}L}\,(T_{\text{p}L}+m_\text{p})+\gamma_{\mathcal{P}L}\,\beta_{\mathcal{P}L}\,\sqrt{T_{\text{p}L}(T_{\text{p}L}+2m_\text{p})}\cos\theta_{\text{p}L}]/\Theta_\mathcal{D}\Big]\Big\}^A,\end{aligned} \tag{24}$$

where T_A is the kinetic energy of the light ion A, in units of MeV/n. The light ion mass, m_A, in the term,[10] $\sqrt{T_{AL}(T_{AL}+2m_A)}$, leads to the equality $\sqrt{T_{AL}(T_{AL}+2m_A)} = \sqrt{T_{AL}(T_{AL}+2m_\text{p})}$ when units of MeV/n are used. An overall multiplicative A^2 factor is introduced to ensure units of MeV/n, as discussed in Section 5.6.

5.3 Non-invariant single-differential spectral cross-section

A spectral distribution for production of particle j, is obtained by integrating $\frac{d^2\sigma}{dEd\Omega}$, as in

$$\begin{aligned}\frac{d\sigma}{dE} &= \frac{d\sigma}{dT} = \int d\Omega\frac{d^2\sigma}{dEd\Omega} = 2\pi\int_{-1}^{1} d\cos\theta\frac{d^2\sigma}{dEd\Omega} = 2\pi\int_{-1}^{1} dz\frac{d^2\sigma}{dEd\Omega}\\ &= 2\pi|\mathbf{p}|\int_{-1}^{1} d\cos\theta\frac{d^3\sigma}{dp^3/E} = 2\pi|\mathbf{p}|\int_{-1}^{1} dz\frac{d^3\sigma}{dp^3/E}\\ &= 2\pi\sqrt{T_{jL}(T_{jL}+2m_j)}\int_{-1}^{1} dz\frac{d^3\sigma}{dp^3/E}\,,\end{aligned} \tag{25}$$

with $z \equiv \cos\theta_{jL}$, and assuming azimuthal symmetry. Examination of equation (14) for the proton model and equation (18) for the light ion model shows that both models are written explicitly as functions of the proton angle, $z \equiv \cos\theta_{\text{p}L}$.

[10] Strictly speaking, the nucleon mass should be used instead of the proton mass, but the slight difference between the proton and nucleon mass leads to negligible differences in cross-section results.

5.4 Proton spectral distribution

In order to obtain the proton spectral distribution, the proton Lorentz-invariant double-differential cross-section of equation (14), must be inserted into the right hand side of (25). Isolating only the z terms to be integrated, equations (14) and (23) can be written in the general form

$$E_{\rm p}\frac{d^3\sigma_{\rm p}}{dp_{\rm p}^3} = N_4\left(V_{\mathcal{P}}e^{zW_{\mathcal{P}}} + V_{\mathcal{C}}e^{zW_{\mathcal{C}}} + V_{\mathcal{T}}e^{zW_{\mathcal{T}}} + V_{\mathcal{D}}e^{zW_{\mathcal{D}}}\right), \tag{26}$$

and

$$\frac{d^2\sigma_{\rm p}}{dT_{\rm p}d\Omega_{\rm p}} = N_4\sqrt{T_{{\rm p}L}(T_{{\rm p}L}+2m_{\rm p})}\left(V_{\mathcal{P}}e^{zW_{\mathcal{P}}} + V_{\mathcal{C}}e^{zW_{\mathcal{C}}} + V_{\mathcal{T}}e^{zW_{\mathcal{T}}} + V_{\mathcal{D}}e^{zW_{\mathcal{D}}}\right), \tag{27}$$

where V and W are constants with respect to $z \equiv \cos\theta_{{\rm p}L}$. In terms of kinetic energy,

$$V_{\mathcal{P}} \equiv \exp\{[m_{\rm p} - \gamma_{\mathcal{P}L}\,(T_{{\rm p}L}+m_{\rm p})]/\Theta_{\mathcal{P}}\} = e^{X_{\mathcal{P}}}, \tag{28}$$

$$W_{\mathcal{P}} \equiv [\gamma_{\mathcal{P}L}\,\beta_{\mathcal{P}L}\,\sqrt{T_{{\rm p}L}(T_{{\rm p}L}+2m_{\rm p})}\,]/\Theta_{\mathcal{P}}, \tag{29}$$

$$V_{\mathcal{C}} \equiv \exp\{[m_{\rm p} - \gamma_{\mathcal{C}L}\,(T_{{\rm p}L}+m_{\rm p})]/\Theta_{\mathcal{C}}\} = e^{X_{\mathcal{C}}}, \tag{30}$$

$$W_{\mathcal{C}} \equiv [\gamma_{\mathcal{C}L}\,\beta_{\mathcal{C}L}\,\sqrt{T_{{\rm p}L}(T_{{\rm p}L}+2m_{\rm p})}\,]/\Theta_{\mathcal{C}}, \tag{31}$$

$$V_{\mathcal{T}} \equiv \exp\{[m_{\rm p} - \gamma_{\mathcal{T}L}\,(T_{{\rm p}L}+m_{\rm p})]/\Theta_{\mathcal{T}}\} = \exp\{-T_{{\rm p}L}/\Theta_{\mathcal{T}}\} = e^{X_{\mathcal{T}}}, \tag{32}$$

$$W_{\mathcal{T}} \equiv [\gamma_{\mathcal{T}L}\,\beta_{\mathcal{T}L}\,\sqrt{T_{{\rm p}L}(T_{{\rm p}L}+2m_{\rm p})}\,]/\Theta_{\mathcal{T}} = 0, \tag{33}$$

$$V_{\mathcal{D}} \equiv w_{\mathcal{D}}^{({\rm p})}\exp\{[m_{\rm p} - \gamma_{\mathcal{P}L}\,(T_{{\rm p}L}+m_{\rm p})]/\Theta_{\mathcal{D}}\} = w_{\mathcal{D}}^{({\rm p})}e^{X_{\mathcal{D}}}, \tag{34}$$

$$W_{\mathcal{D}} \equiv [\gamma_{\mathcal{P}L}\,\beta_{\mathcal{P}L}\,\sqrt{T_{{\rm p}L}(T_{{\rm p}L}+2m_{\rm p})}\,]/\Theta_{\mathcal{D}}, \tag{35}$$

where the following definitions have been used,

$$X_{\mathcal{P}} \equiv [m_{\rm p} - \gamma_{\mathcal{P}L}\,(T_{{\rm p}L}+m_{\rm p})]/\Theta_{\mathcal{P}}, \tag{36}$$

$$X_{\mathcal{C}} \equiv [m_{\rm p} - \gamma_{\mathcal{C}L}\,(T_{{\rm p}L}+m_{\rm p})]/\Theta_{\mathcal{C}}, \tag{37}$$

$$X_{\mathcal{T}} \equiv [m_{\rm p} - \gamma_{\mathcal{T}L}\,(T_{{\rm p}L}+m_{\rm p})]/\Theta_{\mathcal{T}}\} = -T_{{\rm p}L}/\Theta_{\mathcal{T}}, \tag{38}$$

$$X_{\mathcal{D}} \equiv [m_{\rm p} - \gamma_{\mathcal{P}L}\,(T_{{\rm p}L}+m_{\rm p})]/\Theta_{\mathcal{D}}. \tag{39}$$

Also, $W_{\mathcal{T}} = 0$ because $\beta_{\mathcal{T}L} = 0$ (giving $\gamma_{\mathcal{T}L} = 1$), due to the lab frame being defined as the target frame. Using the result

$$\int_{-1}^{1} dz\exp[Wz] = \frac{2}{W}\sinh W, \tag{40}$$

and define

$$\mathcal{A}_i \equiv \frac{V_i}{W_i}\sinh W_i = \frac{w_i^{({\rm p})}}{2W_i}(e^{Z_i^+} - e^{Z_i^-}), \tag{41}$$

where

$$Z_i^{\pm} \equiv X_i \pm W_i \ , \tag{42}$$

and $w_i^{(\mathrm{p})} = 1$, for $i = \mathcal{P}, \mathcal{C}, \mathcal{T}$, and $w_i^{(\mathrm{p})} = w_{\mathcal{D}}^{(\mathrm{p})} = 30$, for $i = \mathcal{D}$. The $\frac{V_i}{W_i} \sinh W_i$ term in equation (41) contains multiplication of exponential functions, which can lead to overflow or underflow problems in compilers such as *FORTRAN*. It is better to multiply the exponential functions analytically, as given by the term $\frac{w_i^{(\mathrm{p})}}{2W_i}(e^{Z_i^+} - e^{Z_i^-})$, prior to numerical evaluation. This will eliminate overflow or underflow problems.

Note that $\lim_{x \to 0} \frac{\sinh x}{x} = 1$, yields

$$\mathcal{A}_{\mathcal{T}} = \frac{V_{\mathcal{T}}}{W_{\mathcal{T}}} \sinh W_{\mathcal{T}} = V_{\mathcal{T}}, \tag{43}$$

which needs to be implemented in equation (41) in order to avoid a numerical singularity due to $W_{\mathcal{T}} = 0$ mentioned previously.

The proton spectral distribution is obtained from equation (25) as

$$\frac{d\sigma}{dT_{\mathrm{p}L}} \ = \ 4\pi N_4 \sqrt{T_{\mathrm{p}L}(T_{\mathrm{p}L} + 2m_{\mathrm{p}})} \ (\mathcal{A}_{\mathcal{P}} + \mathcal{A}_{\mathcal{C}} + \mathcal{A}_{\mathcal{T}} + \mathcal{A}_{\mathcal{D}}) \tag{44}$$

written entirely in terms of kinetic energy, $T_{\mathrm{p}L}$, using equations (28) - (35). This is the final form of the spectral distribution for proton production. It is a very simple and compact, analytic equation involving no integrals, and is therefore a very efficient parameterization of the proton production spectral distribution. No numerical techniques are required for evaluation. Sample plots of the proton spectral distributions are provided in Figure 47. Sample results are in Table 7.

5.5 Light ion spectral distributions

The light ion spectral distribution is more difficult to obtain from equation (17) or (18), because of the fact that all of the contributing terms are summed and then raised to the power A. Therefore, a general analytic expression for the spectral distribution, analogous to equation (44) cannot be obtained. However, by definition, light ions only take the values $A = 2, 3, 4$ and so a separate analytic expression can be obtained for each value of A, as discussed below.

In the following equations, units will be denoted in square brackets, as in [units], on the left hand side of some equations. A full discussion of where these units come from is included in section 5.6.

In order to obtain the light ion spectral distribution, the Lorentz-invariant double-differential cross-section of equation (18), must be inserted into the right hand side of

(25). Again, isolating only the z terms to be integrated, equations (18) and (24) can be written

$$\frac{d^3\sigma}{dp^3/E}\left[\frac{\text{mb}}{(\text{MeV/n})^2}\right] = A^2\, C_A N_4^A \left(Y_{\mathcal{P}}\, e^{zW_{\mathcal{P}}} + Y_{\mathcal{C}}\, e^{zW_{\mathcal{C}}} + Y_{\mathcal{T}}\, e^{zW_{\mathcal{T}}} + Y_{\mathcal{D}}\, e^{zW_{\mathcal{D}}}\right)^A, \quad (45)$$

and

$$\begin{aligned}\frac{d^2\sigma}{dT_{jL}d\Omega_{jL}}\left[\frac{\text{mb}}{\text{MeV/n}}\right] &= A^2\, C_A N_4^A \sqrt{T_{jL}(T_{jL}+2m_j)} \\ &\quad \times \left(Y_{\mathcal{P}}\, e^{zW_{\mathcal{P}}} + Y_{\mathcal{C}}\, e^{zW_{\mathcal{C}}} + Y_{\mathcal{T}}\, e^{zW_{\mathcal{T}}} + Y_{\mathcal{D}}\, e^{zW_{\mathcal{D}}}\right)^A, \quad (46)\end{aligned}$$

with an overall multiplicative A factor being introduced to ensure units of MeV/n, and with m_j being given by the proton mass and T_{jL} written in units of MeV/n, as discussed in section 5.6. Also, Y and W are constants with respect to $z \equiv \cos\theta_{jL}$. Specifically,

$$\begin{aligned} Y_{\mathcal{P}} &\equiv w_{\mathcal{P}}\, V_{\mathcal{P}} = w_{\mathcal{P}}\, e^{X_{\mathcal{P}}}, & (47)\\ Y_{\mathcal{C}} &\equiv w_{\mathcal{C}}\, V_{\mathcal{C}} = w_{\mathcal{C}}\, e^{X_{\mathcal{C}}}, & (48)\\ Y_{\mathcal{T}} &\equiv w_{\mathcal{T}}\, V_{\mathcal{T}} = w_{\mathcal{T}}\, e^{X_{\mathcal{T}}}, & (49)\\ Y_{\mathcal{D}} &\equiv w_{\mathcal{D}}\, V_{\mathcal{D}} = w_{\mathcal{D}}^{(\text{p})}\, w_{\mathcal{D}}\, e^{X_{\mathcal{D}}}. & (50)\end{aligned}$$

Substituting equation (45) into (25) gives the general light ion spectral distribution for arbitrary A as

$$\begin{aligned}\frac{d\sigma}{dT}\left[\frac{\text{mb}}{\text{MeV/n}}\right] &= 2\pi A^2\, C_A N_4^A \sqrt{T_{jL}(T_{jL}+2m_{\text{p}})} \\ &\quad \times \int_{-1}^{1} dz \left(Y_{\mathcal{P}}\, e^{zW_{\mathcal{P}}} + Y_{\mathcal{C}}\, e^{zW_{\mathcal{C}}} + Y_{\mathcal{T}}\, e^{zW_{\mathcal{T}}} + Y_{\mathcal{D}}\, e^{zW_{\mathcal{D}}}\right)^A. \quad (51)\end{aligned}$$

Although this equation is easily evaluated numerically, it cannot be analytically integrated for arbitrary A. In the interests of providing results that can be efficiently used in transport codes, the above equation will now be analytically integrated for the values of A appropriate for light ions, namely $A = 2, 3, 4$.

5.5.1 Deuteron ($A = 2$) spectral distribution

Define

$$\bar{w}_i \equiv w_i \quad \text{for} \quad i = \mathcal{P}, \mathcal{C}, \mathcal{T}, \tag{52}$$

$$\bar{w}_i \equiv w_{\mathcal{D}}^{(\mathrm{p})} w_{\mathcal{D}} \quad \text{for} \quad i = \mathcal{D}, \tag{53}$$

and make the additional definitions

$$\mathcal{E}_i \equiv \frac{Y_i^2}{W_i} \sinh(2W_i) = \frac{\bar{w}_i^2}{2W_i} (e^{2Z_i^+} - e^{2Z_i^-}), \tag{54}$$

$$\mathcal{F}_{ij} \equiv \frac{4Y_iY_j}{W_i + W_j} \sinh(W_i + W_j) = \frac{2\bar{w}_i\bar{w}_j}{W_i + W_j} (e^{Z_i^+ + Z_j^+} - e^{Z_i^- + Z_j^-}), \tag{55}$$

where the exponential terms in the Y and sinh functions have been evaluated analytically, in order to avoid overflow or underflow problems, as discussed previously. Note that $\lim_{x\to 0} \frac{\sinh 2x}{x} = 2$, yields

$$\mathcal{E}_{\mathcal{T}} = \frac{Y_{\mathcal{T}}^2}{W_{\mathcal{T}}} \sinh(2W_{\mathcal{T}}) = 2Y_{\mathcal{T}}^2, \tag{56}$$

which needs to be implemented in equation (54) in order to avoid a numerical singularity. For $A = 2$, equation (51) is analytically integrated to give the deuteron spectral distribution in closed form as

$$\begin{aligned} \frac{d\sigma}{dT_{AL}} \left[\frac{\mathrm{mb}}{\mathrm{MeV/n}}\right] = {} & 2\pi A^2 C_A N_4^2 \sqrt{T_{AL}(T_{AL} + 2m_{\mathrm{p}})}\, (\mathcal{E}_{\mathcal{P}} + \mathcal{E}_{\mathcal{C}} + \mathcal{E}_{\mathcal{T}} + \mathcal{E}_{\mathcal{D}} \\ & + \mathcal{F}_{\mathcal{PC}} + \mathcal{F}_{\mathcal{PT}} + \mathcal{F}_{\mathcal{PD}} + \mathcal{F}_{\mathcal{CT}} + \mathcal{F}_{\mathcal{CD}} + \mathcal{F}_{\mathcal{TD}}), \end{aligned} \tag{57}$$

with m_{p} being given by the proton mass and T_{AL} in units of MeV/n. Sample plots of the deuteron spectral distributions are provided in Figure 47. Sample results are in Table 7.

5.5.2 Triton and Helion ($A = 3$) spectral distribution

Make the definitions

$$\mathcal{G}_i \equiv \frac{Y_i^3}{W_i}\sinh(3W_i) = \frac{\bar{w}_i^3}{2W_i}(e^{3Z_i^+} - e^{3Z_i^-}), \tag{58}$$

$$\mathcal{H}_{ij} \equiv \frac{9Y_i^2 Y_j}{2W_i + W_j}\sinh(2W_i + W_j) = \frac{9\bar{w}_i^2\bar{w}_j}{2(2W_i + W_j)}(e^{2Z_i^+ + Z_j^+} - e^{2Z_i^- + Z_j^-}), \tag{59}$$

$$\begin{aligned}\mathcal{J}_{ijk} &\equiv \frac{18Y_iY_jY_k}{W_i + W_j + W_k}\sinh(W_i + W_j + W_k) \\ &= \frac{9\bar{w}_i\bar{w}_j\bar{w}_k}{W_i + W_j + W_k}(e^{Z_i^+ + Z_j^+ + Z_k^+} - e^{Z_i^- + Z_j^- + Z_k^-}).\end{aligned} \tag{60}$$

Note that $\lim_{x\to 0}\frac{\sinh 3x}{x} = 3$, yields

$$\mathcal{G}_\mathcal{T} = \frac{Y_\mathcal{T}^3}{W_\mathcal{T}}\sinh(3W_\mathcal{T}) = 3Y_\mathcal{T}^3, \tag{61}$$

which needs to be implemented in equation (58) in order to avoid a numerical singularity. For $A = 3$, equation (51) is analytically integrated to give the triton and helion spectral distributions in closed form as

$$\begin{aligned}\frac{d\sigma}{dT_{AL}}\left[\frac{\text{mb}}{\text{MeV/n}}\right] &= 2\pi A^2\, C_A N_4^3\sqrt{T_{AL}(T_{AL} + 2m_\text{p})} \times \frac{2}{3}(\mathcal{G}_\mathcal{P} + \mathcal{G}_\mathcal{C} + \mathcal{G}_\mathcal{T} + \mathcal{G}_\mathcal{D} + \mathcal{H}_{\mathcal{PC}} \\ &+ \mathcal{H}_{\mathcal{PT}} + \mathcal{H}_{\mathcal{PD}} + \mathcal{H}_{\mathcal{CP}} + \mathcal{H}_{\mathcal{CT}} + \mathcal{H}_{\mathcal{CD}} + \mathcal{H}_{\mathcal{TP}} + \mathcal{H}_{\mathcal{TC}} + \mathcal{H}_{\mathcal{TD}} \\ &+ \mathcal{H}_{\mathcal{DP}} + \mathcal{H}_{\mathcal{DC}} + \mathcal{H}_{\mathcal{DT}} + \mathcal{J}_{\mathcal{CTD}} + \mathcal{J}_{\mathcal{PTD}} + \mathcal{J}_{\mathcal{PCD}} + \mathcal{J}_{\mathcal{PCT}}),\end{aligned} \tag{62}$$

with m_p being given by the proton mass and T_{AL} in units of MeV/n. Sample plots of the triton spectral distributions are provided in Figure 47. Sample results are in Table 7.

5.5.3 Alpha ($A = 4$) spectral distribution

Make the definitions

$$\mathcal{K}_i \equiv \frac{Y_i^4}{4W_i}\sinh(4W_i) = \frac{\bar{w}_i^4}{8W_i}(e^{4Z_i^+} - e^{4Z_i^-}), \tag{63}$$

$$\mathcal{L}_{ij} \equiv \frac{4Y_i^3 Y_j}{3W_i + W_j}\sinh(3W_i + W_j) = \frac{2\bar{w}_i^3\bar{w}_j}{3W_i + W_j}(e^{3Z_i^+ + Z_j^+} - e^{3Z_i^- + Z_j^-}), \tag{64}$$

$$\mathcal{M}_{ij} \equiv \frac{6Y_i^2 Y_j^2}{2(W_i + W_j)}\sinh 2(W_i + W_j) = \frac{3\bar{w}_i^2\bar{w}_j^2}{2(W_i + W_j)}(e^{2Z_i^+ + 2Z_j^+} - e^{2Z_i^- + 2Z_j^-}), \tag{65}$$

$$\begin{aligned}\mathcal{N}_{ijk} &\equiv \frac{12Y_i^2 Y_j Y_k}{2W_i + W_j + W_k}\sinh(2W_i + W_j + W_k) \\ &= \frac{6\bar{w}_i^2\bar{w}_j\bar{w}_k}{2W_i + W_j + W_k}(e^{2Z_i^+ + Z_j^+ + Z_k^+} - e^{2Z_i^- + Z_j^- + Z_k^-}),\end{aligned} \tag{66}$$

$$\begin{aligned}\mathcal{O}_{ijkl} &\equiv \frac{24Y_iY_jY_kY_l}{W_i + W_j + W_k + W_l}\sinh(W_i + W_j + W_k + W_l) \\ &= \frac{12\bar{w}_i\bar{w}_j\bar{w}_k\bar{w}_l}{W_i + W_j + W_k + W_l}(e^{Z_i^+ + Z_j^+ + Z_k^+ + Z_l^+} - e^{Z_i^- + Z_j^- + Z_k^- + Z_l^-}).\end{aligned} \tag{67}$$

Note that $\lim_{x\to 0}\frac{\sinh 4x}{4x} = 1$, yields

$$\mathcal{K}_\mathcal{T} = \frac{Y_\mathcal{T}^4}{4W_\mathcal{T}}\sinh(4W_\mathcal{T}) = Y_\mathcal{T}^4, \tag{68}$$

which needs to be implemented in equation (63) in order to avoid a numerical singularity. For $A = 4$, equation (51) is analytically integrated to give the alpha spectral distribution in closed form as

$$\begin{aligned}\frac{d\sigma}{dT_{AL}}\left[\frac{\text{mb}}{\text{MeV/n}}\right] &= 2\pi A^2\, C_A N_4^4\sqrt{T_{AL}(T_{AL} + 2m_\text{p})} \times 2(\mathcal{K}_\mathcal{P} + \mathcal{K}_\mathcal{C} + \mathcal{K}_\mathcal{T} + \mathcal{K}_\mathcal{D} \\ &+ \mathcal{L}_{\mathcal{PC}} + \mathcal{L}_{\mathcal{PT}} + \mathcal{L}_{\mathcal{PD}} + \mathcal{L}_{\mathcal{CP}} + \mathcal{L}_{\mathcal{CT}} + \mathcal{L}_{\mathcal{CD}} \\ &+ \mathcal{L}_{\mathcal{TP}} + \mathcal{L}_{\mathcal{TC}} + \mathcal{L}_{\mathcal{TD}} + \mathcal{L}_{\mathcal{DP}} + \mathcal{L}_{\mathcal{DC}} + \mathcal{L}_{\mathcal{DT}} \\ &+ \mathcal{M}_{\mathcal{PC}} + \mathcal{M}_{\mathcal{PT}} + \mathcal{M}_{\mathcal{PD}} + \mathcal{M}_{\mathcal{CT}} + \mathcal{M}_{\mathcal{CD}} + \mathcal{M}_{\mathcal{TD}} \\ &+ \mathcal{N}_{\mathcal{PCT}} + \mathcal{N}_{\mathcal{PCD}} + \mathcal{N}_{\mathcal{PTD}} + \mathcal{N}_{\mathcal{CPT}} + \mathcal{N}_{\mathcal{CPD}} + \mathcal{N}_{\mathcal{CTD}} \\ &+ \mathcal{N}_{\mathcal{TPC}} + \mathcal{N}_{\mathcal{TPD}} + \mathcal{N}_{\mathcal{TCD}} + \mathcal{N}_{\mathcal{DPC}} + \mathcal{N}_{\mathcal{DPT}} + \mathcal{N}_{\mathcal{DCT}} \\ &+ \mathcal{O}_{\mathcal{PCTD}}),\end{aligned} \tag{69}$$

with m_p being given by the proton mass and T_{AL} in units of MeV/n. Sample plots of the alpha spectral distributions are provided in Figure 47. Sample results are in Table 7.

5.6 Units

Unit analysis is very important when implementing the formulas of the present work into transport codes. Therefore, a detailed discussion is now given. The symbol $\sim$ will be used to denote units. Also, angles in steradian (sr) are not written explicitly, because they are not units in the normal sense. The system of units in the present work uses standard particle physics units, with the speed of light $c \equiv 1$. The units of the Lorentz-invariant double-differential cross-section are given by[11]

$$E\frac{d^3\sigma}{dp^3} \sim \frac{\text{mb}}{\text{MeV}^2}, \tag{70}$$

where $\sigma \sim$ mb and $E \sim p \sim$ MeV. Also, note $m \sim$ MeV. The coalescence model raises these units to the power of A on the right hand side of equation (1), implying that C_A carries *different* units for each light ion, depending on the value of A. Therefore, the units of C_A are

$$C_A \sim \left(\frac{\text{mb}}{\text{MeV}^2}\right)^{1-A}. \tag{71}$$

Equation (2) implies that the units of the normalization constant are the same as the Lorentz-invariant double-differential cross-section, namely

$$N \sim \frac{\text{mb}}{\text{MeV}^2}. \tag{72}$$

This is consistent with explicit formulas for N given in equations (4) and (16) where the units are carried by the term

$$\frac{\sigma}{m_{\text{p}}}\,\Theta^{-1} \sim \frac{\text{mb}}{\text{MeV}^2}, \tag{73}$$

with temperature units $\Theta \sim$ MeV.

Consider now the units of spectral distribution,

$$\frac{d\sigma}{dT} \sim \frac{\text{mb}}{\text{MeV}}, \tag{74}$$

and analyze the units in equation (51). Equations (28) - (35) show that the V and W terms do not carry units. This is denoted as

$$V \sim W \sim 1. \tag{75}$$

[11] Energy units of MeV are used for illustration. GeV can equally be used.

Therefore, the units of $\frac{d\sigma}{dT}$ in equation (51) are carried by the term $C_A N_4^A \sqrt{T_{jL}(T_{jL}+2m_j)}$, as in

$$\frac{d\sigma}{dT} \sim C_A N_4^A \sqrt{T_{jL}(T_{jL}+2m_j)} \sim \left(\frac{\text{mb}}{\text{MeV}^2}\right)^{1-\text{A}} \left(\frac{\text{mb}}{\text{MeV}^2}\right)^{\text{A}} \text{MeV} \sim \frac{\text{mb}}{\text{MeV}} \tag{76}$$

arriving at the correct units for $\frac{d\sigma}{dT}$.

Calculation of coalescence coefficients has been discussed previously [12], but important details will be repeated here. The coalescence coefficient, C_A, is calculated as [13]

$$C_A = \frac{\tilde{c}_A}{V^{A-1}} \,, \tag{77}$$

where $\tilde{c}_A$ is constant for each value of A. The interaction volume is $V = \frac{4}{3}\pi R^3$, with the interaction radius R given by [13]

$$R = a(A_{\mathcal{P}}^{1/3} + A_{\mathcal{T}}^{1/3}) + b \,, \tag{78}$$

where a and b are constants from reference [13] and listed in Table 6 of the present work. $A_{\mathcal{P}}$ and $A_{\mathcal{T}}$ are the mass numbers of the projectile and target nuclei, respectively. The units of R, a, b are all fm $\equiv 10^{-15}$m,

$$R \sim a \sim b \sim \text{fm}, \tag{79}$$

where

$$\text{fm}^2 \equiv 10\,\text{mb}. \tag{80}$$

The calculated C_A values in equation (77) require the constant $\tilde{c}_A$ values as input. These $\tilde{c}_A$ are constants, which vary only with A, and they have been determined [12] from the reaction Ar (800MeV/n) + KCl as follows,

$$\tilde{c}_A = C_A^{\text{obs[Ar(800MeV/n)+KCl]}} \, V^{A-1} \,, \tag{81}$$

where $C_A^{\text{obs[Ar(800MeV/n)+KCl]}}$ are the observed C_A values for the reaction of Ar (800MeV/n) + KCl [12, 13]. The units of $\tilde{c}_A$ are

$$\tilde{c}_A \sim \left(\frac{\text{mb}}{\text{MeV}^2}\right)^{1-A} (\text{fm}^3)^{A-1}, \tag{82}$$

Even though this can be simplified further using the relation between fm and mb in equation (80), it will be left in this form because the calculation of the interaction radius in equation (78), is naturally given in fm, and the units of the V^{A-1} term in the denominator of equation (77) cancels the $(\text{fm}^3)^{A-1}$ units in equation (82), to give $(\frac{\text{mb}}{\text{MeV}^2})^{1-A}$ in equation (77), as in

$$C_A = \frac{\tilde{c}_A}{V^{A-1}} \sim \frac{\left(\frac{\text{mb}}{\text{MeV}^2}\right)^{1-A} (\text{fm}^3)^{A-1}}{(\text{fm}^3)^{A-1}} \sim \left(\frac{\text{mb}}{\text{MeV}^2}\right)^{1-A}. \tag{83}$$

5.6.1 Units of MeV/n

Up to now, energy units of MeV have been discussed. However, HZETRN and many other transport codes instead use units of MeV/n. Refer to equation (1), where A is the mass of the emitted light ion. The energy units of $E_{\rm p}\frac{d^3\sigma_{\rm p}}{dp_{\rm p}^3}$ on the right hand side are MeV. With the definitions $p_A \equiv Ap_{\rm p}$ and $E_A \equiv AE_{\rm p}$, the energy units of $E_A\frac{d^3\sigma_A}{dp_A^3}$ on the left hand side are also obviously MeV and *not* MeV/n. Thus, the *natural units of the coalescence model* are MeV, *not* MeV/n, because of the definitions of p_A and E_A inherent in the coalescence model. Nevertheless, the conversion factor is simple, namely

$$E_A\frac{d^3\sigma_A}{dp_A^3}\ \left[\frac{\rm mb}{({\rm MeV/n})^2}\right] = A^2\,E_A\frac{d^3\sigma_A}{dp_A^3}\ \left[\frac{\rm mb}{\rm MeV^2}\right], \tag{84}$$

with the square brackets denoting units. In other words, in units of MeV/n, the coalescence model is written

$$E_A\frac{d^3\sigma_A}{dp_A^3}\ \left[\frac{\rm mb}{({\rm MeV/n})^2}\right] = A^2\,C_A\left(E_{\rm p}\frac{d^3\sigma_{\rm p}}{dp_{\rm p}^3}\right)^A, \tag{85}$$

instead of equation (1).

6 Summary, conclusions and future work

New models for proton and light ion production in nucleus-nucleus collisions have been introduced in the present work. The models are collectively referred to as DDFRG (Double-Differential FRaGmentation), which continues the set of nuclear physics models previously developed at NASA, known as NUCFRG [28], RAADFRG [29], EMDFRG [31] and QMSFRG [32]. The DDFRG models are the first set of models devoted to differential cross-sections, whereas the previous models [28, 29, 31] calculated total cross-sections only.

The goal has been to introduce parameterizations represented by analytic formulas that can be used efficiently in space radiation transport codes. The model for proton production represents three thermal sources produced in the projectile, central fireball, and target rest frames. An additional direct production Gaussian source (equivalent to a low temperature thermal source) has been introduced to account for quasi-elastic direct knockout. The model for light ion production uses a hybrid coalescence model in which particles from the four sources coalesce to form composite light ions. Weighting parameters have been introduced that give different weights to the four sources.

The models have been compared to a variety of high energy experimental data for both light and heavy ion projectiles, with the fragments being produced at both small and large angles. Agreement of the models with data is very good, with the models showing the large quasi-elastic peak at very small angles with suppression at large angles. The data shows variations with angle and fragment energy of many orders of magnitude and the models are able to capture this. In addition, the models have been developed to be valid for both light and heavy projectiles.

The main conclusion of the present work is that a single set of models, with judicious choice of a finite set of parameters, is able to describe a broad range of experimental data for proton and light ion production in relativistic heavy ion collisions relevant to space radiation.

The models were developed with emphasis on Lorentz-invariant double-differential cross-sections, as these were the data measured. However, space radiation transport codes generally use non-invariant double-differential cross-sections in energy and angle, and a set of closed-form analytic formulas for these quantities has been developed, as well as closed-form analytic formulas for fragment spectral distributions.

6.1 Future work

Further development of DDFRG is necessary for the following reasons:

1. Light ions and neutrons dominate dose-equivalent [1] for realistic shield thicknesses (≥ 20 g/cm^2). They are scattered at large angles and therefore require 3-dimensional transport (3DHZETRN) and nuclear physics double-differential cross-sections.

2. Transport code (GEANT, FLUKA, MCNP, PHITS, HZETRN, SHIELD) comparisons [3] show the largest differences for light ions. The disagreements are mainly due to inaccurate light ion nuclear physics models and lack of experimental data.

3. An experimental thick target program was recently completed at the NASA Space Radiation Laboratory (NSRL), located at Brookhaven National Laboratory, using unique combinations of double thick targets where incident beam particles scattered from the first target and secondary fragments subsequently scattered from a back target. This simulated the scattering geometry in a spacecraft, where fragments are produced when GCR interact with a spacecraft wall and more scattered products are produced from the far, back and surrounding walls. These measurements show significant discrepancies [33] compared to transport codes (MCNP, PHITS) for light ions. Further cross-section measurements of light ion fragments have been recommended to resolve these discrepancies.

4. Mars Science Laboratory Radiation Assessment Detector (MSL-RAD) light ion flux measurements highlight the need for improved nuclear interaction models. Light ion model results show moderate to large discrepancies [5, 34, 35] over the MSL-RAD energy range, with model errors mainly attributed to inaccurate light ion nuclear physics models. In this particular case, the observed discrepancies did not contribute significantly to dose-equivalent, but improvements would yield better agreement with MSL-RAD.

5. Calculations with the HZETRN transport code significantly under-predict dose measurements from the International Space Station [36, 37], at high latitudes where GCR contribute most. The cause of the discrepancy has yet to be fully clarified, but improvements to the underlying cross-section models may help remove some measure of uncertainty.

6. Recent measurements of light ion cross-section production at NSRL [38] show large differences between measurements and the light ion cross-section models used in the PHITS [39] transport code.

7. Light ion cross-section measurements [40] are needed to improve inaccurate light ion nuclear physics models. Reviewers of thick target experiments also recommended further cross-section measurements.

8. Light ion cross-sections represent the largest physics uncertainty in space radiation.

9. Light ion cross-section measurements represent the largest gap in the cross-section database [40].

10. An experimental double-differential cross-section measurement program was also recently completed at NSRL, using oxygen and iron beams on several targets, with

production of light ion fragments. Large differences were seen between measurements and the light ion cross-section models used in the PHITS [39] transport code.

The highest priority for future work is complete analysis of *all* experimental differential cross-section data that has been measured and is relevant for space radiation. The parameters in the present work need to be fine-tuned to fit all available data. One of the most time-consuming parts of the present work was correct treatment of the transverse momentum variables in which the data were measured. Generally, it is not a simple task to acquire the data and compare the theoretical models, especially for differential cross-sections, and often a great deal of work is required. Neutron double-differential cross-sections can be just as important as light ion cross-sections. DDFRG can be adapted to provide models for neutron production. A list of prioritized future work is given below:

1. Complete analysis of all existing experimental differential cross-section data relevant to space radiation.

2. Tune model parameters to obtain best fits to all data.

3. Develop analytic formulas for angular distributions, $\frac{d\sigma}{d\Omega}$.

4. Improve RAADFRG predictions of light ion and neutron total cross-sections.

5. Make predictions for light ion total cross-sections, by integrating the Lorentz-invariant double-differential cross-sections developed in the present work. Compare predictions to the NUCFRG [28] and RAADFRG [29] codes.

6. Adapt the proton production model to account for neutron production.

7. Develop a high energy proton and light ion production model. The thermal models discussed in the present work are expected to be accurate in the intermediate energy region, but not at high energy. A high energy model, perhaps based on Feynman scaling, needs to be developed. Existing models [41, 42, 43] can be adapted.

8. Double-differential and single-differential electromagnetic dissociation contributions [31, 44] need to be added to the models developed herein. Existing models [44] can be adapted.

9. Compare cross-section model predictions to other models, such as those used in the Russian (ROSCOSMOS) SHIELD transport code [3, 4] and other transport codes.

10. Make further recommendations for future cross-section measurements.

11. Compare the updated 3DHZETRN code with measurements, such as those obtained with MSLRAD [5, 34, 35].

7 Appendix: Transforming transverse momentum to angle

Inclusive nuclear or particle reactions can be written in general form as

$$P + T \rightarrow F + \cdots, \tag{86}$$

where P represents the projectile, T represents the target and F represents the fragment of interest. The reaction is denoted as inclusive because final state reactions products, other than F, are not specified. If all final state particles are listed, then the reaction is called exclusive. An inclusive reaction is the sum of all exclusive reactions that include F in the final state. The 3-dimensional volume element in momentum space is

$$dp^3 = p^2 dp d\Omega = p^2 dp \sin\theta d\theta d\phi, \tag{87}$$

where $p \equiv |\mathbf{p}|$ is the magnitude of the 3-momentum. Assuming azimuthal symmetry, the momentum volume element becomes [30, 41, 44, 45, 46]

$$dp^3 = p^2 dp d\Omega = 2\pi p^2 dp \sin\theta d\theta \quad \text{(spherical coordinates)}, \tag{88}$$

$$= 2\pi p^{||} p^{\perp} dp^{\perp} \quad \text{(cylindrical coordinates)}, \tag{89}$$

with the longitudinal momentum, $p^{||}$, and transverse momentum, $p^{\perp}$, defined as

$$p^{||} \equiv p\cos\theta, \tag{90}$$

$$p^{\perp} \equiv p\sin\theta. \tag{91}$$

The momentum and angle variables are used to construct double-differential cross-sections for production of fragment, F.

In spherical coordinates with azimuthal symmetry, the two fundamental fragment independent variables are momentum and angle, (p, θ). In cylindrical coordinates with azimuthal symmetry, the fundamental independent fragment variables are longitudinal and transverse momentum, $(p^{||}, p^{\perp})$. The double-differential cross-sections will always be written in terms of the fragment independent variables, and experimental and theoretical plots of cross-sections can be made in three dimensions, with the vertical y axis representing the double-differential cross-section and the two horizontal x and z axes representing the two independent variables. Usually, however, plots will be made in two dimensions with the vertical y axis representing the double-differential cross-section, the horizontal x axis representing momentum, p, and a family of curves plotted for various angles, θ. Equivalently, the x axis can be $p^{||}$, and a family of curves plotted for various values of $p^{\perp}$.

A thermal/coalescence model for light ion fragment double-differential cross-sections was presented in reference [12] and compared to a variety of experimental data [13]. The data was given in terms of momentum and angle, (p, θ), and all model and experimental

cross-section plots were made in terms of these variables. Also, the theoretical models were mainly presented in terms of momentum and angle, (p, θ), but it was also shown how to write the theoretical models in terms of longitudinal and transverse momentum, $(p^{||}, p^{\perp})$.

Another important and extensive data set has been presented by Anderson and collaborators [16]. However, this data set was not analyzed in the previous work [12] and the aim of the present paper is to compare the thermal/coalescence model developed in reference [12] to the Anderson data set [16]. It will be seen that comparing theoretical models to differential cross-section data is never straightforward, unlike the situation for total cross-section data. Differential cross-section data is almost always reported in terms of variables quite different to variables employed in a given theoretical model. The conversion of the variable sets from experiment to theoretical models and vice versa is often extremely cumbersome and very time consuming, as will be seen in the present work, and as also illustrated in previous works [41, 42, 47, 48].

The Anderson data set [16] contains a complicated set of fragment variables. The two independent variables are neither momentum and angle, (p, θ), nor longitudinal and transverse momentum, $(p^{||}, p^{\perp})$, but rather involve a hybrid mixture of the dependent variables, momentum and transverse momentum, $(p, p^{\perp})$; a mixture of one spherical coordinate variable, p, and one cylindrical coordinate variable, $p^{\perp}$. It will now be shown how to use these dependent hybrid variables.

7.1 Thermal proton production model

Equation (91) implies that

$$\theta = \arcsin(p^{\perp}/p), \tag{92}$$

so that the spherical coordinate set, (p, θ), is replaced by $(p, \arcsin(p^{\perp}/p))$, which is a function of the mixed variable set $(p, p^{\perp})$.

7.1.1 (p_{jL}, θ_{jL}) variables

The thermal model for a particle j emitted in the $*$ frame ($*$ = projectile or central fireball or target) is [12]

$$E\frac{d^3\sigma_*}{dp^3}(p_{jL}, \theta_{jL}) = N\, e^{-T_{j*}/\Theta_*} = N\, \exp[-T_{j*}(p_{jL}, \theta_{jL})/\Theta_*], \tag{93}$$

where p_{jL} and θ_{jL} are the momentum and angle of particle j in the lab frame, L. The notation (p_{jL}, θ_{jL}) indicates that the functions must be written as explicit functions of the lab frame L variables p_{jL} and θ_{jL} because these are the variables used for the experimental cross-sections, with which the thermal model is to be compared. However, T_{j*} is the

kinetic energy of particle j in the $*$ frame, and this needs to be Lorentz-transformed to the lab frame, L. The temperature of the $*$ frame is Θ_*, which does not need to be Lorentz-transformed because it is a Lorentz-scalar.

In order to Lorentz-transform the particle j kinetic energy, use equation (6) to write

$$T_{j*} = E_{j*} - m_{j*}. \tag{94}$$

The Lorentz-transformation of the total energy is [30]

$$E_{j*} = \gamma_{*L}\, E_{jL} - \gamma_{*L}\, \beta_{*L}\, p_{ZjL}\ , \tag{95}$$

where the longitudinal momentum is given as

$$p_{ZjL} \equiv p_{jL} \cos\theta_{jL}, \tag{96}$$

with $p_{jL} \equiv |\mathbf{p}_{jL}|$. The relativistic γ_{*L} and β_{*L} factors refer to the speed of the $*$ frame with respect to the lab frame, L. That is, they are relations *between* different reference frames and have nothing to do with particle j. Thus, the Lorentz-transformed total energy of particle j in terms of (p_{jL}, θ_{jL}) variables is [12]

$$E_{j*} = \gamma_{*L} \sqrt{p_{jL}^2 + m_j^2} - \gamma_{*L}\, \beta_{*L}\, p_{jL} \cos\theta_{jL}\ , \tag{97}$$

which is simply substituted into equation (93) via equation (94) to give the final answer for the thermal model Lorentz-invariant double-differential cross-section in the $*$ frame,

$$E\frac{d^3\sigma_*}{dp^3}(p_{jL}, \theta_{jL}) = N\ \exp[-(\gamma_{*L} \sqrt{p_{jL}^2 + m_j^2} - \gamma_{*L}\, \beta_{*L}\, p_{jL} \cos\theta_{jL} - m)/\Theta_*]. \tag{98}$$

7.1.2 $(p_{jL}, p_{jL}^{\perp})$ variables

From equation (91), transverse momentum of particle j is

$$p_{jL}^{\perp} \equiv p_{jL} \sin\theta_{jL}, \tag{99}$$

giving the lab scattering angle of particle j as

$$\theta_{jL} = \arcsin(p_{jL}^{\perp}/p_{jL}), \tag{100}$$

which is a specific form of equation (92). However, θ_{jL} is a double valued function: The same value of $p^{\perp}$ can give rise to two different values of θ_{jL} in the interval[12] $0 < \theta_{jL} < \pi$. The two values of θ_{jL} are

$$\theta_{jL}^{(1)} = \arcsin(p_{jL}^{\perp}/p_{jL}), \tag{101}$$

$$\theta_{jL}^{(2)} = \pi - \arcsin(p_{jL}^{\perp}/p_{jL}), \tag{102}$$

[12] If the interval is not restricted, then θ_{jL} is a multivalued function.

Substituting $\theta_{jL}^{(2)}$ into (99), with the trigonometric [18] identity, $\sin(\pi-\theta)=\sin\theta$, gives[13]

$$p_{jL}^{\perp(2)} = p_{jL}\sin\theta_{jL}^{(2)} = p_{jL}\sin[\pi-\arcsin(p_{jL}^{\perp}/p_{jL})] \tag{103}$$

$$= p_{jL}\sin[\arcsin(p_{jL}^{\perp}/p_{jL})] = p_{jL}\sin\theta_{jL}^{(1)} \equiv p_{jL}^{\perp(1)}, \tag{104}$$

showing that the two different angles, $\theta_{jL}^{(1)}$ and $\theta_{jL}^{(2)}$, give the same value of $p_{jL}^{\perp}$, as required.

The double valued function gives rise to double values of longitudinal momentum,

$$p_{ZjL}^{(1)} = p_{jL}\cos\theta_{jL}^{(1)}, \tag{105}$$

$$p_{ZjL}^{(2)} = p_{jL}\cos\theta_{jL}^{(2)} \tag{106}$$

$$= p_{jL}\cos[\pi-\arcsin(p_{jL}^{\perp}/p_{jL})] = -p_{jL}\cos[\arcsin(p_{jL}^{\perp}/p_{jL})] \tag{107}$$

$$= -p_{jL}\cos\theta_{jL}^{(1)} = -p_{ZjL}^{(1)}, \tag{108}$$

using $\cos(\pi-\theta)=-\cos\theta$. The above result, that the longitudinal momenta are the same in magnitude, but opposite in direction, is expected, and can be written in compact form,

$$p_{ZjL}^{(1,2)} = p_{ZjL}^{\pm} = \pm|p_{ZjL}|\ , \tag{109}$$

where $|p_{ZjL}| \equiv |p_{ZjL}^{(1)}| = |p_{ZjL}^{(2)}|$. Equation (109) shows $p_{ZjL}^{(1)}$ taking the positive sign in the forward Z direction and $p_{ZjL}^{(2)}$ taking the negative sign in the backward Z direction. The double values of energy are

$$E_{j*}^{(1)} = \gamma_{*L}\sqrt{p_{jL}^2+m_j^2} - \gamma_{*L}\,\beta_{*L}\,p_{ZjL}^{(1)}, \tag{110}$$

$$E_{j*}^{(2)} = \gamma_{*L}\sqrt{p_{jL}^2+m_j^2} - \gamma_{*L}\,\beta_{*L}\,p_{ZjL}^{(2)}$$

$$= \gamma_{*L}\sqrt{p_{jL}^2+m_j^2} + \gamma_{*L}\,\beta_{*L}\,p_{ZjL}^{(1)}, \tag{111}$$

or, in compact form,

$$E_{j*}^{(2,1)} \equiv E_{j*}^{\pm} = \gamma_{*L}\sqrt{p_{jL}^2+m_j^2} \pm \gamma_{*L}\,\beta_{*L}\,|p_{ZjL}|. \tag{112}$$

The kinetic energy values are

$$T_{j*}^{(1)} = E_{j*}^{(1)} - m_{j*}\ , \tag{113}$$

$$T_{j*}^{(2)} = E_{j*}^{(2)} - m_{j*}\ , \tag{114}$$

or

$$T_{j*}^{(2,1)} = T_{j*}^{\pm} = E_{j*}^{\pm} - m_{j*}. \tag{115}$$

[13]The alternate possible solution, $\theta_{jL}^{(2)} = \pi/2 + \arcsin(p_{jL}^{\perp}/p_{jL})$, is not used because it does not lead to the required result, $p_{jL}^{\perp(1)} = p_{jL}^{\perp(2)}$.

Note that

$$(p_{jL}^{(1)})^2 = (p_{ZjL}^{(1)})^2 + (p_{jL}^{\perp(1)})^2 = (p_{ZjL}^{(2)})^2 + (p_{jL}^{\perp(2)})^2 = (p_{jL}^{(2)})^2, \tag{116}$$

so that no (1,2) index is required for p_{jL}^2, since $p_{jL}^2 = (p_{jL}^{\pm})^2 = (p_{jL}^{(1)})^2 = (p_{jL}^{(2)})^2$.

The behavior of the energy is very important. Equations (110) and (111) show that the expressions for energy are the same except for a change in sign of the second term. This is also see in equation (97), which also shows that the second term undergoes a change in sign as θ crosses over the value of $\pi/2$. The cross-section in equation (98) changes smoothly as θ varies across $\pi/2$. The map from angle to cross-section is one-to-one, which is typical of a well behaved function.

As a consequence of equations (101) - (114), the cross-section in $(p_{jL}, p_{jL}^{\perp})$ variables is double valued,

$$E\frac{d^3\sigma_*^{(1)}}{dp^3}(p_{jL}, p_{jL}^{\perp}) = N\, e^{-T_{j*}^{(1)}/\Theta_*}$$

$$= N \exp\{[\gamma_{*L}\sqrt{p_{jL}^2 + m_j^2} - \gamma_{*L}\,\beta_{*L}\,p_{jL}\cos[\arcsin(p_{jL}^{\perp}/p_{jL})] - m_{j*}]/\Theta_*\}\,, \tag{117}$$

and

$$E\frac{d^3\sigma_*^{(2)}}{dp^3}(p_{jL}, p_{jL}^{\perp}) \;=\; N\, e^{-T_{j*}^{(2)}/\Theta_*}$$

$$= N \exp\{[\gamma_{*L}\sqrt{p_{jL}^2 + m_j^2} - \gamma_{*L}\,\beta_{*L}\,p_{jL}\cos[\pi - \arcsin(p_{jL}^{\perp}/p_{jL})] - m_{j*}]/\Theta_*\}$$

$$= N \exp\{[\gamma_{*L}\sqrt{p_{jL}^2 + m_j^2} + \gamma_{*L}\,\beta_{*L}\,p_{jL}\cos[\arcsin(p_{jL}^{\perp}/p_{jL})] - m_{j*}]/\Theta_*\}\,, \tag{118}$$

representing a one-to-many (two) map from $p^{\perp}$ to cross-section, which is not a well behaved function. In compact form,

$$E\frac{d^3\sigma_*^{(2,1)}}{dp^3}(p_{jL}, p_{jL}^{\perp}) \equiv E\frac{d^3\sigma_*^{\pm}}{dp^3}(p_{jL}, p_{jL}^{\perp})\,, \tag{119}$$

with

$$E\frac{d^3\sigma_*^{\pm}}{dp^3}(p_{jL}, p_{jL}^{\perp})$$

$$= N \exp\{[\gamma_{*L}\sqrt{p_{jL}^2 + m_j^2} \pm \gamma_{*L}\,\beta_{*L}\,p_{jL}\cos[\arcsin(p_{jL}^{\perp}/p_{jL})] - m_{j*}]/\Theta_*\}. \tag{120}$$

In spite of the fact that the differential cross-section function (120) is double valued over the interval $\theta : 0 \leq \theta \leq \pi$, it is actually a well behaved single valued function over

the separate intervals $\theta : 0 \leq \theta \leq \pi/2$ and $\theta : \pi/2 < \theta \leq \pi$. Mathematically, this is written

$$E\frac{d^3\sigma_*}{dp^3}(p_{jL},\theta_{jL}) \quad = \quad \begin{cases} E\frac{d^3\sigma_*^-}{dp^3}(p_{jL},p_{jL}^\perp)\ , & 0 \leq \theta_{jL} \leq \pi/2, \\ \\ E\frac{d^3\sigma_*^+}{dp^3}(p_{jL},p_{jL}^\perp)\ , & \pi/2 < \theta_{jL} \leq \pi. \end{cases} \tag{121}$$

However, over the $p^\perp$ interval, the function cannot be written in such a concise form and it remains double valued over any $p^\perp$ interval. Therefore, the double valued differential cross-section (120) is impractical to deal with, especially when comparing cross-section model calculations to experiment. A well behaved single valued function is required. Experimentally, there will only be one measured differential cross-section value associated to each $p_{jL}^\perp$ value: Nature is single valued. The fundamental question is how to deal practically with the double valued differential cross-section (120), when performing cross-section model calculations and comparing to experiment. The only practical solution is to incoherently[14] add the two values as in

$$E\frac{d^3\sigma_*}{dp^3}(p_{jL},p_{jL}^\perp) = E\frac{d^3\sigma_*^+}{dp^3}(p_{jL},p_{jL}^\perp) + E\frac{d^3\sigma_*^-}{dp^3}(p_{jL},p_{jL}^\perp), \tag{122}$$

which now represents a well behaved single valued function! This makes perfect sense: A single value of $p_{jL}^\perp$ will receive a contribution from both $\theta_{jl}^{(1)}$ and $\theta_{jl}^{(2)}$. Equation (122) is the final theoretical result to be compared to experiment.

7.1.3 Integrating the differential cross-section to form the total cross-section

The thermal model is expressed very simply in the rest frame of the nucleus in which the fragments are being emitted, but is expressed in a complicated way after Lorentz transformation to the lab frame. Compare equations (93) and (120).

An important check of the Lorentz transformation of differential cross-sections can always be made. The total cross-section is obtained by integrating the differential cross-sections. Because the total cross-section is a Lorentz scalar (meaning that it is Lorentz invariant), it will have the same value in different reference frames. Therefore, integration of the simple expression (93), should give the same value as the integral of the complicated Lorentz transformed expression (120). Also, the integration variables will be different and will be local to the appropriate reference frame. Such as test is always carried out in the present and previous [12] work, and gives one complete confidence that the complicated Lorentz transformations are being done correctly.

[14] In quantum mechanics, there are two types of addition. Coherent addition refers to the addition of complex valued scattering amplitudes, whereas incoherent addition refers to the addition of real valued cross-sections.

In the present work, the integration becomes much more complicated than previously [12] because the differential cross-section is now double valued with the $(p, p^\perp)$ variable set. Making the integrations even more complicated is the fact that the variables $(p, p^\perp)$ are not completely independent, because $p^\perp$ depends on p via equation (91).

This dependence will now seen to be important when the momentum volume element is integrated to form a total cross-section, σ, as in

$$\sigma \equiv \int \frac{dp^3}{E} \frac{d^3\sigma}{dp^3/E}, \tag{123}$$

where the Lorentz-invariant differential cross-section is used as an integration example. There are two pieces in any integral: One is the volume element, dp^3, and the other is the integrand, $\frac{d^3\sigma}{dp^3/E}$. Each of these will now be considered separately.

Equation (91) gives

$$d\theta = \frac{dp^\perp}{p\cos\theta}. \tag{124}$$

Substituting into the volume element in equation (88) gives

$$\begin{aligned} dp^3 = 2\pi p^2 dp \sin\theta d\theta &= 2\pi p\, dp \tan\theta\, dp^\perp & (125)\\ &= 2\pi p\, dp \tan[\arcsin(p^\perp/p)]\, dp^\perp, & (126) \end{aligned}$$

which is the momentum volume element written in terms of spherical/cylindrical hybrid variables, $(p, p^\perp)$. Integration of the volume element with spherical coordinates is

$$\begin{aligned} \int dp^3 &= 2\pi \int_0^\infty dp \int_0^\pi d\theta\ \ p^2 \sin\theta, & (127)\\ &= 2\pi \int_0^\infty dp \int_0^{\pi/2} d\theta\ \ p^2 \sin\theta\ +\ 2\pi \int_0^\infty dp \int_{\pi/2}^\pi d\theta\ \ p^2 \sin\theta, & (128) \end{aligned}$$

where the latter equation shows an equivalent way of writing the integral, but separated into two angular regions. Integration with hybrid variables is somewhat subtle. Equation (91) shows that the value of $p^\perp$ ranges from 0 to a maximum value of p, so that the integration limits for $p^\perp$ appear as

$$\begin{aligned} \int dp^3 = 2\pi \int p^2 dp \sin\theta d\theta &= 2\pi \int p\, dp \tan\theta\, dp^\perp & (129)\\ &\neq 2\pi \int_0^\infty dp \int_0^p dp^\perp\ \ p \tan[\arcsin(p^\perp/p)]. & (130) \end{aligned}$$

The symbol $\neq$ is used instead of an $=$ sign, because it is shown below that this equation is actually incorrect. Note the complication of the hybrid variables: The two integrals, $\int dp^\perp$ and $\int dp$, are not independent. The upper limit of the $\int dp^\perp$ integral depends on

the value of p in the $\int dp$ integral. A further complication is that the full range of θ is not covered in the above expression. With $p^\perp$ ranging from 0 to p, the value of θ only ranges from 0 to $\pi/2$. Mathematically,

$$\theta : 0 \to \pi/2 \;\Rightarrow\; p^\perp : 0 \to p, \tag{131}$$

as seen in equation (91). Thus, to capture the full range $\theta : 0 \to \pi$, one must cover the interval $p^\perp : 0 \to p$ for a second time in equation (130). Of course it is wrong to simply multiply the integral by 2, because the values of $p^\perp$ are completely different in the two angular regions on either side of $\pi/2$. Adding $\pi/2$, as in

$$\begin{aligned} \int dp^3 \quad \neq \quad & 2\pi \int_0^\infty dp \int_0^p dp^\perp \;\; p \tan[\arcsin(p^\perp/p)] \\ + \quad & 2\pi \int_0^\infty dp \int_0^p dp^\perp \;\; p \tan[\pi/2 + \arcsin(p^\perp/p)], \end{aligned} \tag{132}$$

covers the full angular range, $\theta : 0 \to \pi/2 \to \pi = 0 \to \pi$. However, $p^\perp$ is not covering the range correctly. As the angle changes, $\theta : 0 \to \pi/2 \to \pi$, the transverse momentum should change as $p^\perp : 0 \to p \to 0 = 0 \to 0$. Thus, the second $p^\perp$ integral should have the limits interchanged, as in $\int_p^0 dp^\perp$. But, to get the same angular variation, $\theta : 0 \to \pi/2 \to \pi = 0 \to \pi$, one must now use $\tan[\pi - \arcsin(p^\perp/p)]$. Therefore, the correct simultaneous variation of both θ and $p^\perp$ occurs by writing the integral as

$$\begin{aligned} \int dp^3 \quad = \quad & 2\pi \int_0^\infty dp \int_0^p dp^\perp \;\; p \tan[\arcsin(p^\perp/p)] \\ + \quad & 2\pi \int_0^\infty dp \int_p^0 dp^\perp \;\; p \tan[\pi - \arcsin(p^\perp/p)]. \end{aligned} \tag{133}$$

Equation (133) can be checked for correctness. One can take an expression [12] for the Lorentz-invariant double-differential cross-section and integrate over the (p, θ) variable set to obtain the total cross-section, as in equation (123). Using equation (127), this is very straightforward and non-problematic. One can then perform integration with the hybrid variables, as given by equation (133). If the above mathematics is correct, then the value of the total cross-section, σ, obtained with either integration method should be the same. This was confirmed for a variety of test cases.

It is now a straightforward procedure to insert the double valued differential cross-section integrand (120), into the total cross-section integral (123), using the measure (133). The result is

$$\sigma \quad = \quad \int \frac{dp^3}{E} E \frac{d^3\sigma_*^\pm}{dp^3}(p_{jL}, p_{jL}^\perp) \tag{134}$$

$$\begin{aligned} = \quad & 2\pi \int_0^\infty dp \int_0^p dp^\perp \;\; \frac{p}{E} \tan[\arcsin(p^\perp/p)] E \frac{d^3\sigma_*^-}{dp^3}(p_{jL}, p_{jL}^\perp) \\ + \quad & 2\pi \int_0^\infty dp \int_p^0 dp^\perp \;\; \frac{p}{E} \tan[\pi - \arcsin(p^\perp/p)] E \frac{d^3\sigma_*^+}{dp^3}(p_{jL}, p_{jL}^\perp). \end{aligned} \tag{135}$$

Using the identity [18], $\tan(\pi-\theta) = -\tan\theta$, and $\int_p^0 dp^\perp = -\int_0^p dp^\perp$, gives

$$\sigma = 2\pi \int_0^\infty dp \int_0^p dp^\perp \; \frac{p}{E} \tan[\arcsin(p^\perp/p)] \left\{ E\frac{d^3\sigma_*^+}{dp^3}(p_{jL}, p_{jL}^\perp) + E\frac{d^3\sigma_*^-}{dp^3}(p_{jL}, p_{jL}^\perp) \right\}, \quad (136)$$

or simply,

$$\sigma = 2\pi \int_0^\infty dp \int_0^p dp^\perp \; \frac{p}{E} \tan[\arcsin(p^\perp/p)] E\frac{d^3\sigma_*}{dp^3}(p_{jL}, p_{jL}^\perp), \quad (137)$$

with $E\frac{d^3\sigma_*}{dp^3}(p_{jL}, p_{jL}^\perp)$ from equation (122). Equation (137) makes perfect sense: If the differential cross-section in equation (122) has truly become a well behaved single value function, as claimed, then it's integral should be a simple, straightforward expression that one would obtain without even thinking about issues of double values, either in the integrand or volume element; and that is precisely what equation (137) represents!

Participant (Central Fireball) Temperature	$\Theta_{\mathcal{C}}$	110 MeV
Spectator (Projectile = Target) Temperature	$\Theta_{\mathcal{P}} = \Theta_{\mathcal{T}}$	35 MeV
Direct Knockout Effective Temperature	$\Theta_{\mathcal{D}}$	2.8 MeV
Direct Knockout Normalization	$w_{\mathcal{D}}^{(\mathrm{p})}$	30

Table 1: Proton thermal model temperatures and direct normalization parameters. The temperatures, $\Theta_{\mathcal{C}}$ and $\Theta_{\mathcal{P}} = \Theta_{\mathcal{T}}$, are the same as previous work [12].

Reaction	σ (b)
Ar (800 MeV/n) + KCl $\rightarrow$ p + X	16
C (800 MeV/n) + C $\rightarrow$ p + X	3.5
C (1.05 GeV/n) + C $\rightarrow$ p + X	3.6
α (1.05 GeV/n) + C $\rightarrow$ p + X	0.65

Table 2: Total strong interaction cross-sections calculated from NUCFRG3 [28].

Units	$\tilde{c}_A$(d)	$\tilde{c}_A$(t,h)	$\tilde{c}_A(\alpha)$
$\left(\frac{\mathrm{mb}}{\mathrm{GeV}^2}\right)^{1-A} (\mathrm{fm}^3)^{A-1}$	1.6×10^{-3}	6.9×10^{-7}	1.3×10^{-10}
$\left(\frac{\mathrm{mb}}{\mathrm{MeV}^2}\right)^{1-A} (\mathrm{fm}^3)^{A-1}$	1.6×10^{3}	6.9×10^{5}	1.3×10^{8}

Table 3: Constants $\tilde{c}_A$ used for calculation of the coalescence coefficient, C_A, given in equation (77). The first row is the same as Table 7 of previous work [12].

$w_{\mathcal{P}}$	1
$w_{\mathcal{C}}$	3.5
$w_{\mathcal{T}}$	1
$w_{\mathcal{D}}$	2

Table 4: Light ion projectile weighting factors are the same for all fragments d, t, h, α.

	d	t,h	α
$w_{\mathcal{P}}$ ($\mathrm{A}_P \leq 20$)	2	3	3.5
$w_{\mathcal{P}}$ ($\mathrm{A}_P > 20$)	1	2	3
$w_{\mathcal{C}}$	1	1	1
$w_{\mathcal{T}}$	1	1	1
$w_{\mathcal{D}}$	0.2	0.2	0.4

Table 5: Heavy ion projectile weighting factors for fragments d, t, h, α. The value of $w_{\mathcal{P}}$ depends on A_P, which denotes the mass number of the projectile.

	d	t,h	α
a (fm)	0.24	0.24	0.24
b (fm)	2.0	1.6	1.0

Table 6: Constants [13] used for calculation of the interaction radius in equation (78).

Reaction	KE_{Proj} MeV/n	σ mb	KE_{Frag} MeV/n	$\frac{d\sigma}{dT}$ mb $(MeV/n)^{-1}$			
			Proton	Deuteron	Triton	Helion	Alpha
He + C	1050	650	100	8.02379×10^{-1}	1.35996×10^{-1}	4.30049×10^{-3}	3.90611×10^{-4}
			300	6.84997×10^{-1}	1.87102×10^{-1}	7.17934×10^{-3}	7.84985×10^{-4}
			1050	3.90334×10^{-1}	6.59672×10^{-1}	4.50339×10^{-1}	8.88983×10^{-1}
			2000	9.64866×10^{-3}	2.28412×10^{-5}	2.33210×10^{-8}	7.05587×10^{-11}
C + C	800	3500	100	5.22544	4.82347×10^{-1}	2.18052×10^{-2}	2.48534×10^{-3}
			300	3.91629	3.88055×10^{-1}	1.94943×10^{-2}	2.52365×10^{-3}
			800	2.80294	7.57466×10^{-1}	3.89567×10^{-1}	2.47779
			2000	1.01938×10^{-2}	2.72423×10^{-5}	8.24000×10^{-8}	5.30612×10^{-10}
Ar + KCl	800	16000	100	2.38877×10^{1}	6.31091	7.19047×10^{-1}	1.46325×10^{-1}
			300	1.79030×10^{1}	4.90425	5.98521×10^{-1}	1.40162×10^{-1}
			800	$1.28134\text{E}\times 10^{1}$	5.56050	7.34324	1.22436×10^{2}
			2000	4.66003×10^{-2}	1.08598×10^{-4}	8.68460×10^{-7}	1.73140×10^{-8}

Table 7: Sample results. KE_{Proj} = Kinetic energy of projectile. KE_{Frag} = Kinetic energy of fragment.

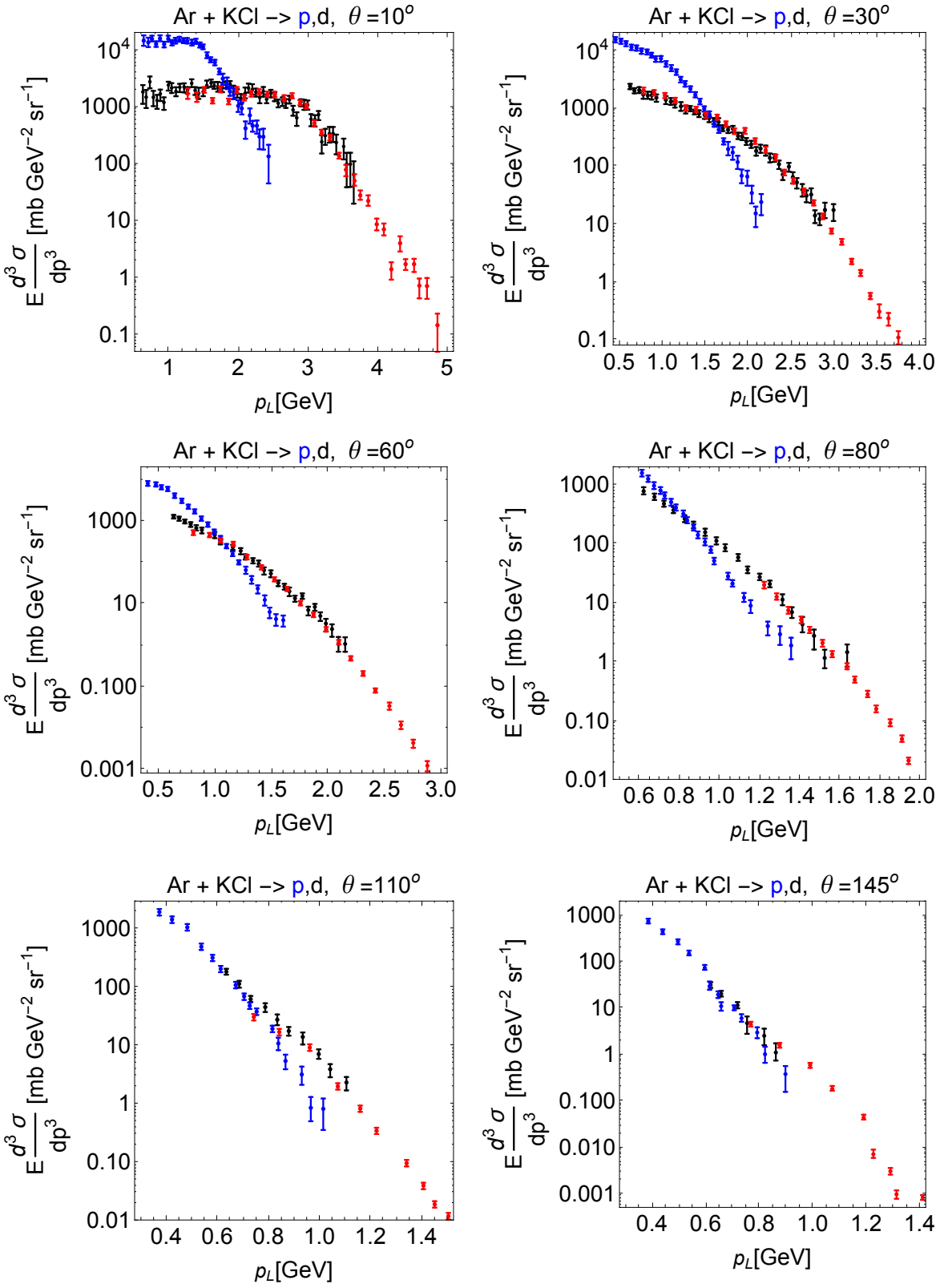

Figure 1: Deuteron (black) and proton production (blue) experimental [13] Lorentz-invariant double-differential cross-sections as a function of lab momentum for 800 MeV/n Ar + KCl reactions at various production angles. The proton cross-sections have been scaled (red) using the coalescence model of equation (1), with the coalescence coefficient $C_A = 8 \times 10^{-6}$ taken from experimental values listed in Table VIII of reference [13]. Axes use units of GeV and plots are the same as reference [12].

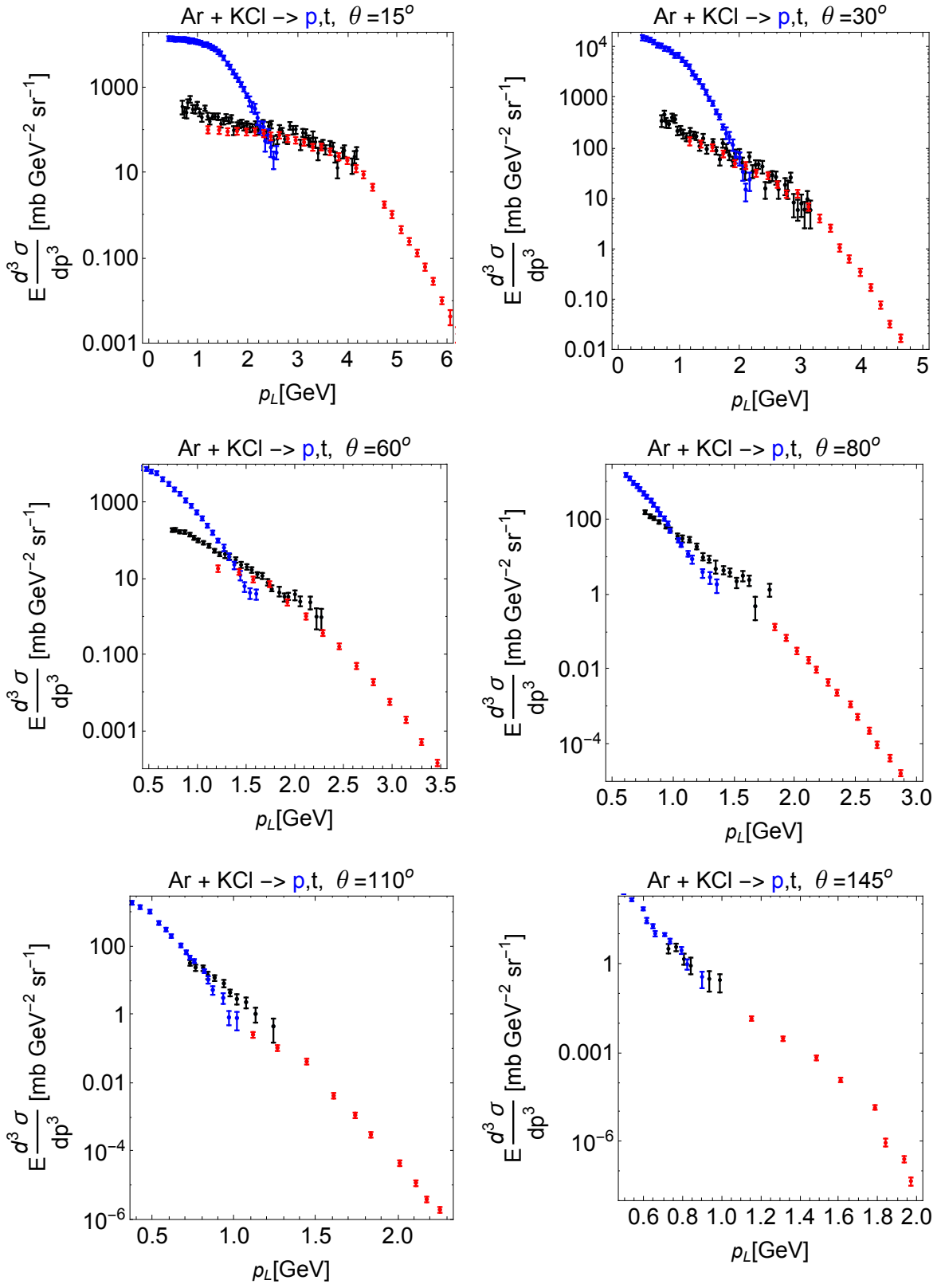

Figure 2: Triton (black) and proton production (blue) experimental [13] Lorentz-invariant double-differential cross-sections as a function of lab momentum for 800 MeV/n Ar + KCl reactions at various production angles. The proton cross-sections have been scaled (red) using the coalescence model of equation (1), with the coalescence coefficient $C_A = 3.5 \times 10^{-11}$ taken from experimental values listed in Table VIII of reference [13]. Axes use units of GeV and plots are the same as reference [12].

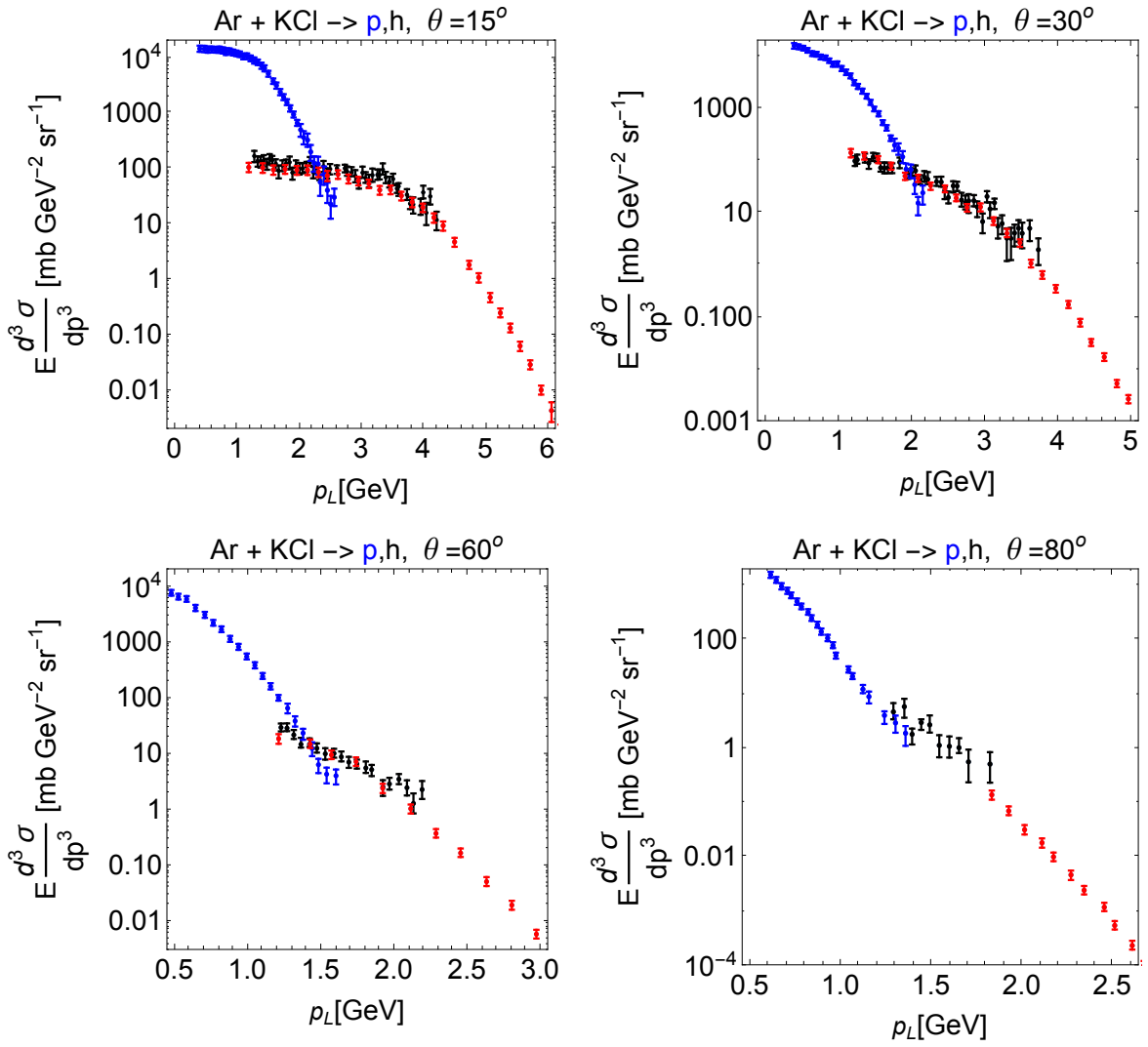

Figure 3: Helion (black) and proton production (blue) experimental [13] Lorentz-invariant double-differential cross-sections as a function of lab momentum for 800 MeV/n Ar + KCl reactions at various production angles. The proton cross-sections have been scaled (red) using the coalescence model of equation (1), with the coalescence coefficient $C_A = 3.5 \times 10^{-11}$ taken from experimental values listed in Table VIII of reference [13]. Axes use units of GeV and plots are the same as reference [12].

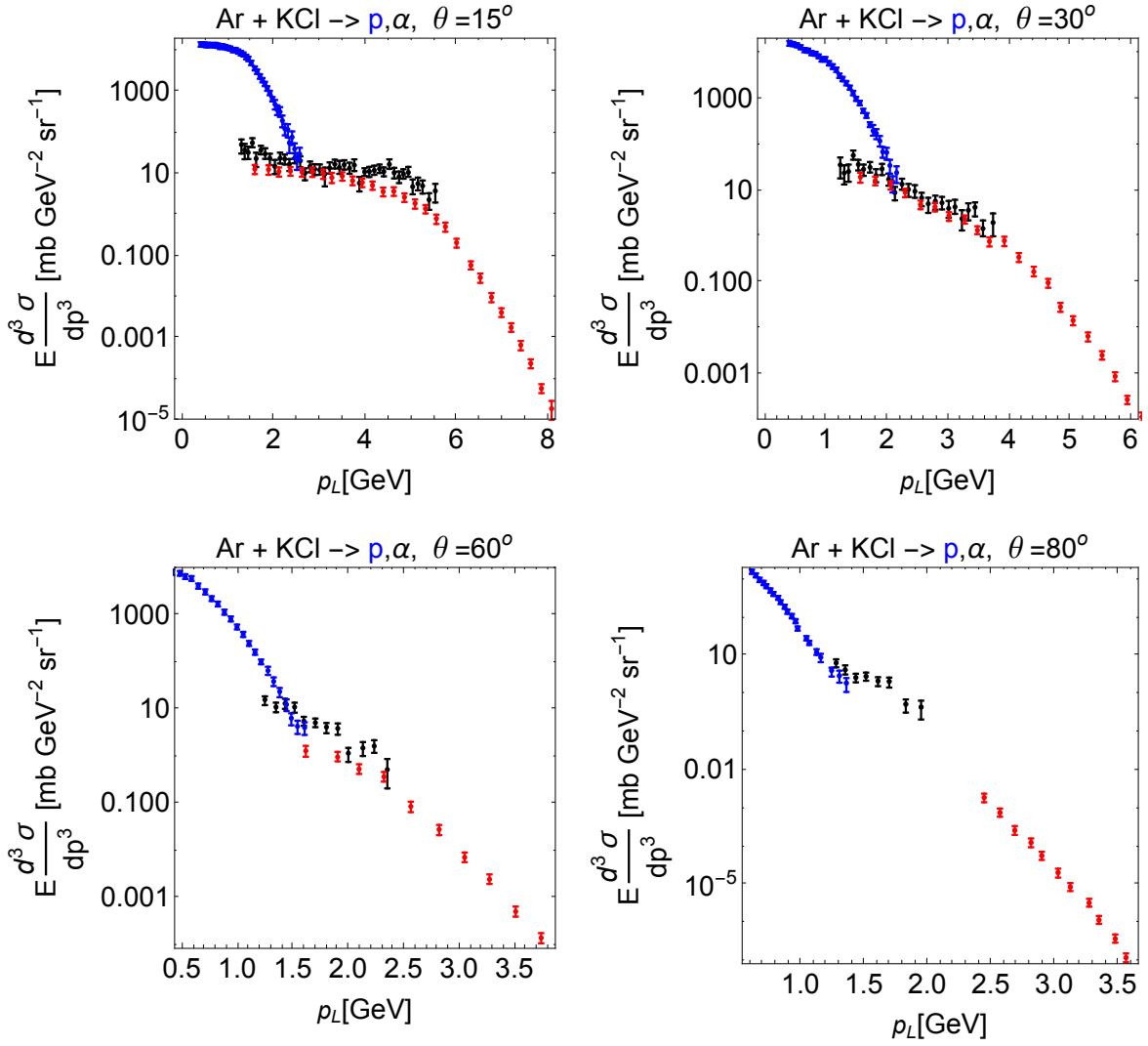

Figure 4: Alpha (black) and proton production (blue) experimental [13] Lorentz-invariant double-differential cross-sections as a function of lab momentum for 800 MeV/n Ar + KCl reactions at various production angles. The proton cross-sections have been scaled (red) using the coalescence model of equation (1), with the coalescence coefficient $C_A = 3\times10^{-16}$ taken from experimental values listed in Table VIII of reference [13]. Axes use units of GeV and plots are the same as reference [12].

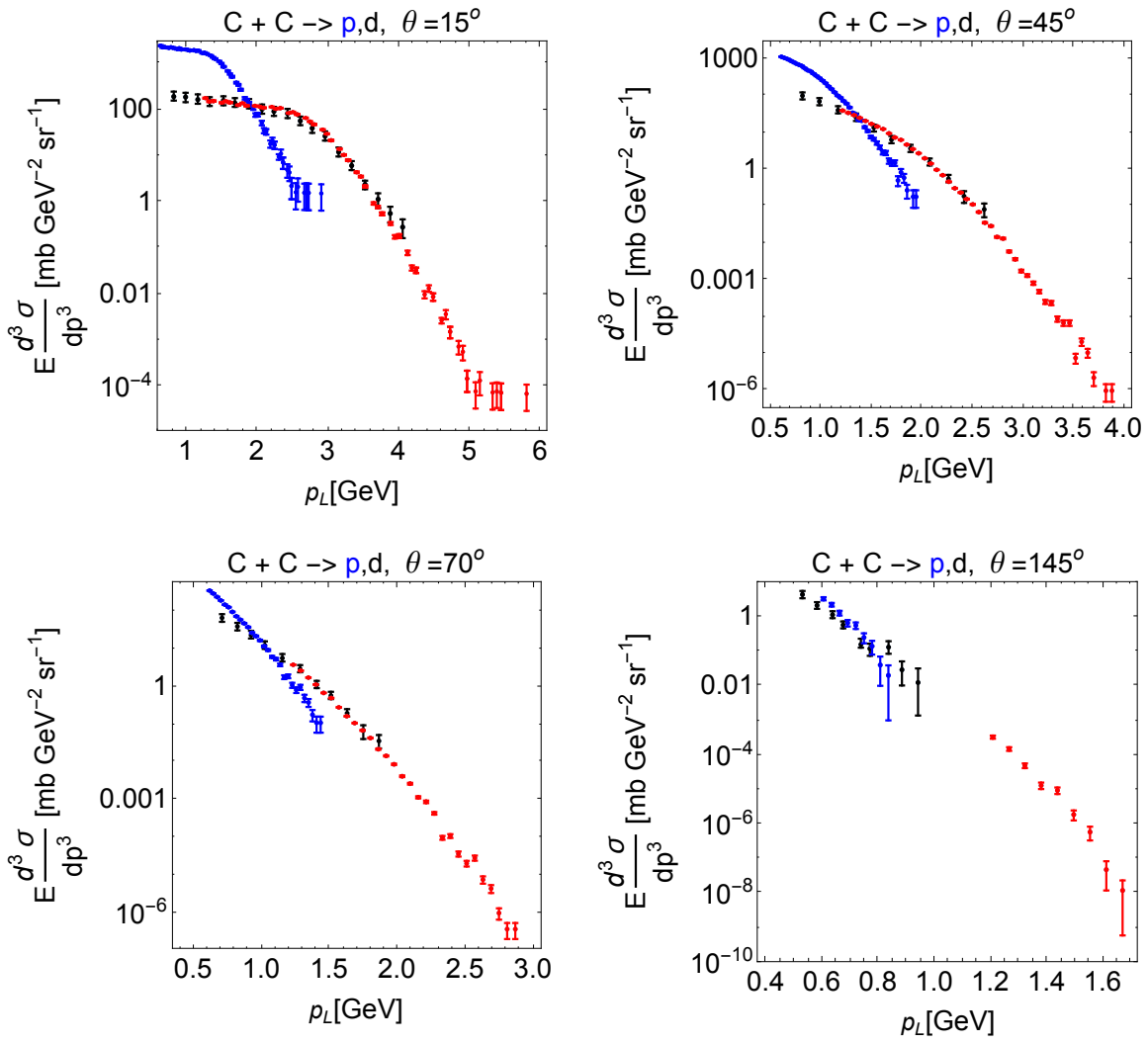

Figure 5: Deuteron (black) and proton production (blue) experimental [13, 14] Lorentz-invariant double-differential cross-sections as a function of lab momentum for 800 MeV/n C + C reactions at various production angles. The proton cross-sections have been scaled (red) using the coalescence model of equation (1), with the coalescence coefficient $C_A = 3 \times 10^{-5}$ taken from experimental values listed in Table VIII of reference [13]. Axes use units of GeV and plots are the same as reference [12].

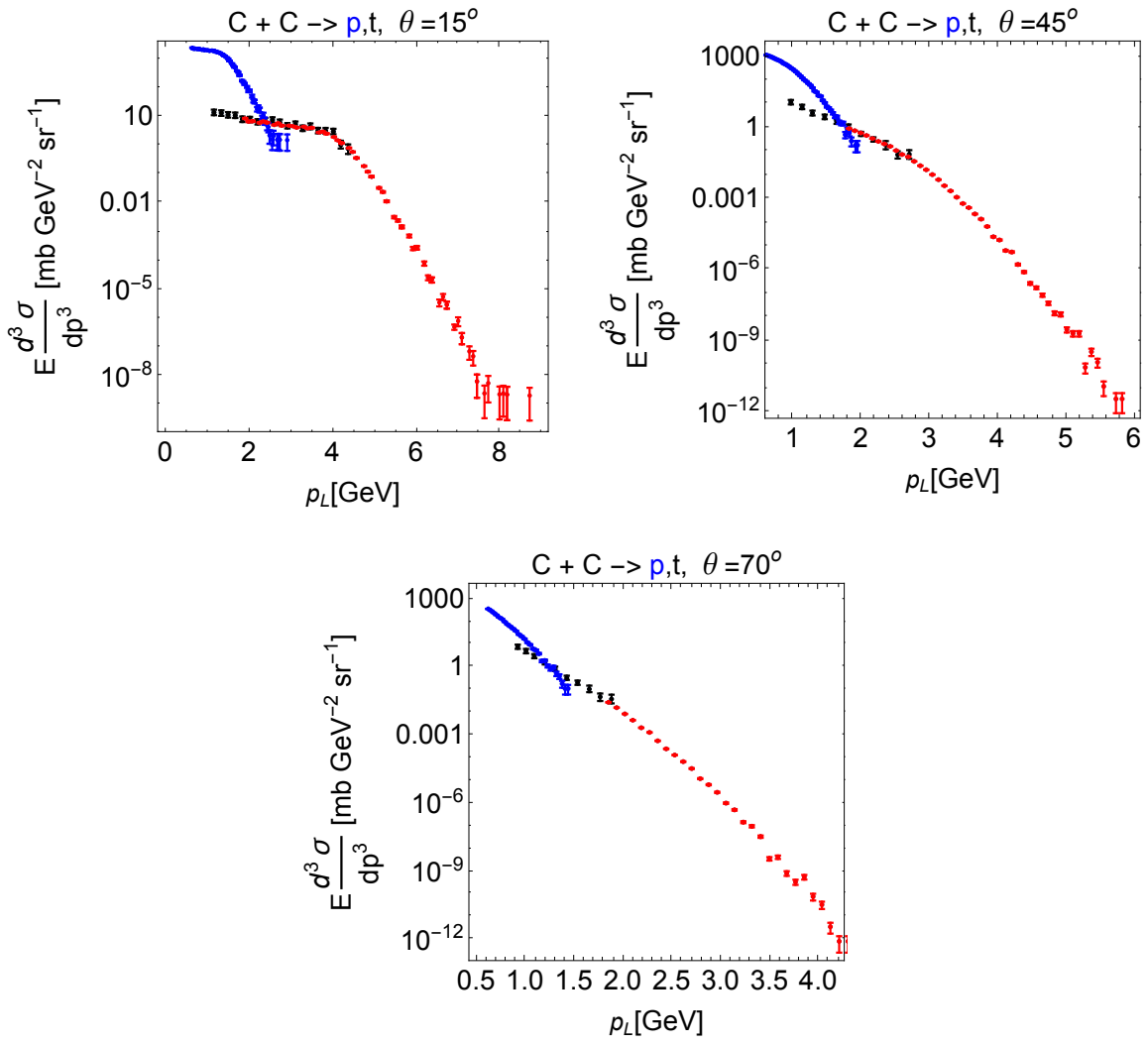

Figure 6: Triton (black) and proton production (blue) experimental [13, 14] Lorentz-invariant double-differential cross-sections as a function of lab momentum for 800 MeV/n C + C reactions at various production angles. The proton cross-sections have been scaled (red) using the coalescence model of equation (1), with the coalescence coefficient $C_A = 6 \times 10^{-10}$ taken from experimental values listed in Table VIII of reference [13]. Axes use units of GeV and plots are the same as reference [12].

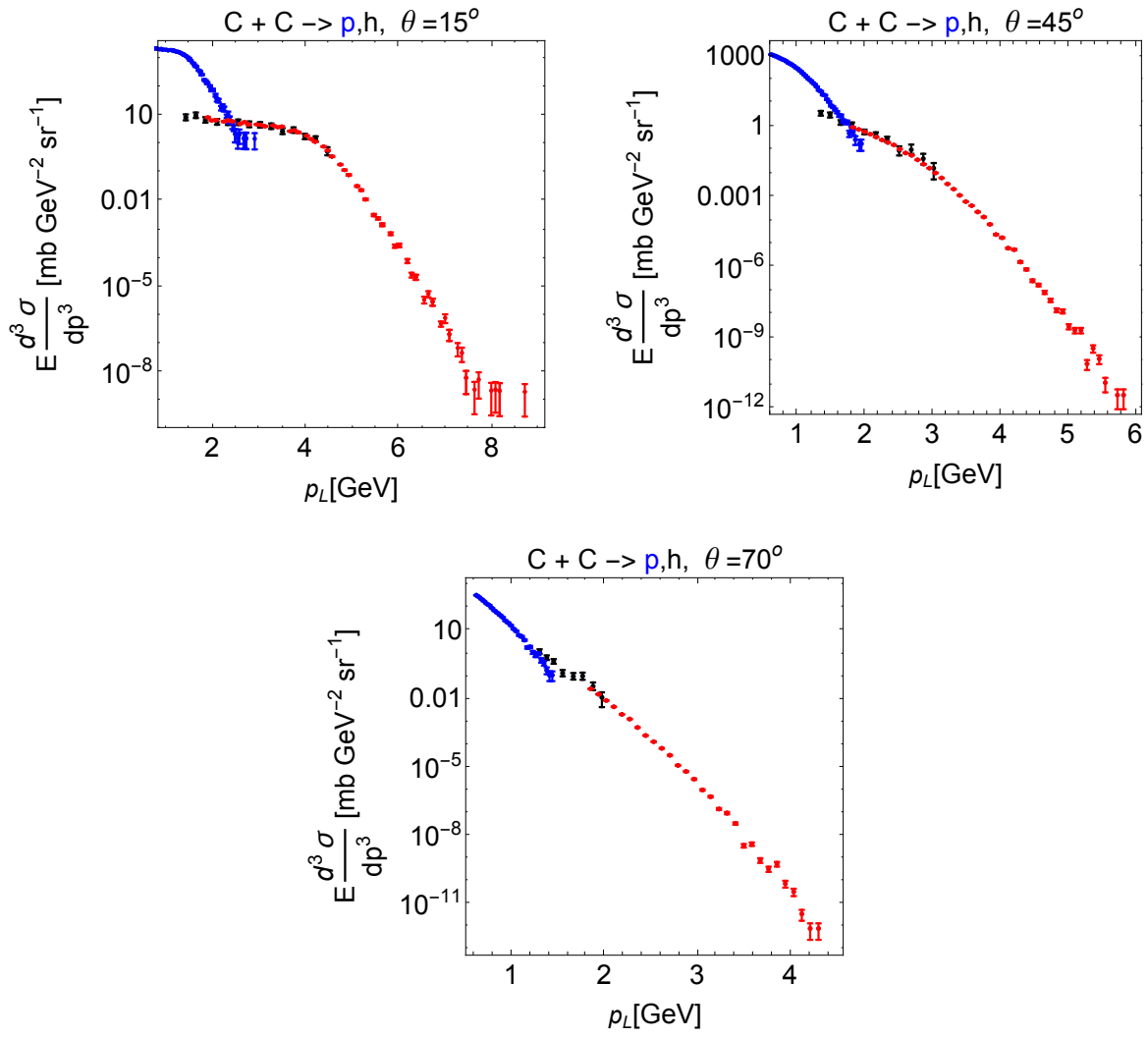

Figure 7: Helion (black) and proton production (blue) experimental [13, 14] Lorentz-invariant double-differential cross-sections as a function of lab momentum for 800 MeV/n C + C reactions at various production angles. The proton cross-sections have been scaled (red) using the coalescence model of equation (1), with the coalescence coefficient $C_A = 6 \times 10^{-10}$ taken from experimental values listed in Table VIII of reference [13]. Axes use units of GeV and plots are the same as reference [12].

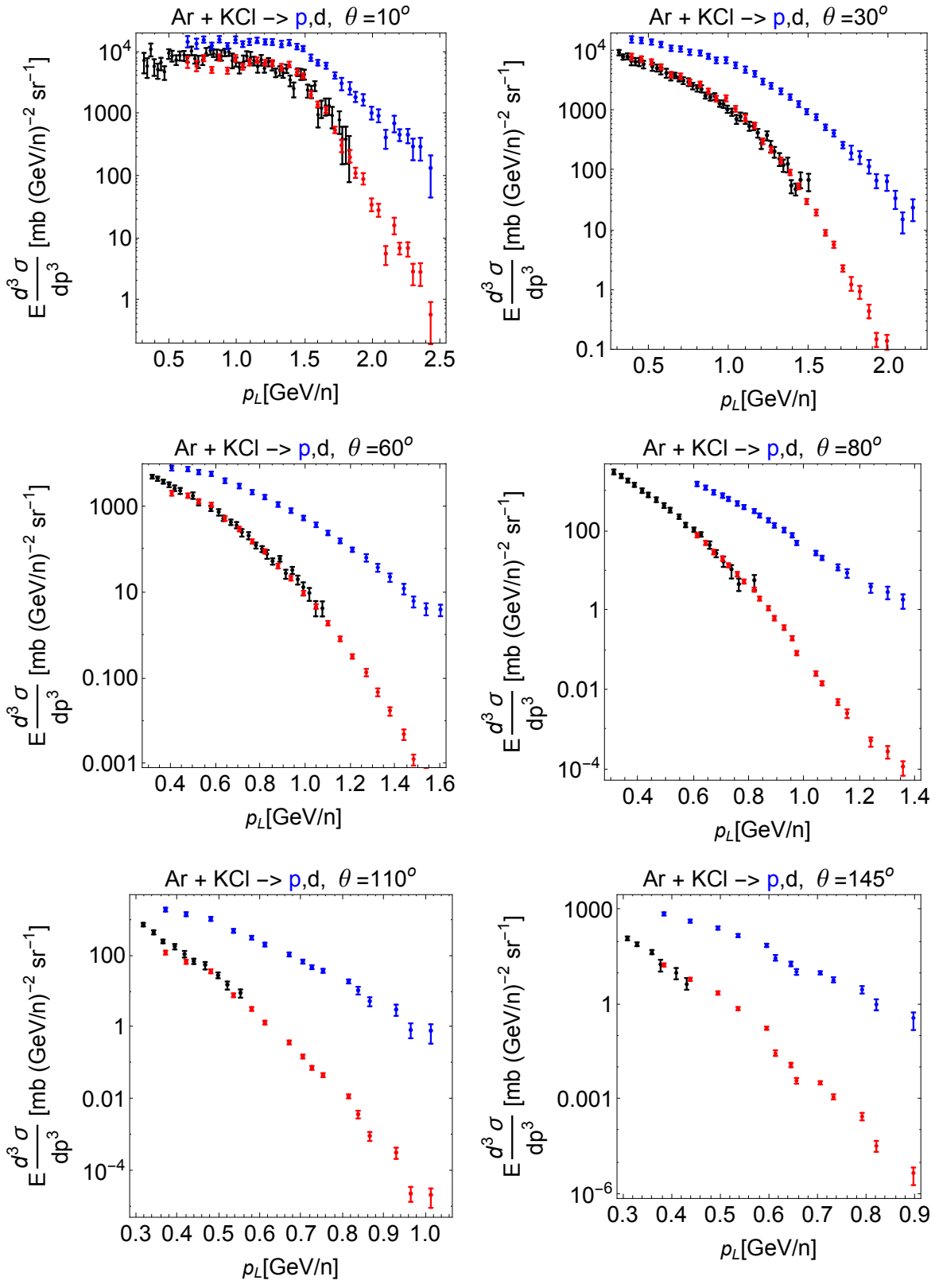

Figure 8: Same as Figure 1, except axes use units of GeV/n.

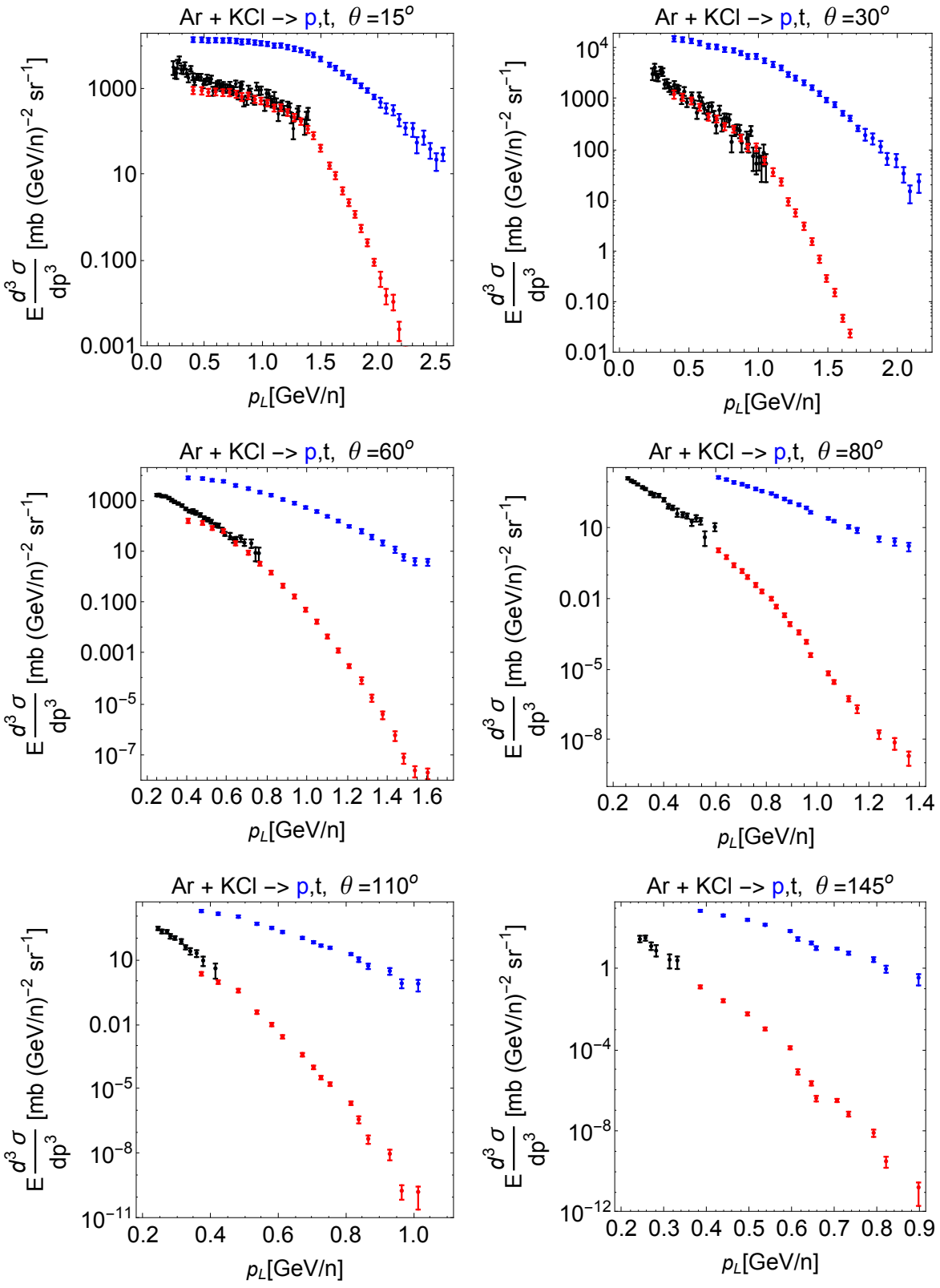

Figure 9: Same as Figure 2, except axes use units of GeV/n.

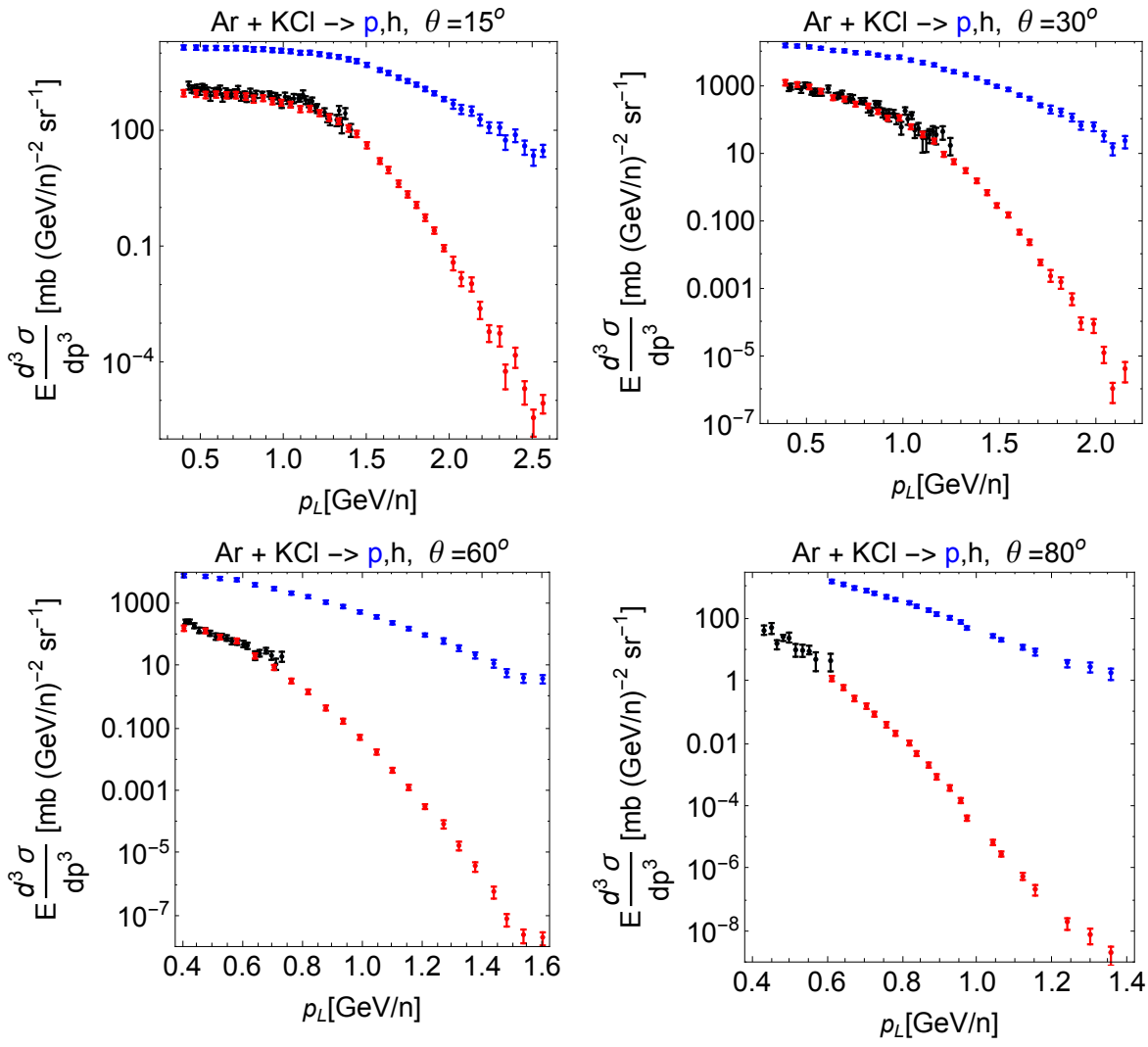

Figure 10: Same as Figure 3, except axes use units of GeV/n.

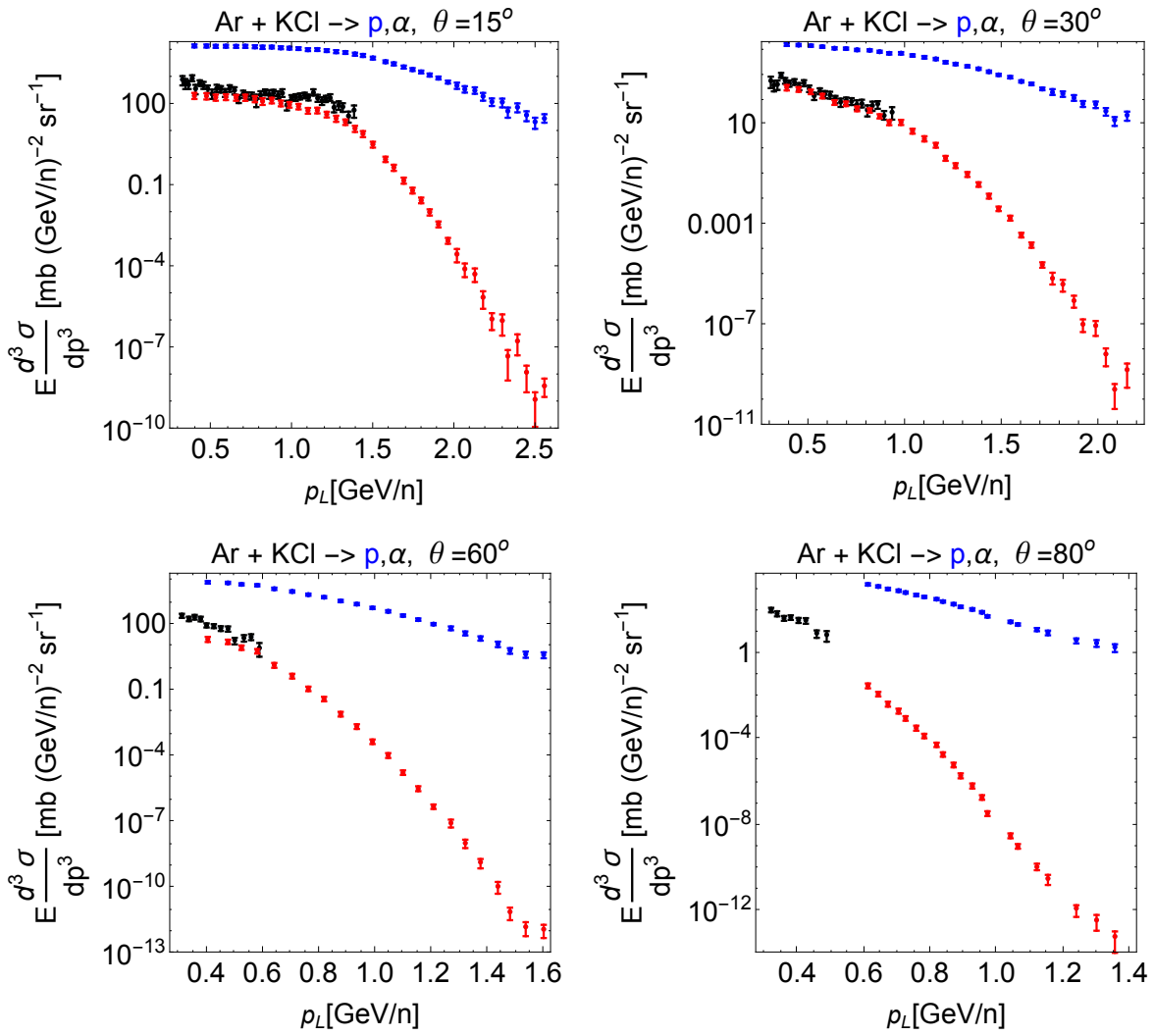

Figure 11: Same as Figure 4, except axes use units of GeV/n.

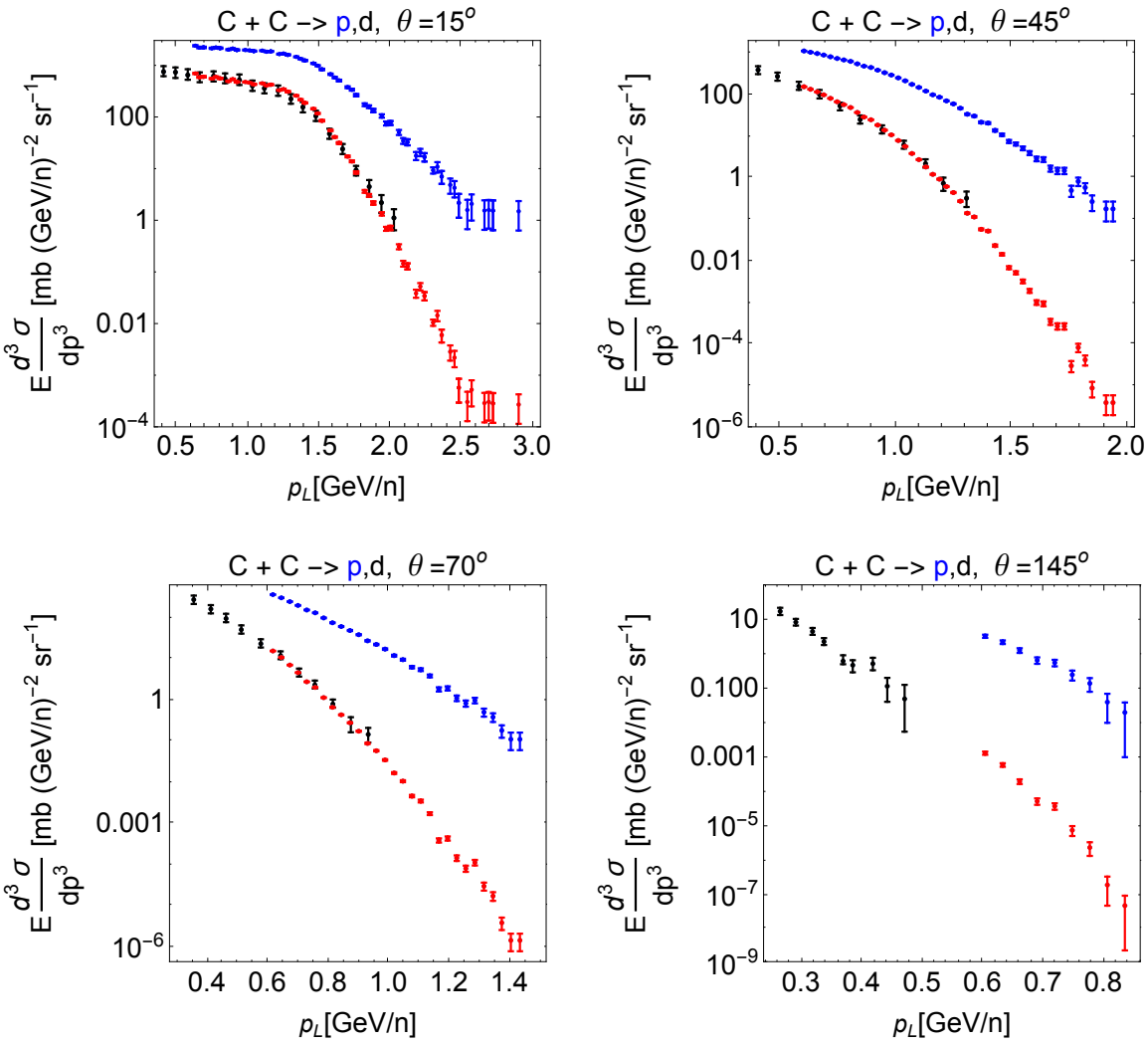

Figure 12: Same as Figure 5, except axes use units of GeV/n.

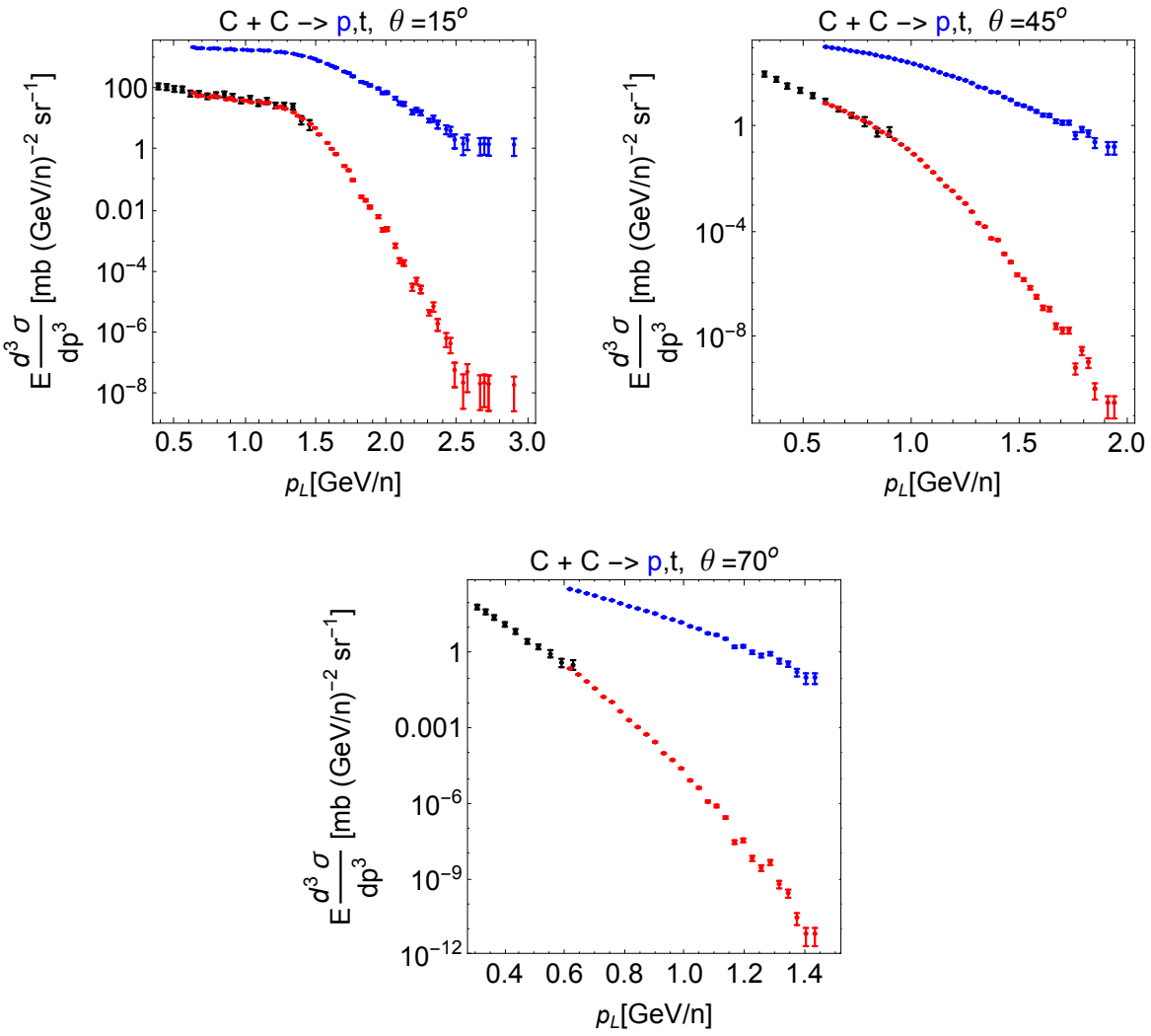

Figure 13: Same as Figure 6, except axes use units of GeV/n.

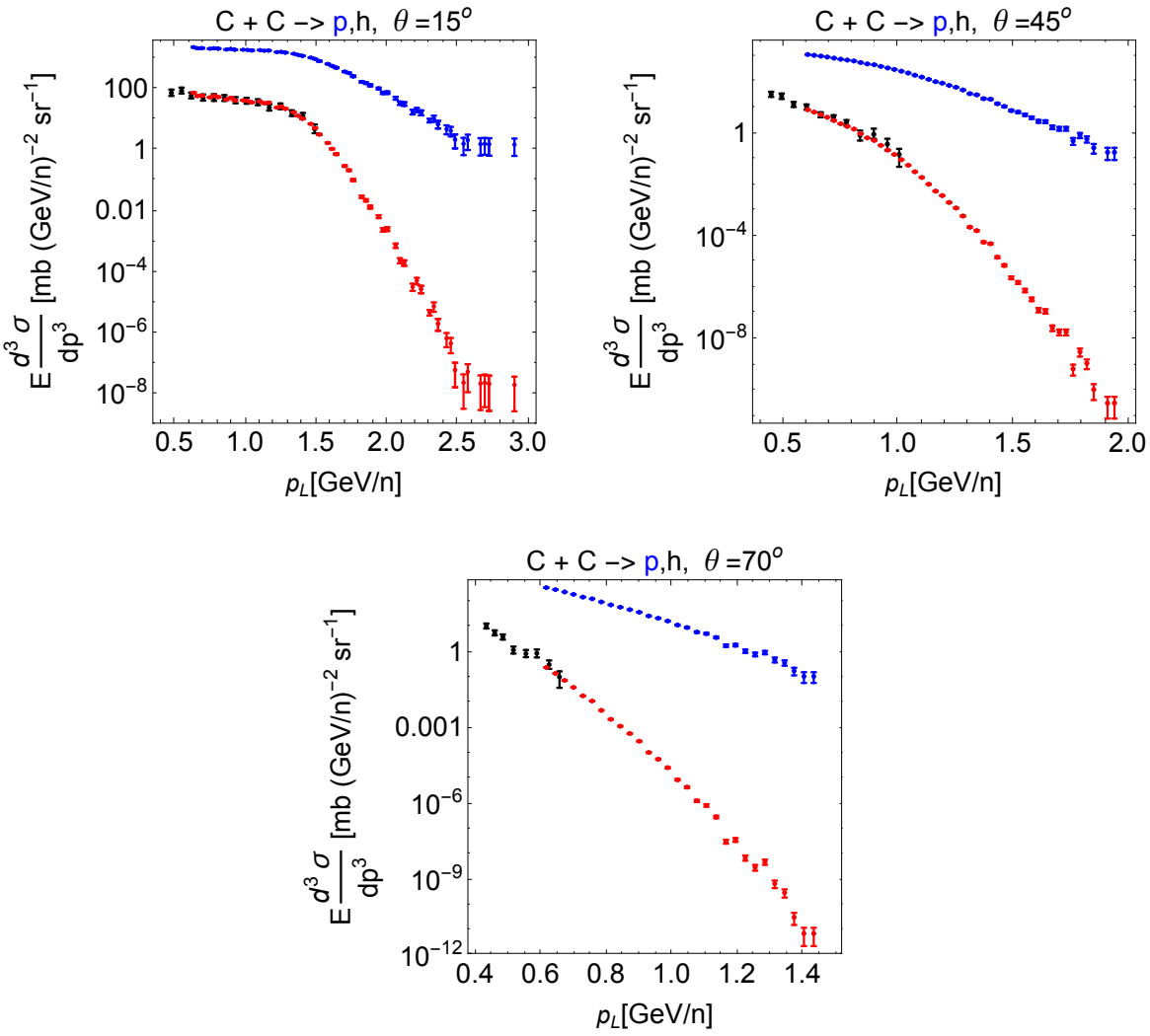

Figure 14: Same as Figure 7, except axes use units of GeV/n.

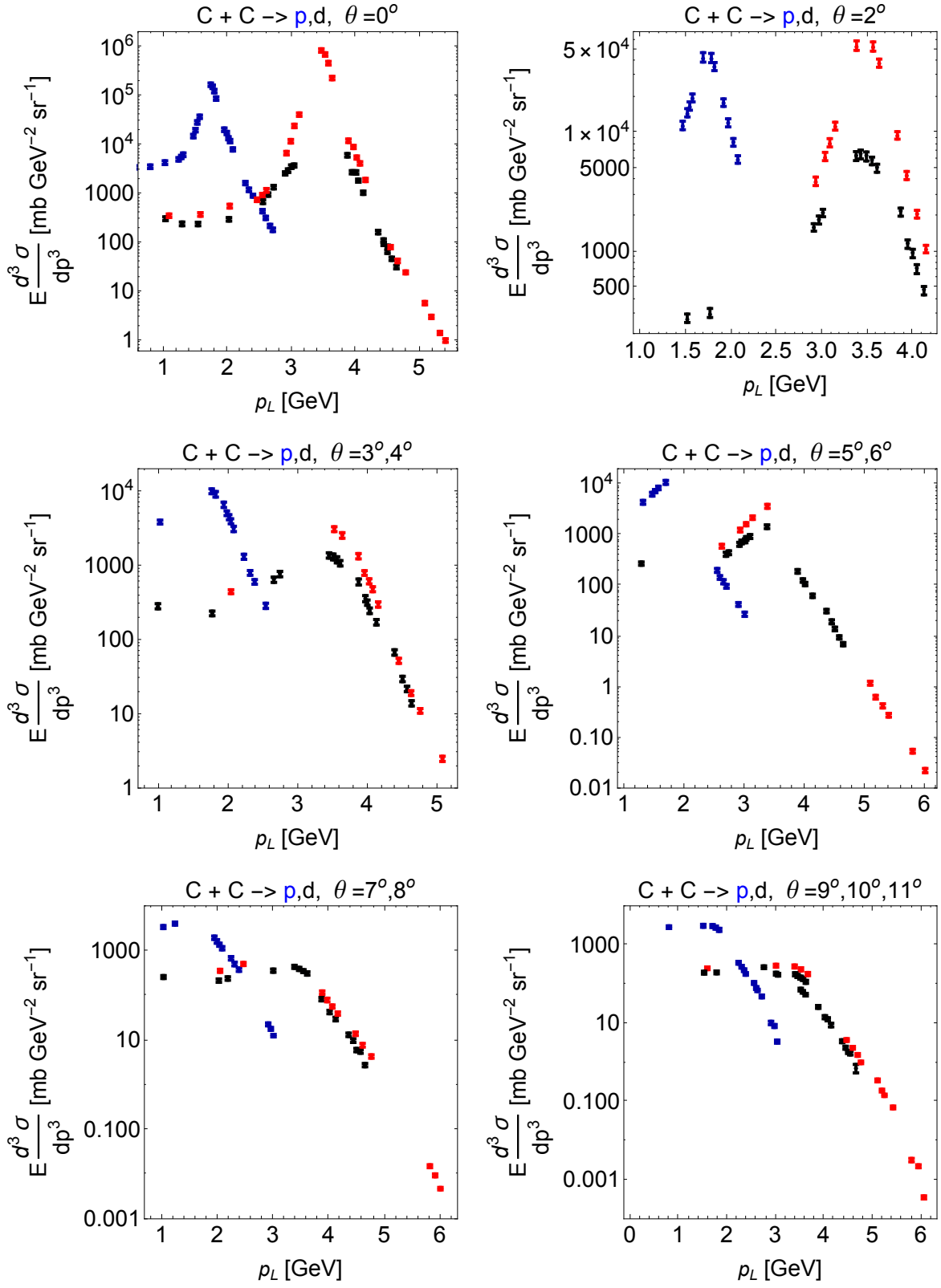

Figure 15: Deuteron (black) and proton production (blue) experimental [16] Lorentz-invariant double-differential cross-sections as a function of lab momentum for 1.05 GeV/n C + C reactions at various production angles. The angular display of the Anderson et al. [16] data, is obtained with the methods discussed in sections 1.2 and 7. The proton cross-sections have been scaled (red) using the coalescence model of equation (1), with the coalescence coefficient $C_A = 3 \times 10^{-5}$ taken from 800 MeV/n experimental values listed in Table VIII of reference [13]. Axes use units of GeV.

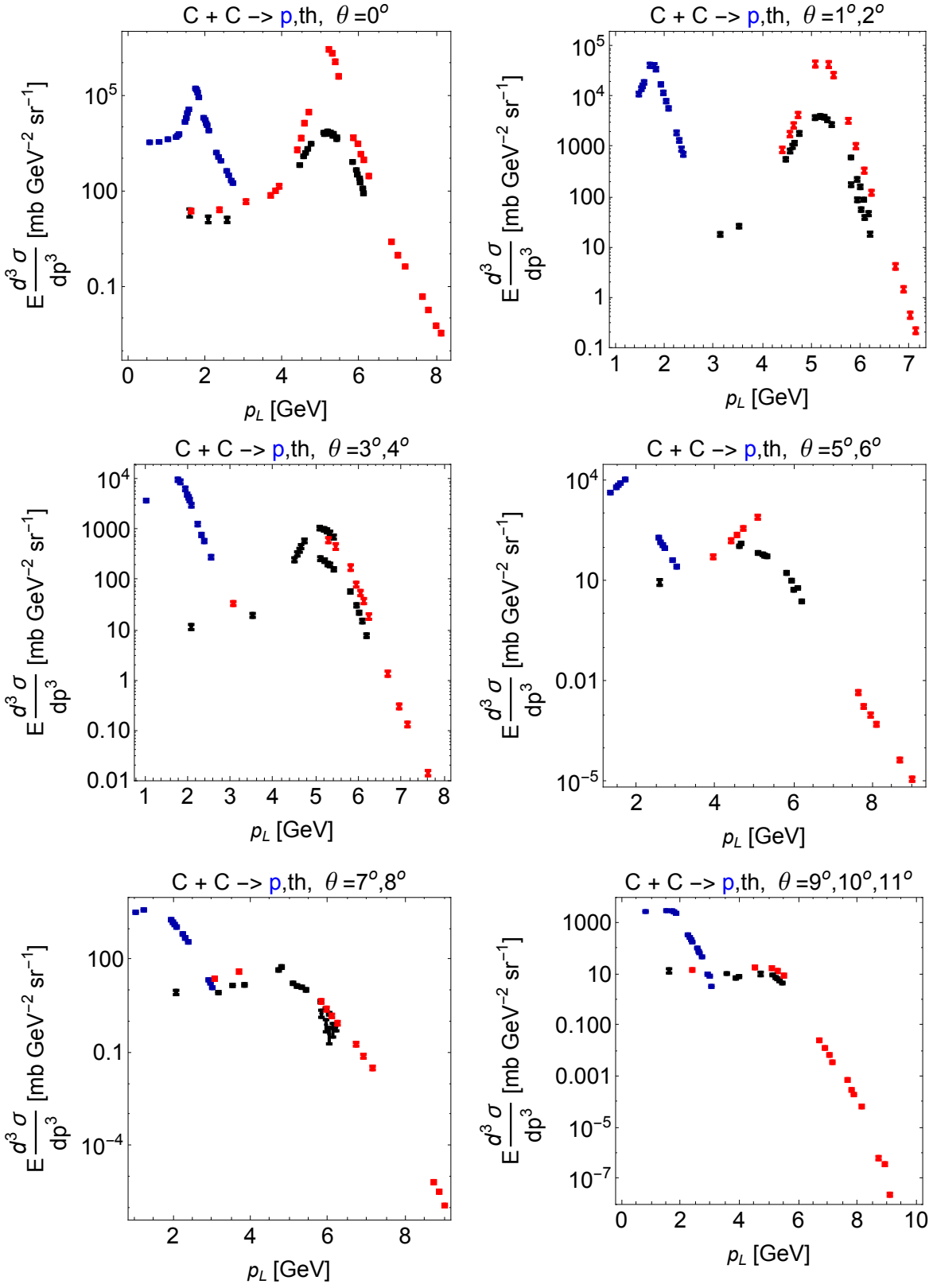

Figure 16: Triton or Helion (black) and proton production (blue) experimental [16] Lorentz-invariant double-differential cross-sections as a function of lab momentum for 1.05 GeV/n C + C reactions at various production angles. The angular display of the Anderson et al. [16] data, is obtained with the methods discussed in sections 1.2 and 7. The proton cross-sections have been scaled (red) using the coalescence model of equation (1), with the coalescence coefficient $C_A = 6 \times 10^{-10}$ taken from 800 MeV/n experimental values listed in Table VIII of reference [13]. Axes use units of GeV.

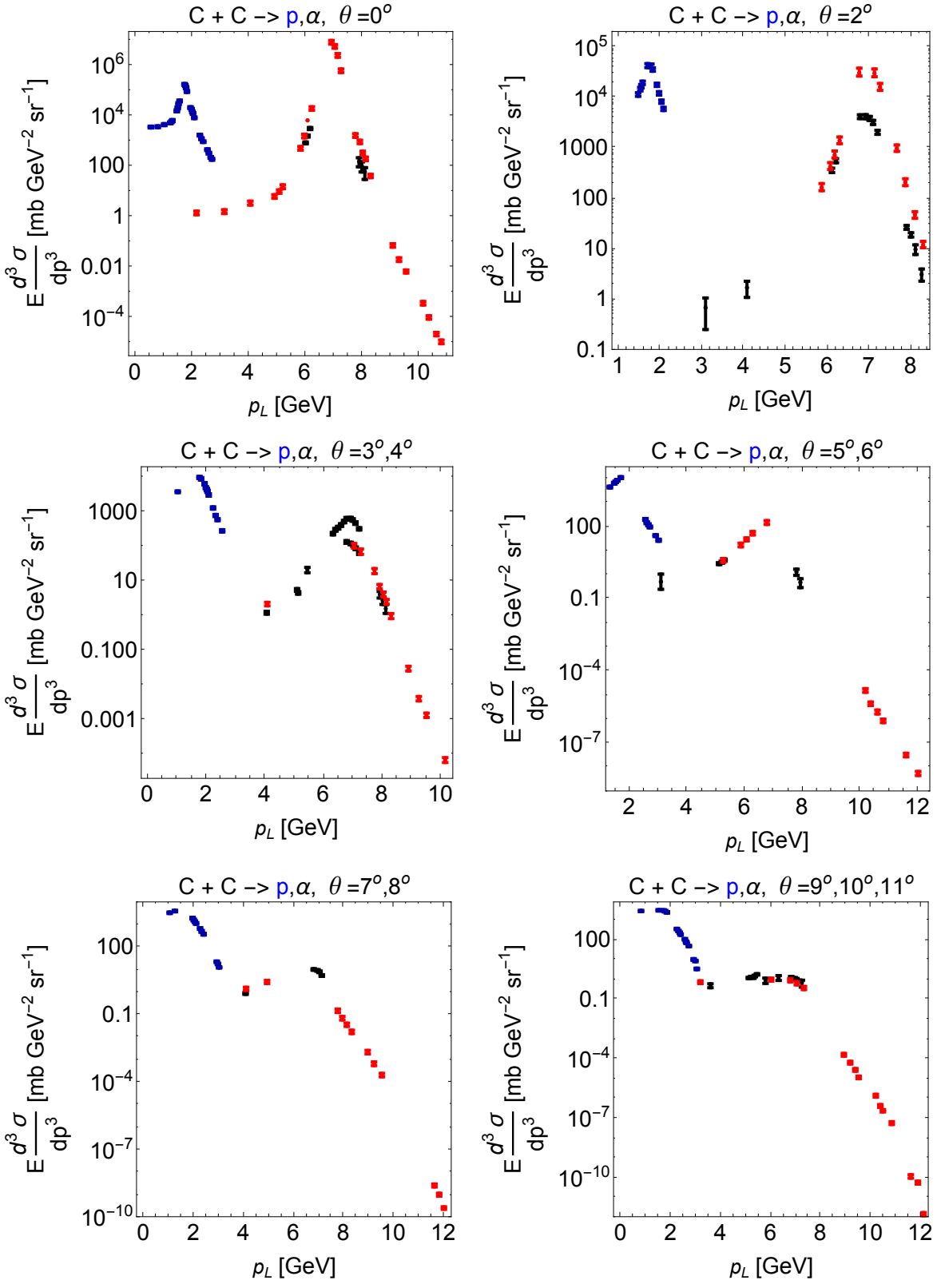

Figure 17: Alpha (black) and proton production (blue) experimental [16] Lorentz-invariant double-differential cross-sections as a function of lab momentum for 1.05 GeV/n C + C reactions at various production angles. The angular display of the Anderson et al. [16] data, is obtained with the methods discussed in sections 1.2 and 7. The proton cross-sections have been scaled (red) using the coalescence model of equation (1), with the coalescence coefficient $C_A = 1 \times 10^{-14}$. Axes use units of GeV.

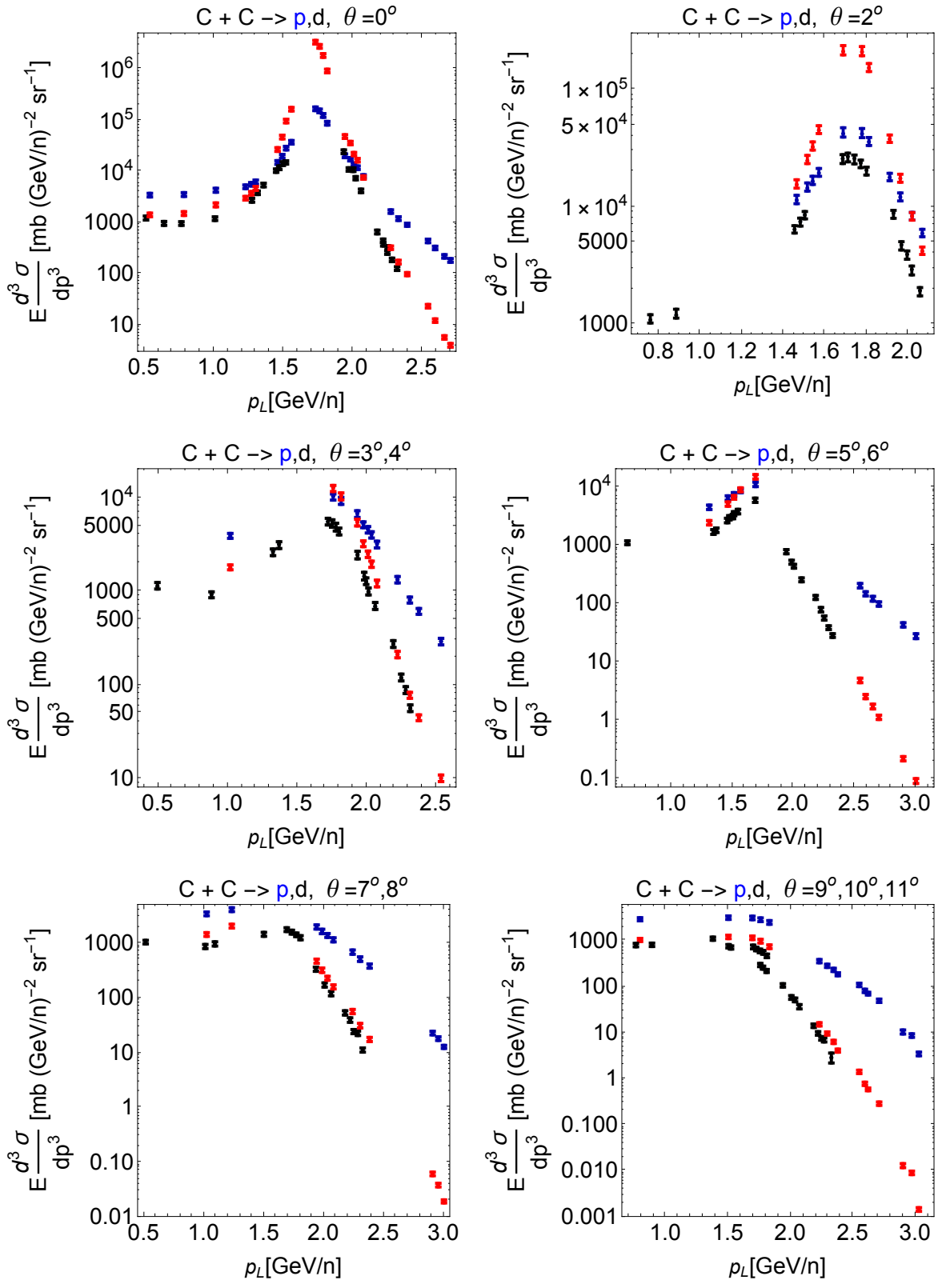

Figure 18: Same as Figure 15, except axes use units of GeV/n.

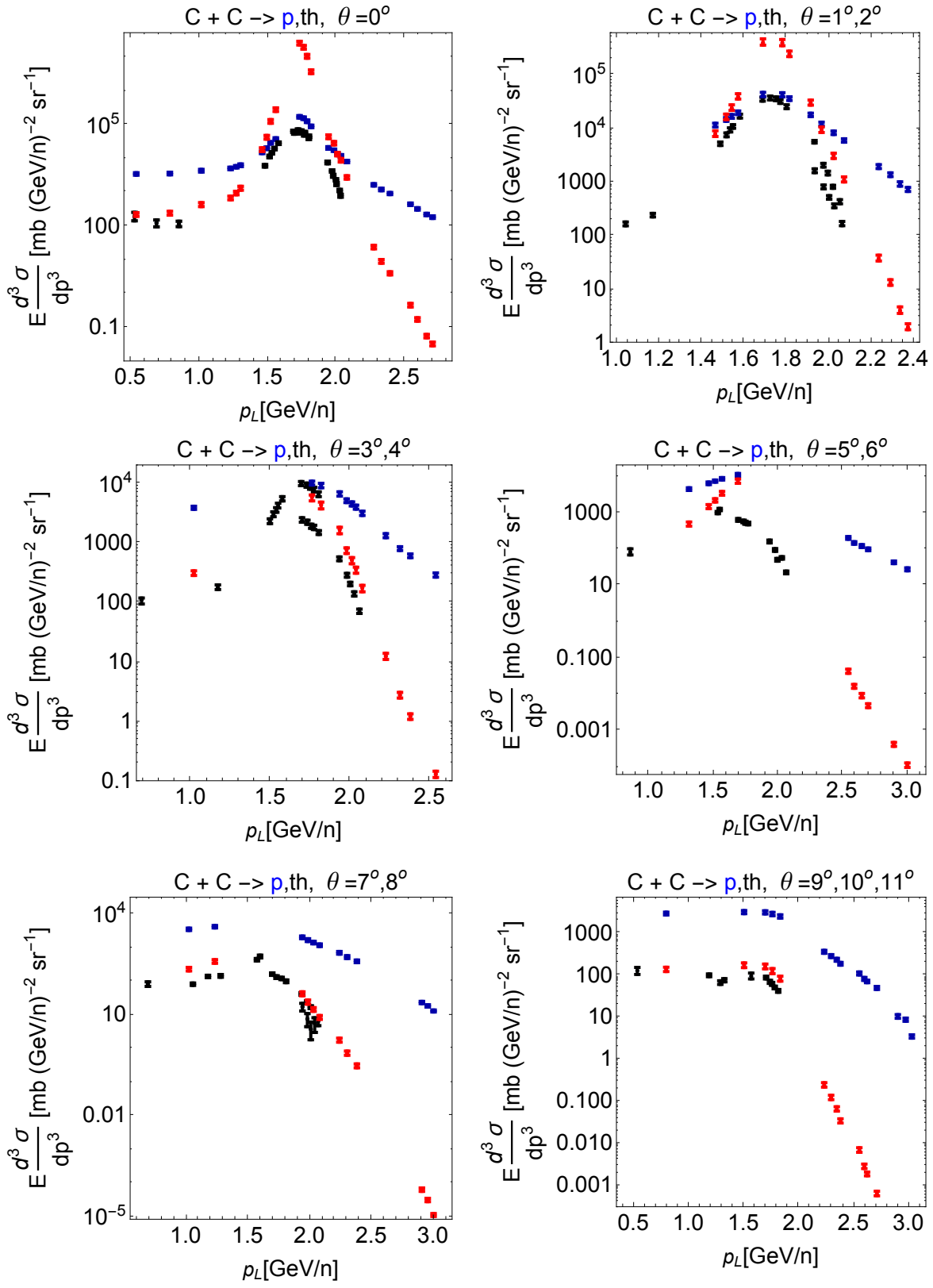

Figure 19: Same as Figure 16, except axes use units of GeV/n.

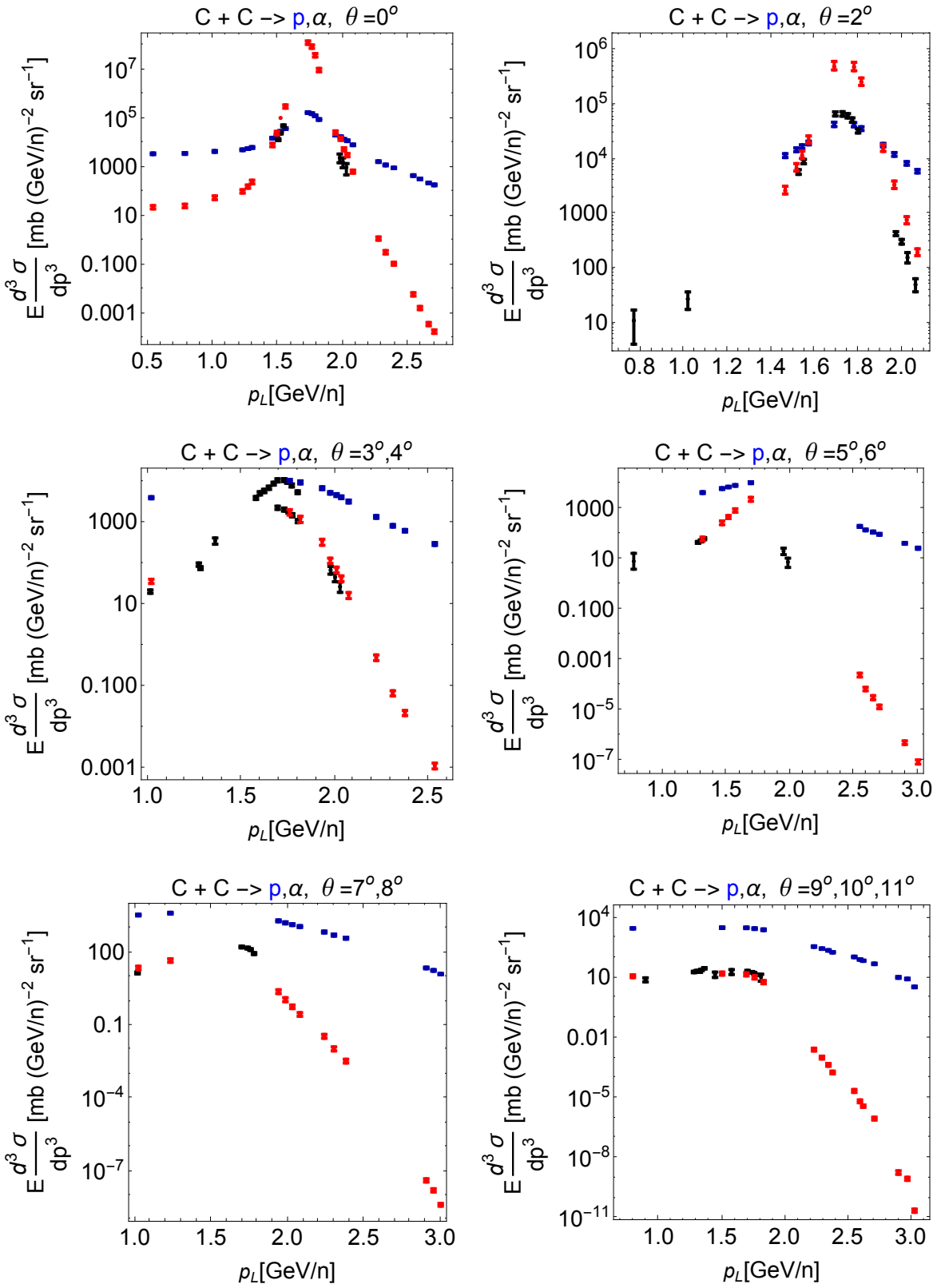

Figure 20: Same as Figure 17, except axes use units of GeV/n.

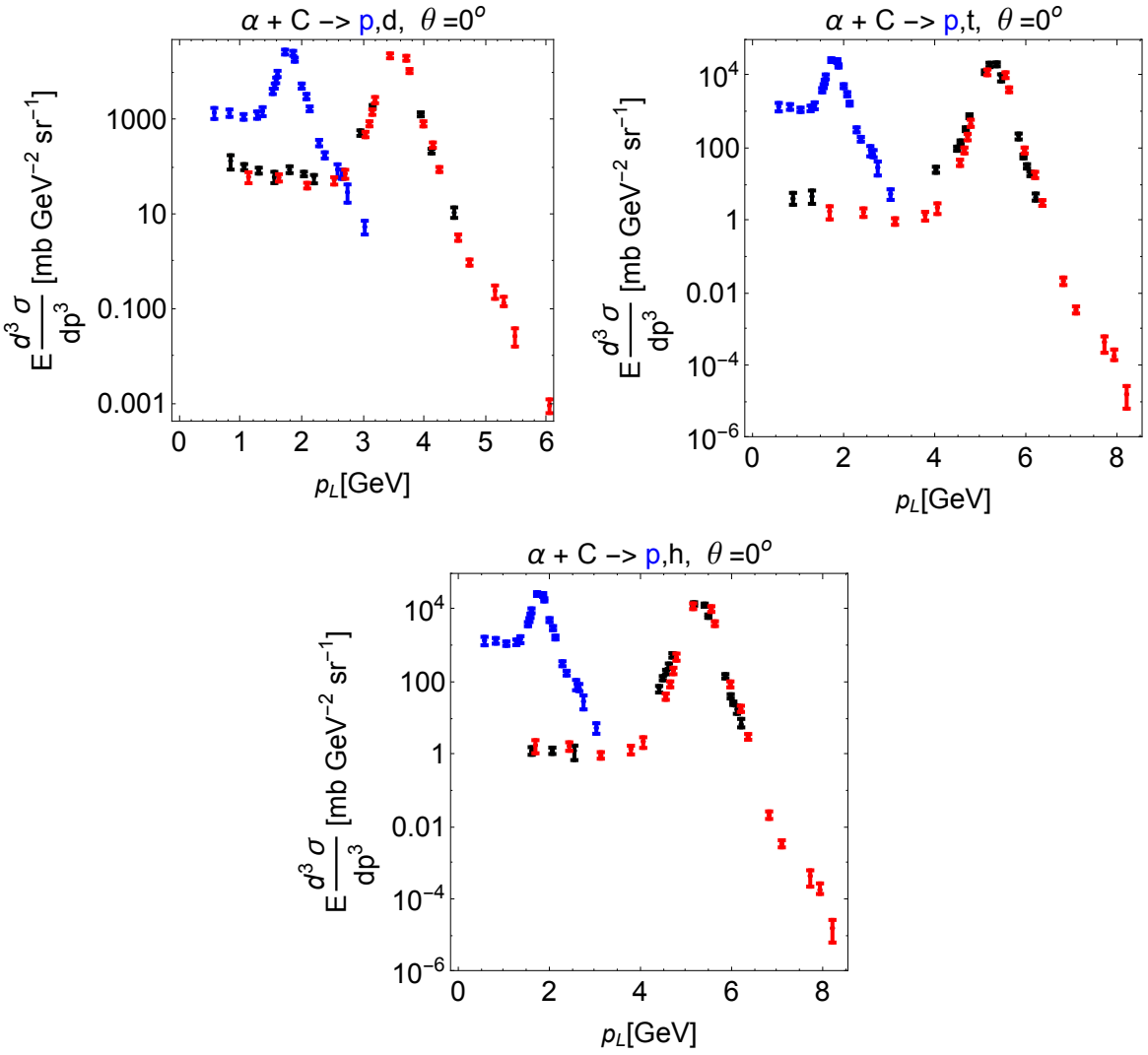

Figure 21: Deuteron, triton, helion (black) and proton (blue) experimental [16] Lorentz-invariant double-differential cross-sections as a function of lab momentum for 1.05 GeV/n α + C reactions. Fragments are produced at an angle of 0°. The proton cross-sections have been scaled (red) using the coalescence model of equation (1), with the coalescence coefficients $C_A = 3 \times 10^{-5}$ (deuteron) and $C_A = 6 \times 10^{-10}$ (triton, helion) taken from 800 MeV/n experimental values listed in Table VIII of reference [13]. Axes use units of GeV.

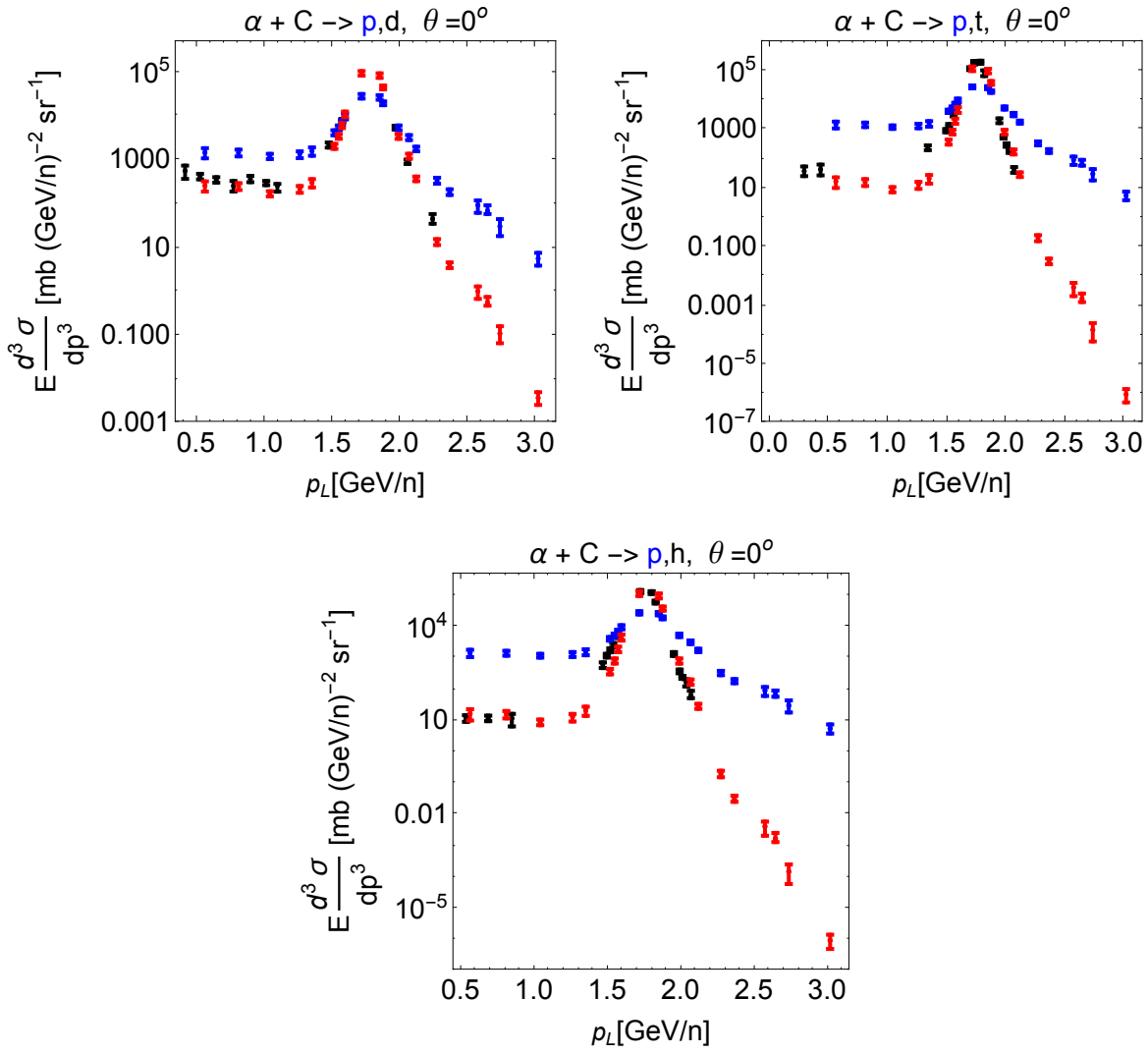

Figure 22: Same as Figure 21, except axes use units of GeV/n.

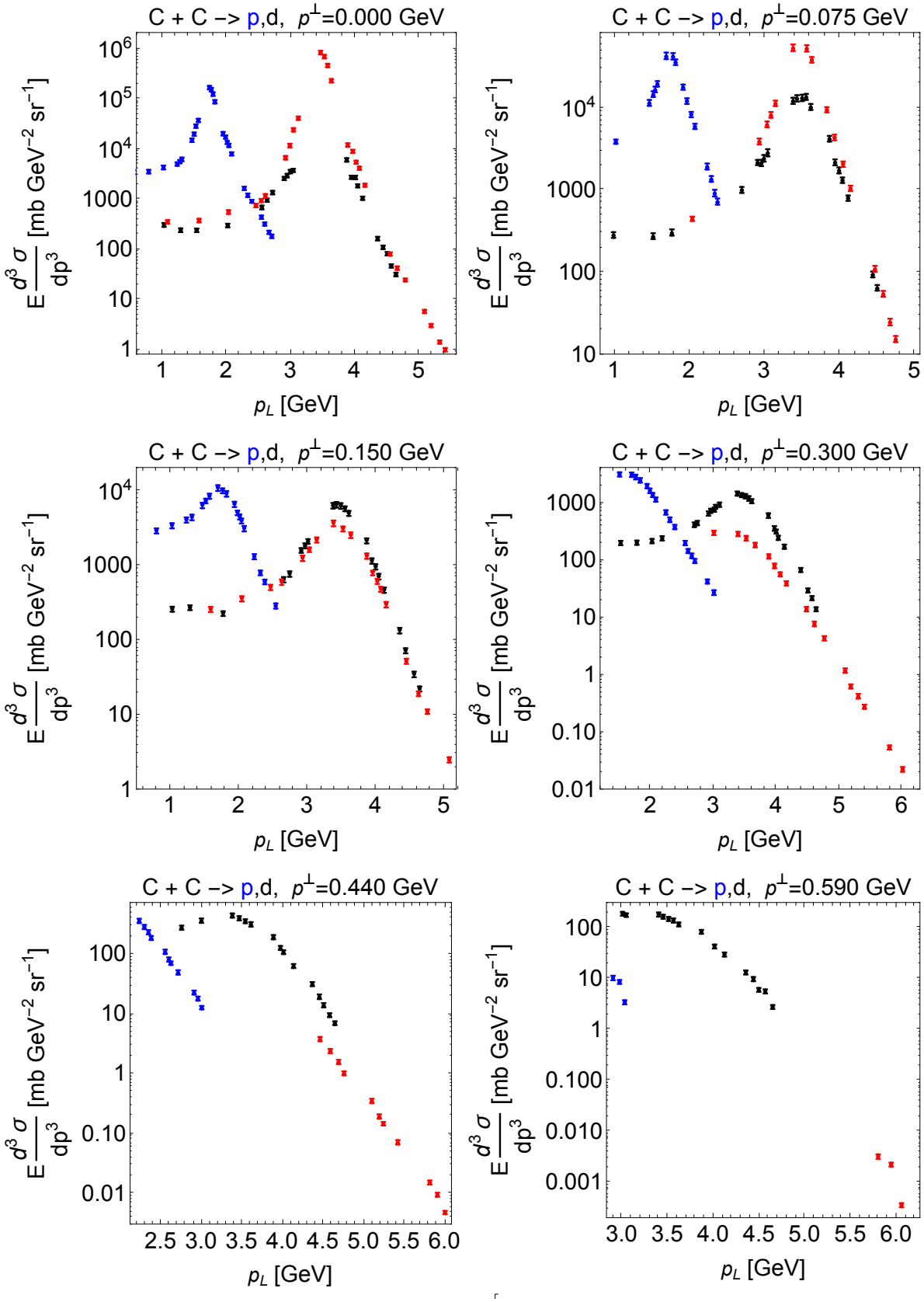

Figure 23: Same as Figure 15, except plot frames are ordered by transverse momentum, $p^{\perp}$, instead of angle.

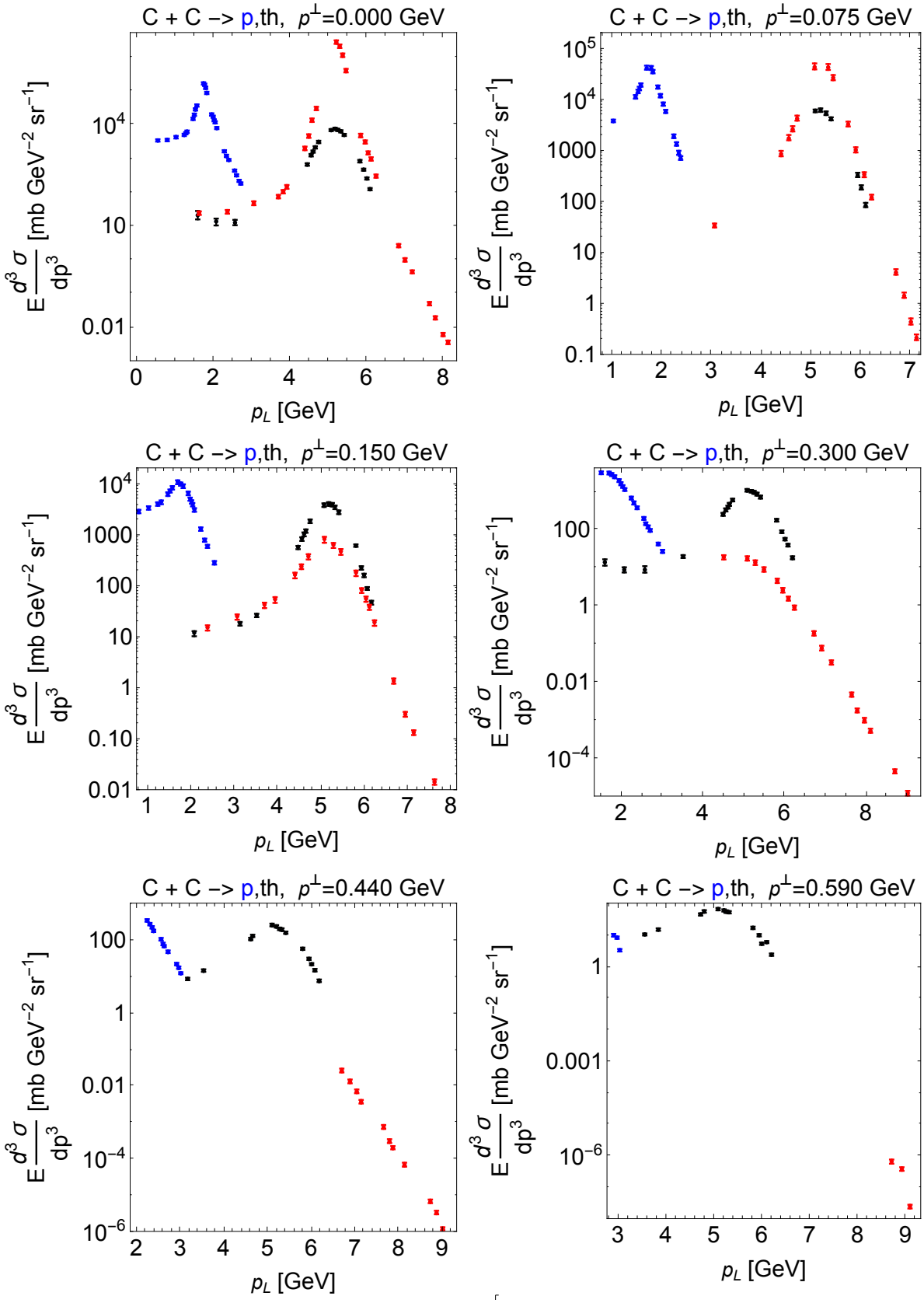

Figure 24: Same as Figure 16, except plot frames are ordered by transverse momentum, $p^{\perp}$, instead of angle.

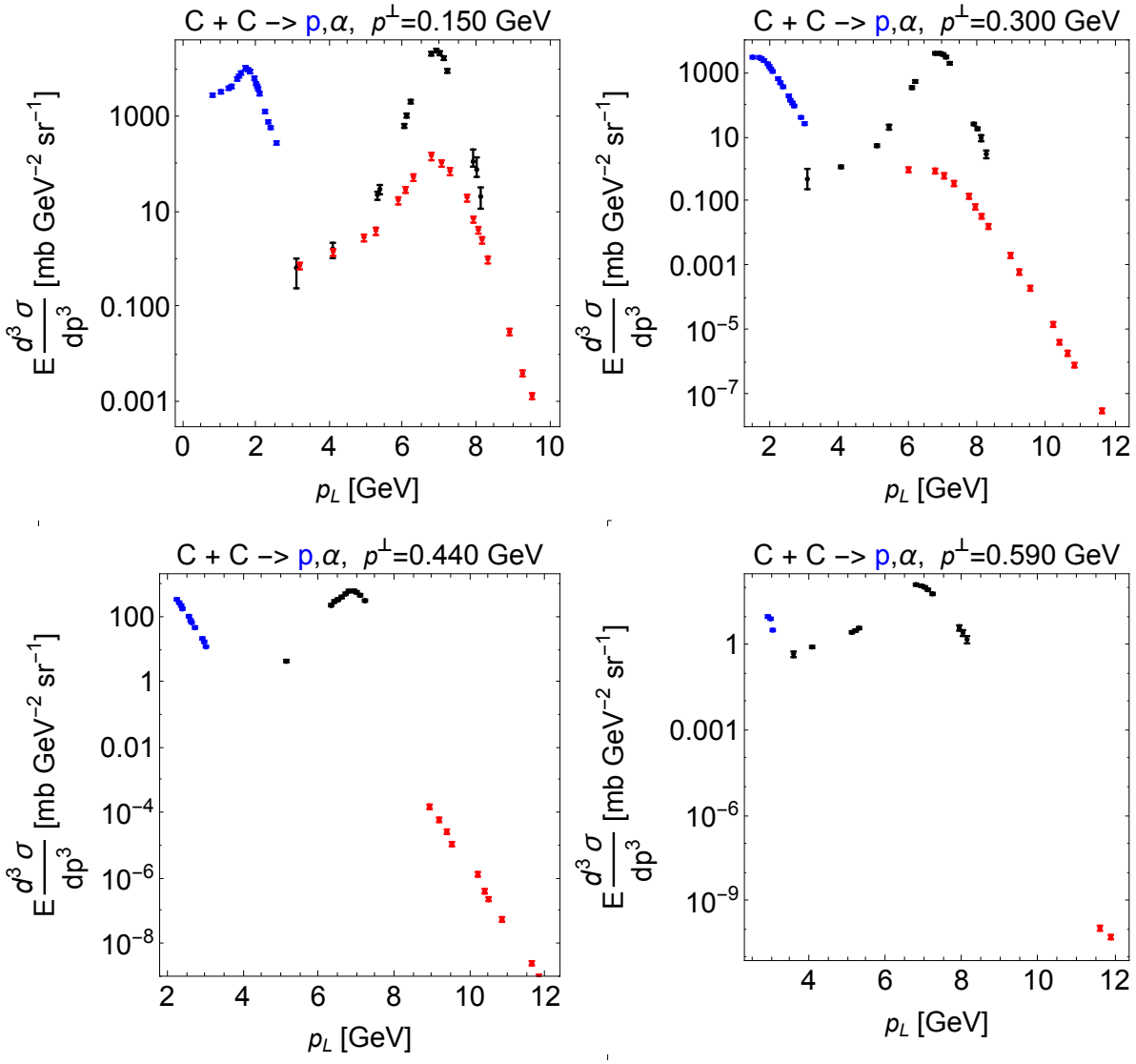

Figure 25: Same as Figure 17, except plot frames are ordered by transverse momentum, $p^{\perp}$, instead of angle.

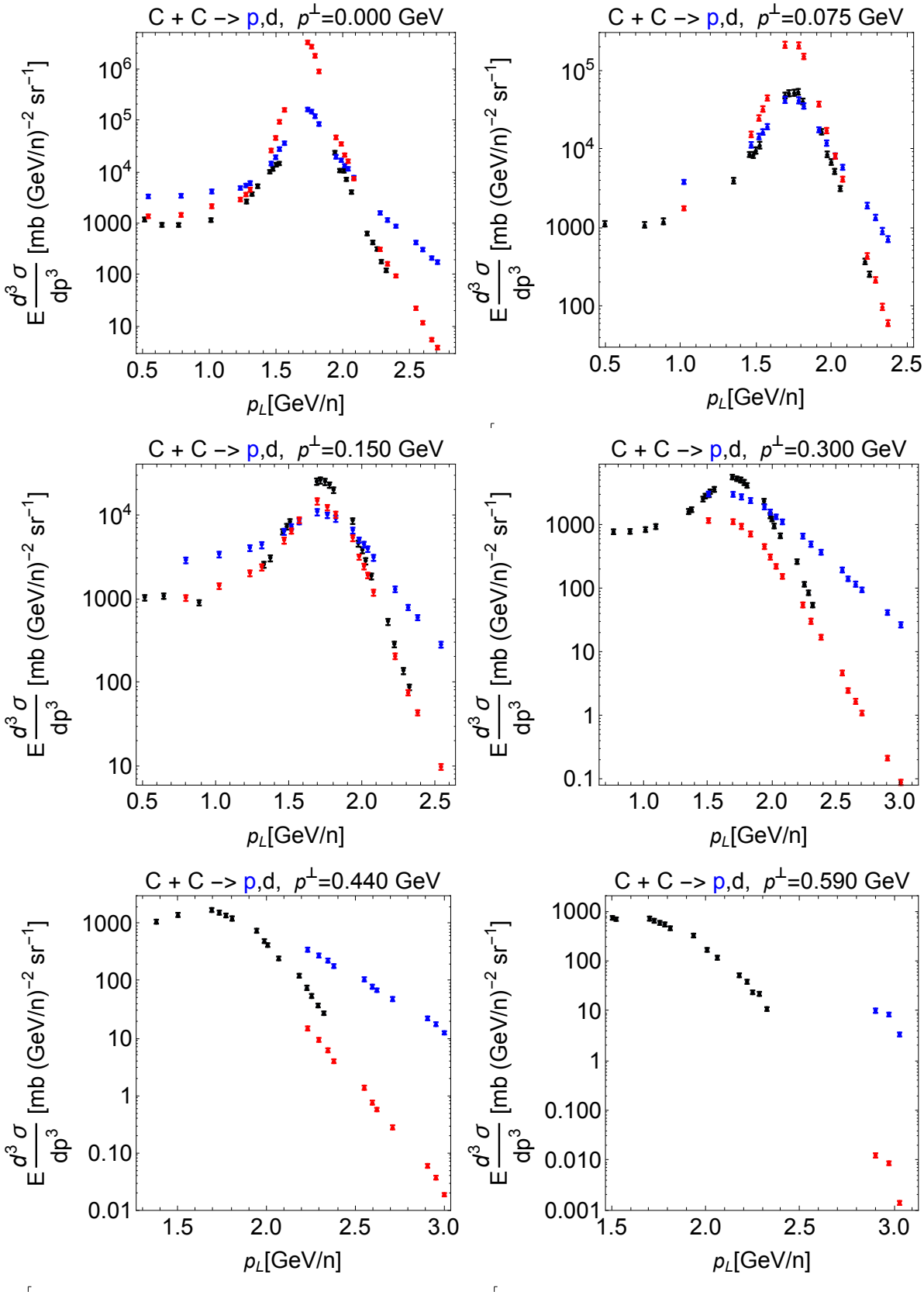

Figure 26: Same as Figure 23, except axes use units of GeV/n.

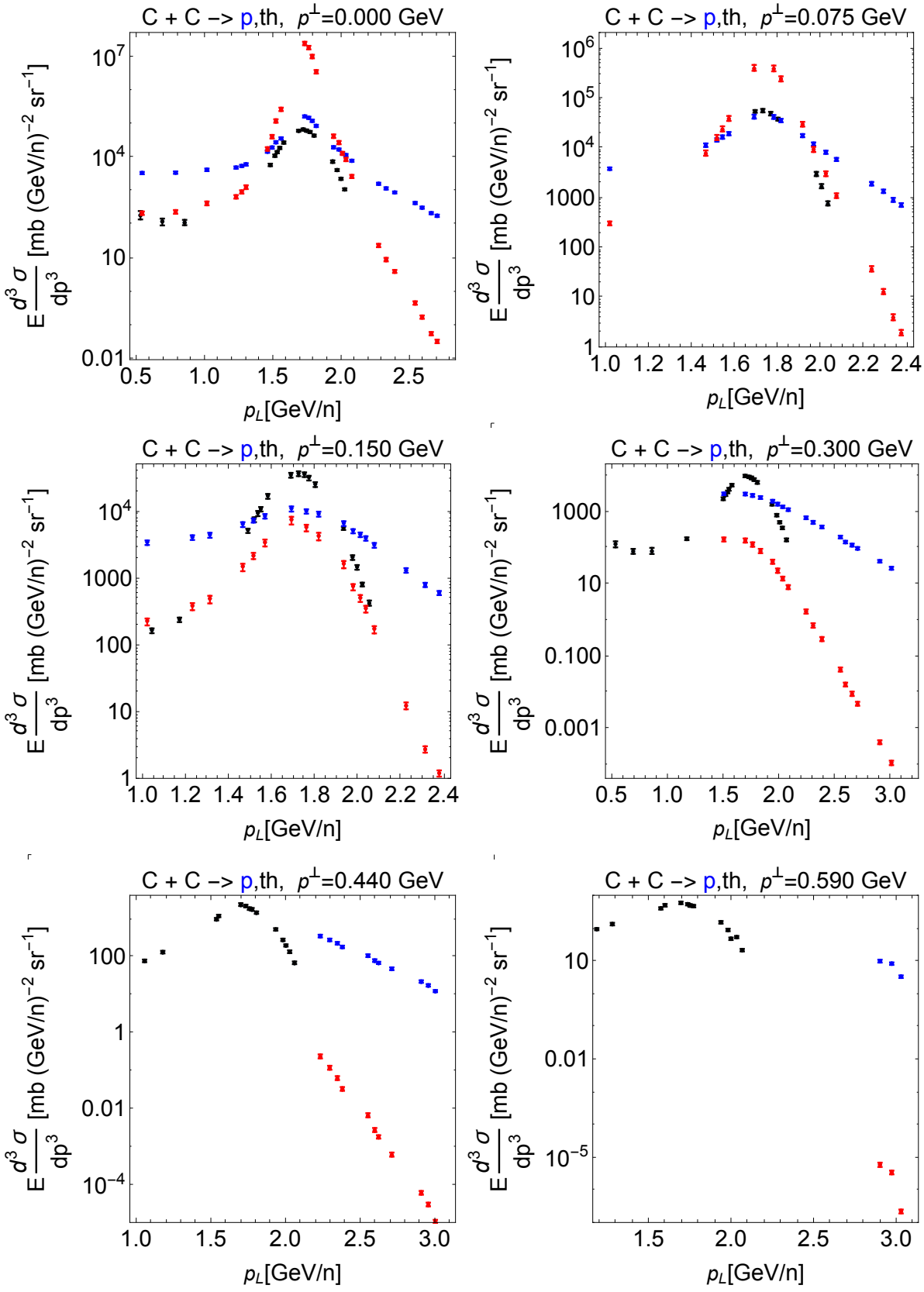

Figure 27: Same as Figure 24, except axes use units of GeV/n.

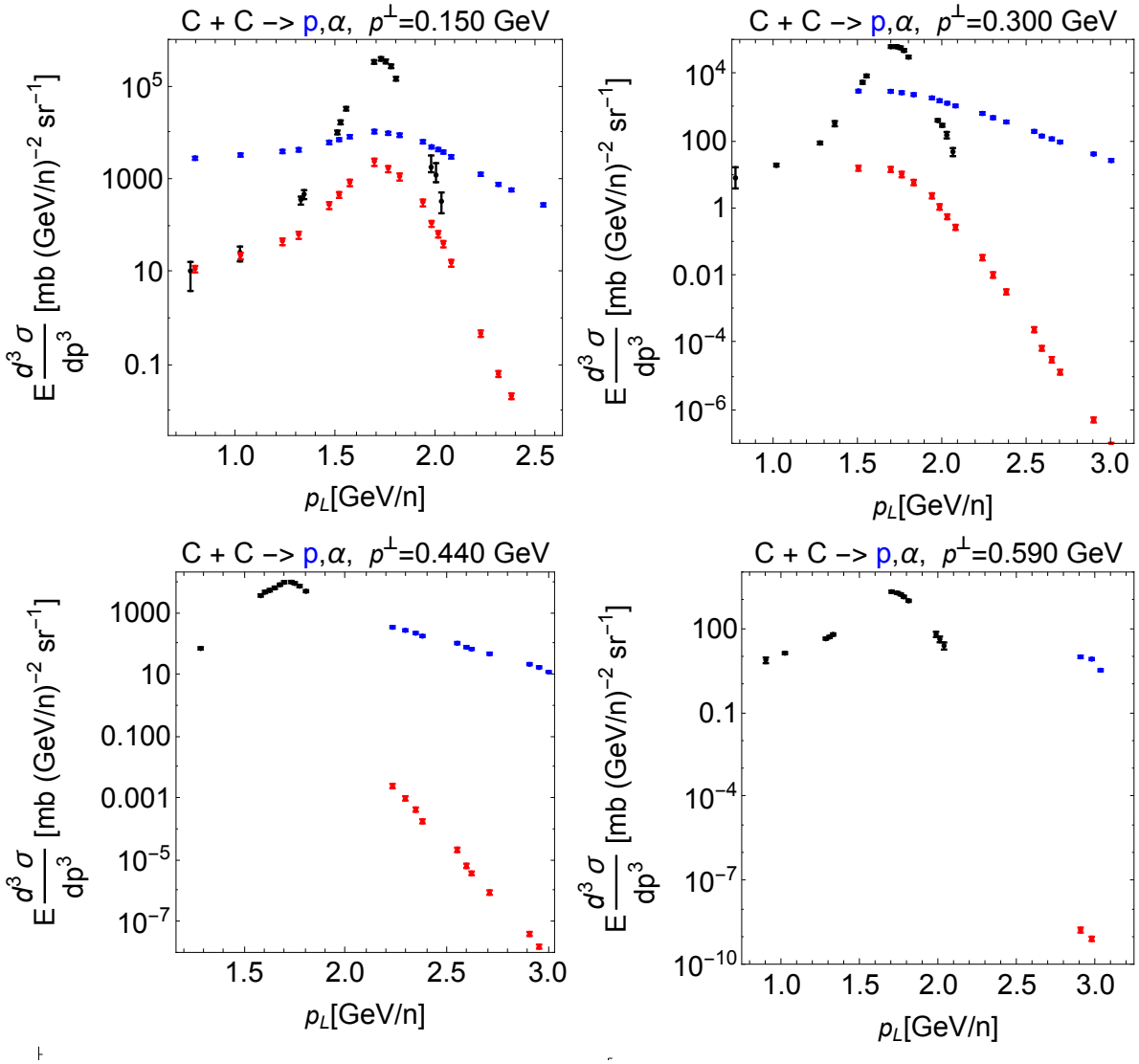

Figure 28: Same as Figure 25, except axes use units of GeV/n.

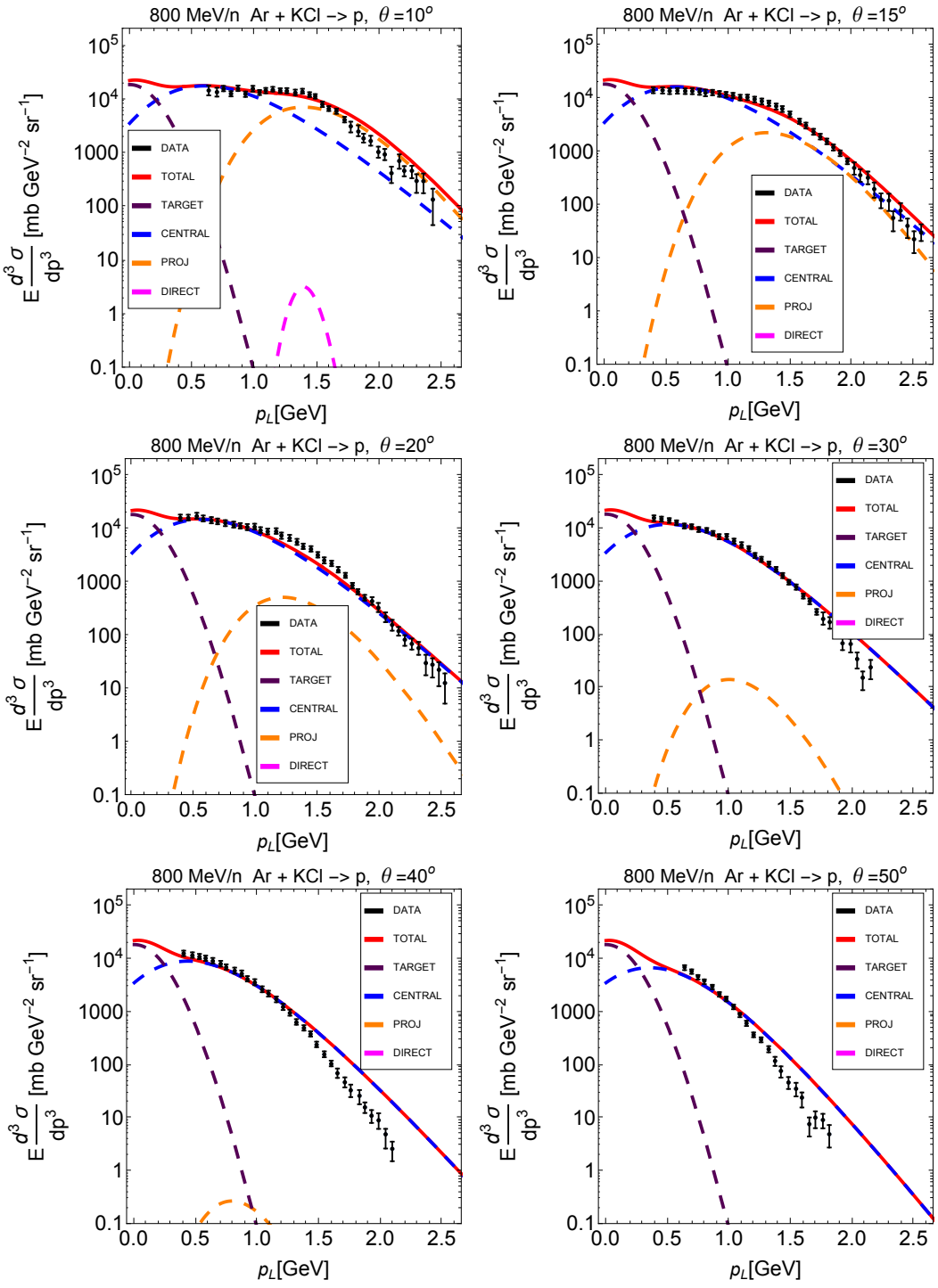

Figure 29: Thermal plus direct knockout model cross-sections for proton production at various angles as a function of lab momentum for Ar + KCl reactions compared to experimental data [13]. Total (red) and individual contributions from central fireball (blue), projectile (orange), direct knockout (magenta), and target (purple) are shown for the parameterized model. Direct knockout does not make any visible contribution for angles > 10°. The individual contributions simply add to give the total, as in equations (13) and (14). Figure is continued on the next page.

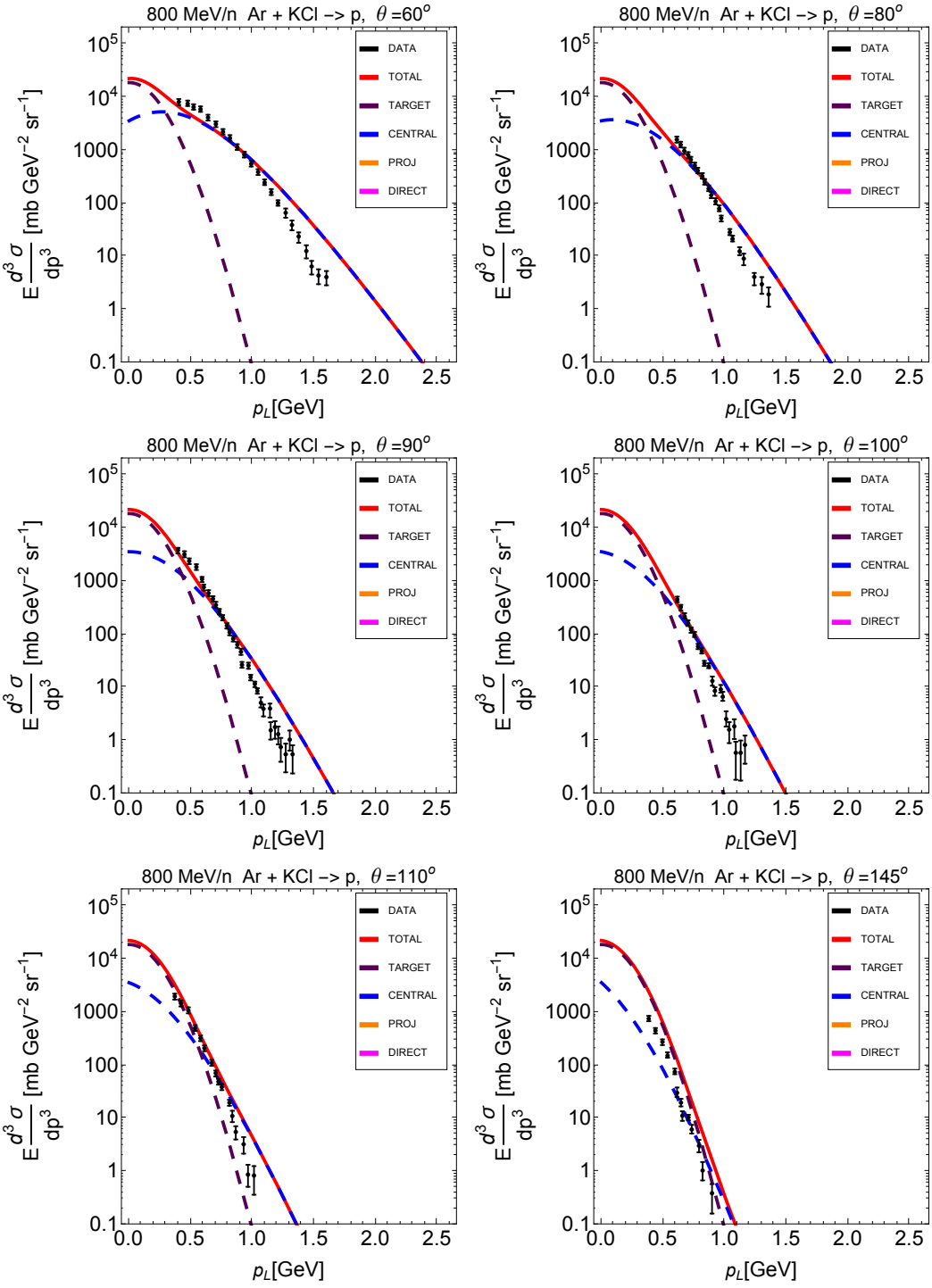

Figure 29 continued.

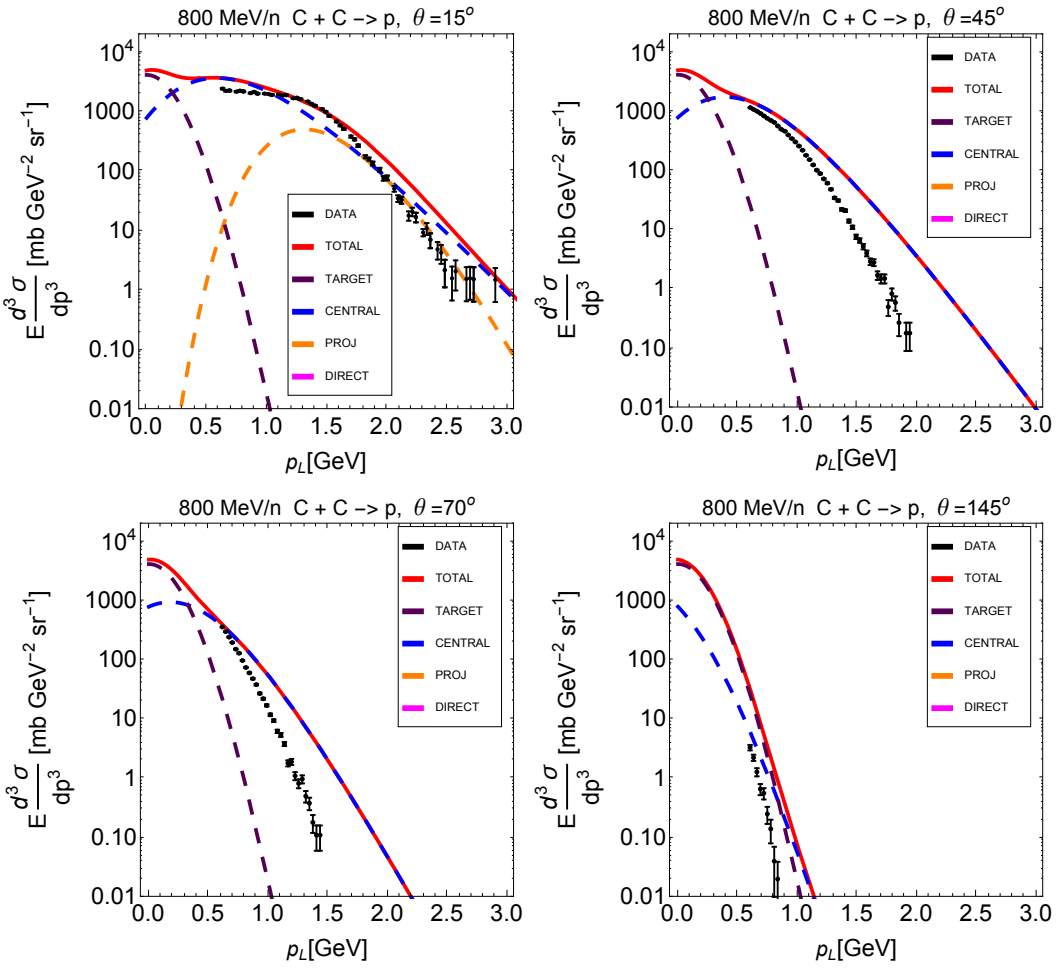

Figure 30: Thermal plus direct knockout model cross-sections for proton production at various angles as a function of lab momentum for C + C reactions compared to experimental data [13]. Individual contribution labeling and addition is the same as Figure 29. Direct knockout does not make any visible contribution for these large angles.

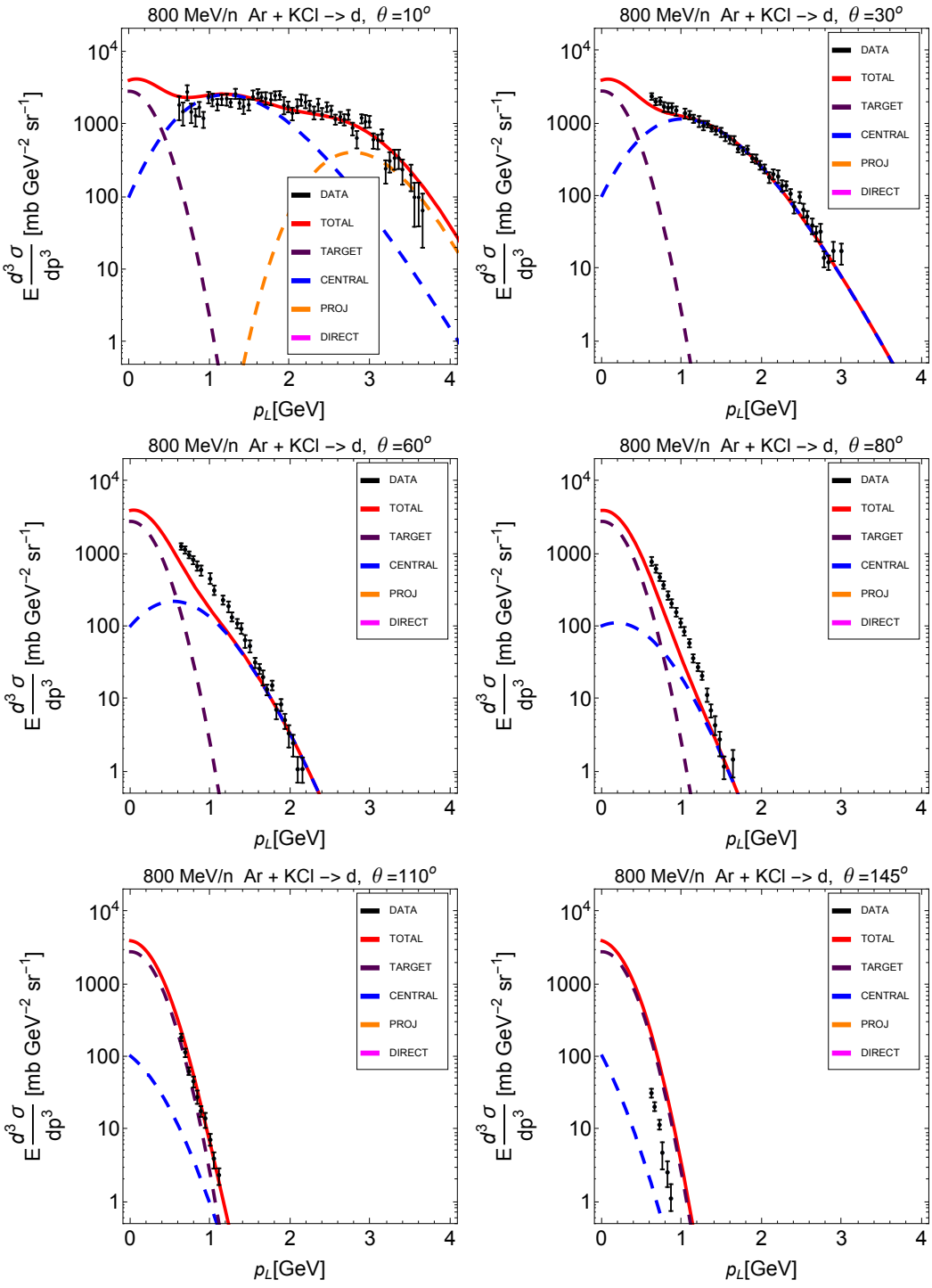

Figure 31: Hybrid coalescence model cross-sections for deuteron production at various angles as a function of lab momentum for Ar + KCl reactions compared to experimental data [13]. Total (red) and individual contributions from central fireball (blue), projectile (orange), direct knockout (magenta), and target (purple) are shown for the parameterized model. Direct knockout does not make any visible contribution for these large angles. Rather than a simple addition, individual contributions add according to equations (17) and (18).

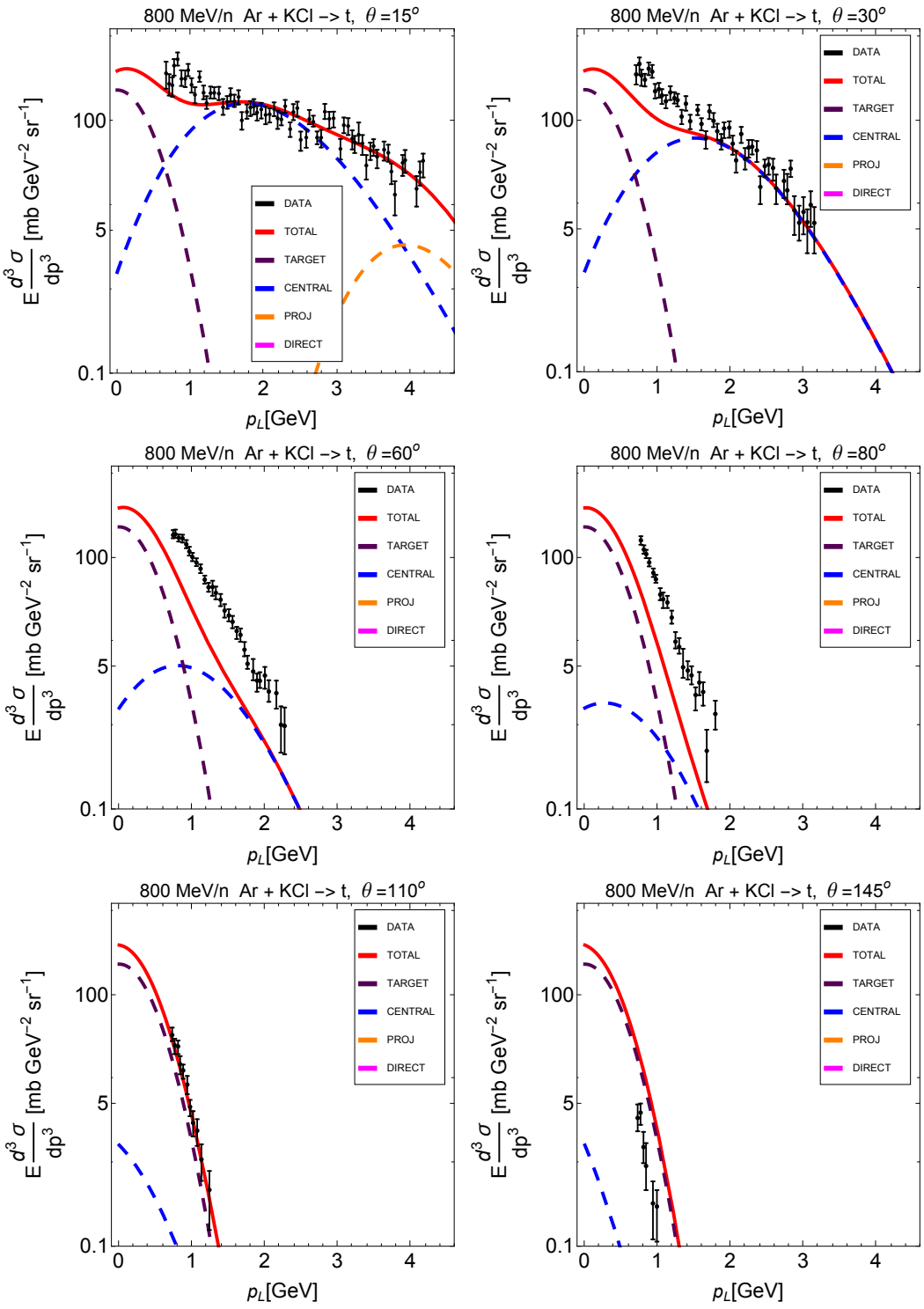

Figure 32: Hybrid coalescence model cross-sections for triton production at various angles as a function of lab momentum for Ar + KCl reactions compared to experimental data [13]. Individual contribution labeling and addition is the same as Figure 31. Direct knockout does not make any visible contribution for these large angles.

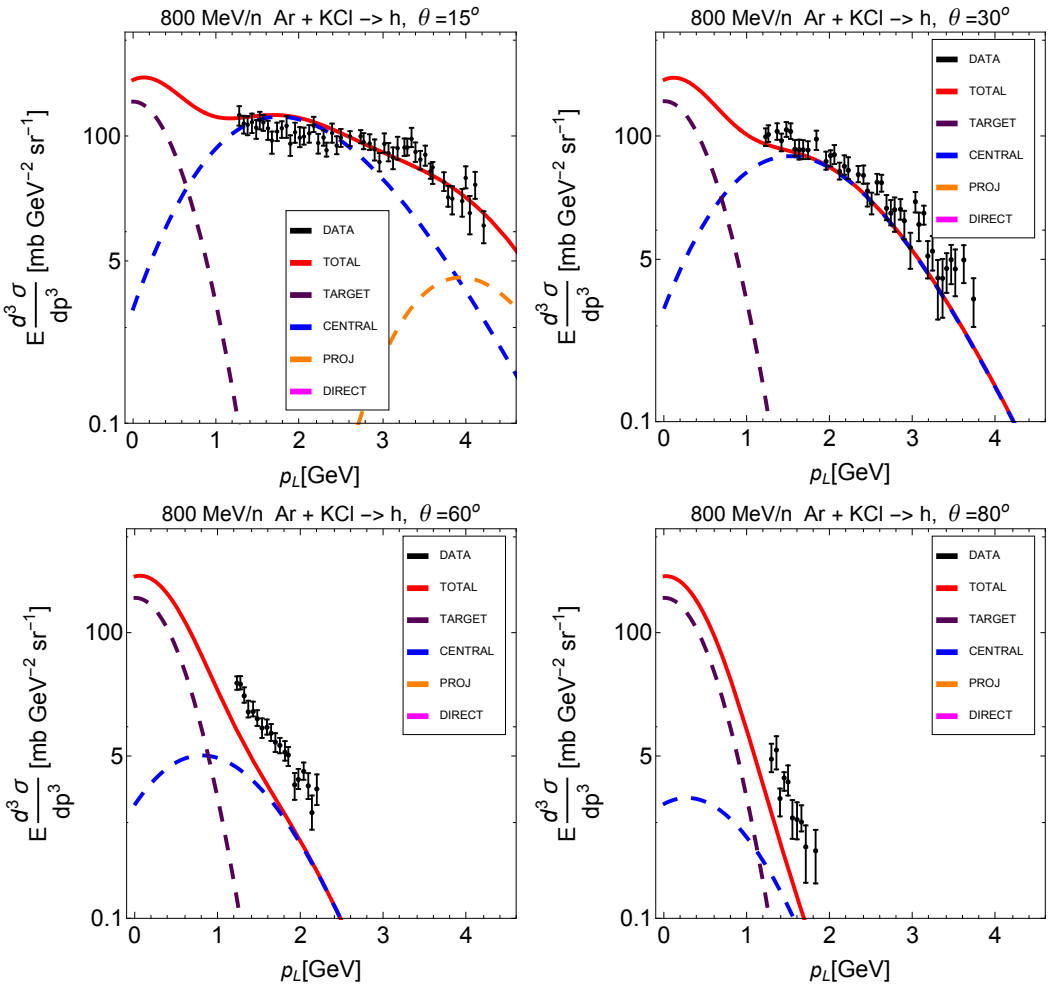

Figure 33: Hybrid coalescence model cross-sections for helion production at various angles as a function of lab momentum for Ar + KCl reactions compared to experimental data [13]. Individual contribution labeling and addition is the same as Figure 31. Direct knockout does not make any visible contribution for these large angles.

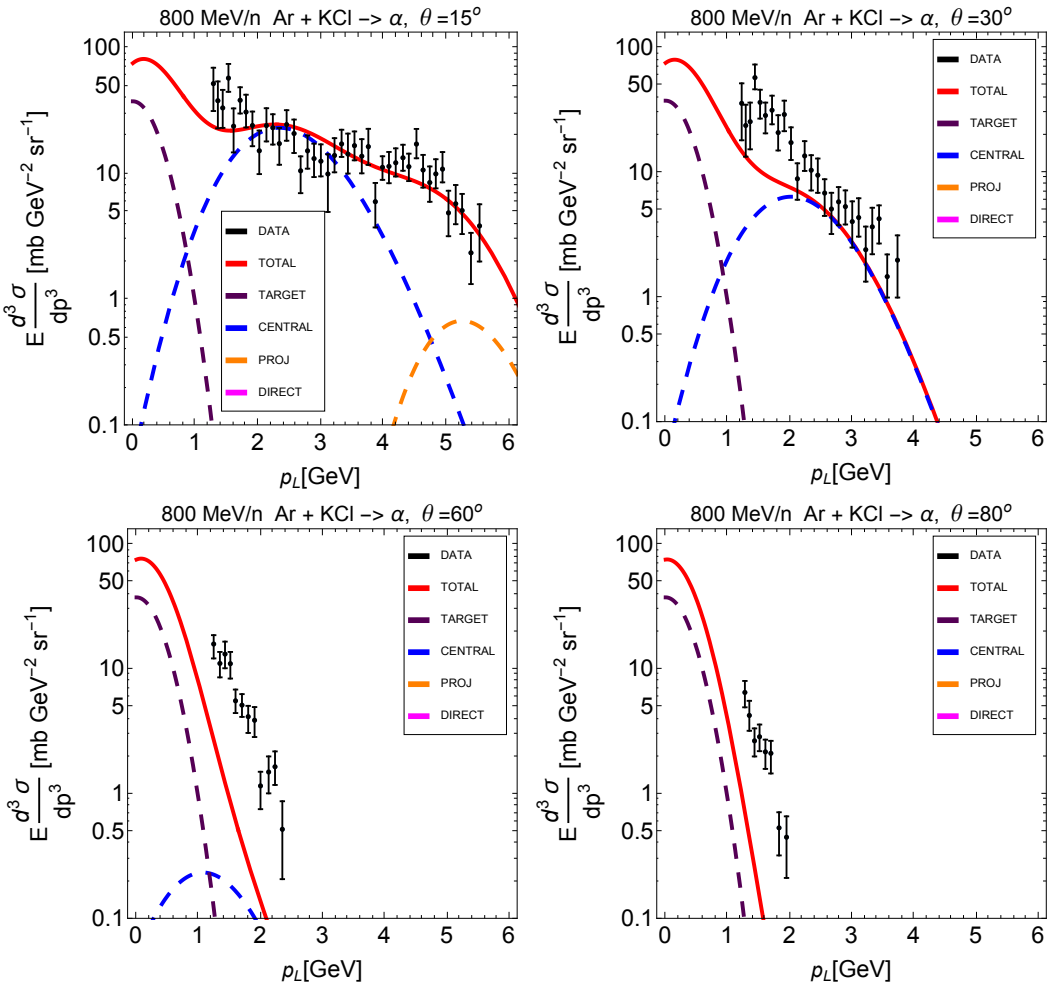

Figure 34: Hybrid coalescence model cross-sections for alpha production at various angles as a function of lab momentum for Ar + KCl reactions compared to experimental data [13]. Individual contribution labeling and addition is the same as Figure 31. Direct knockout does not make any visible contribution for these large angles.

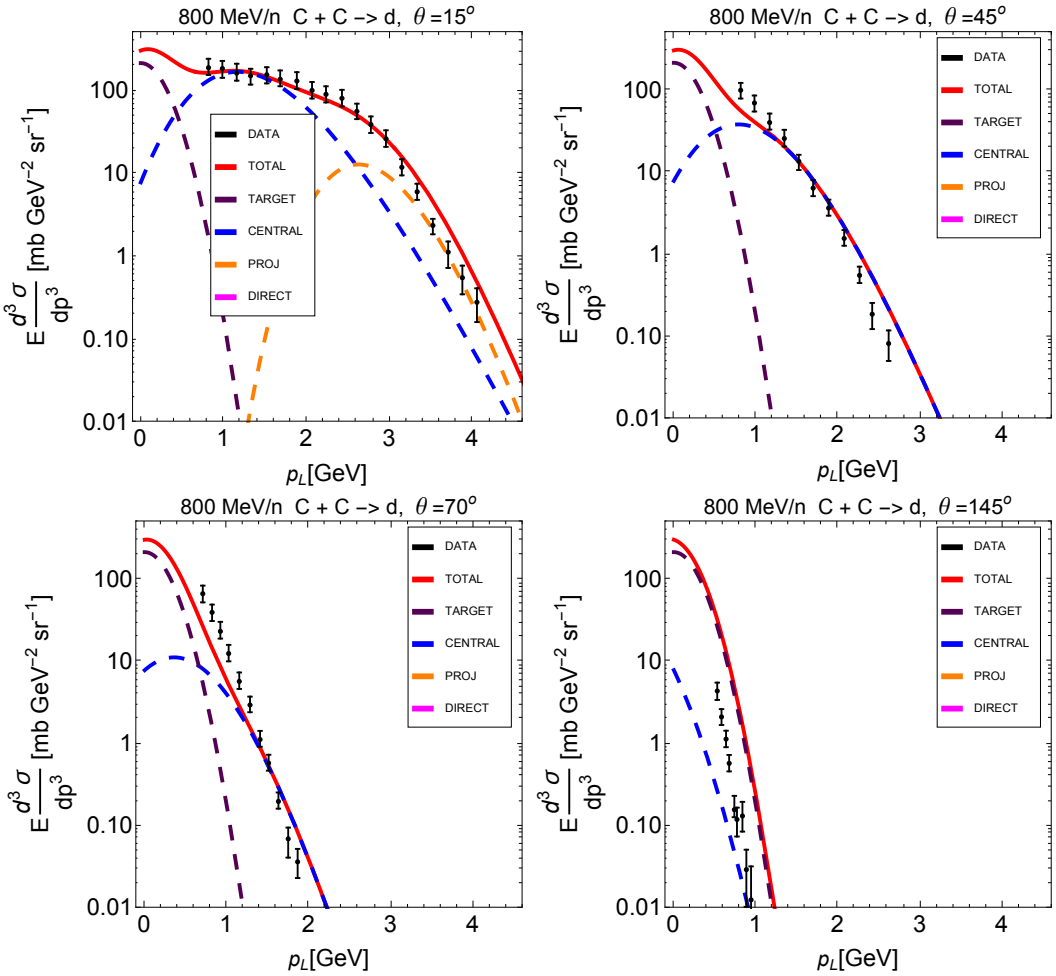

Figure 35: Hybrid coalescence model cross-sections for deuteron production at various angles as a function of lab momentum for C + C reactions compared to experimental data [13]. Individual contribution labeling and addition is the same as Figure 35. Direct knockout does not make any visible contribution for these large angles.

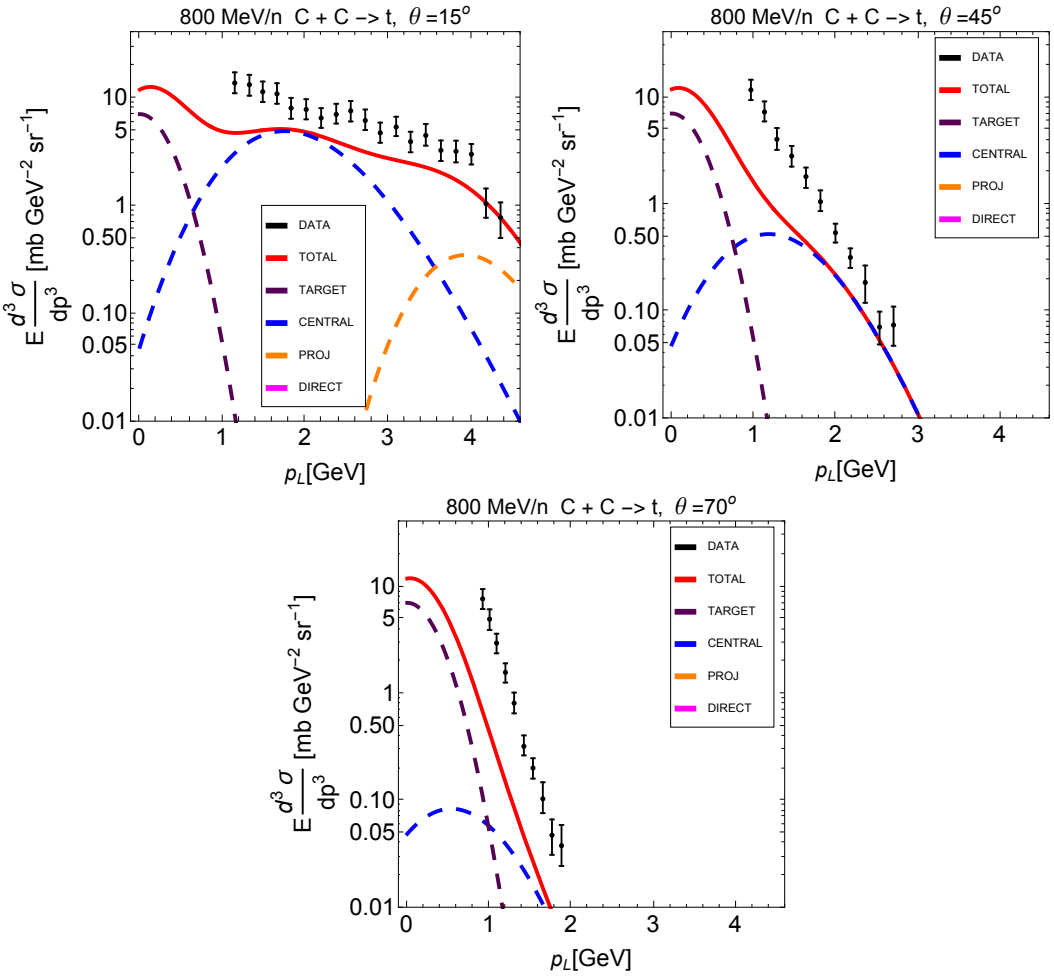

Figure 36: Hybrid coalescence model cross-sections for triton production at various angles as a function of lab momentum for C + C reactions compared to experimental data [13]. Individual contribution labeling and addition is the same as Figure 35. Direct knockout does not make any visible contribution for these large angles.

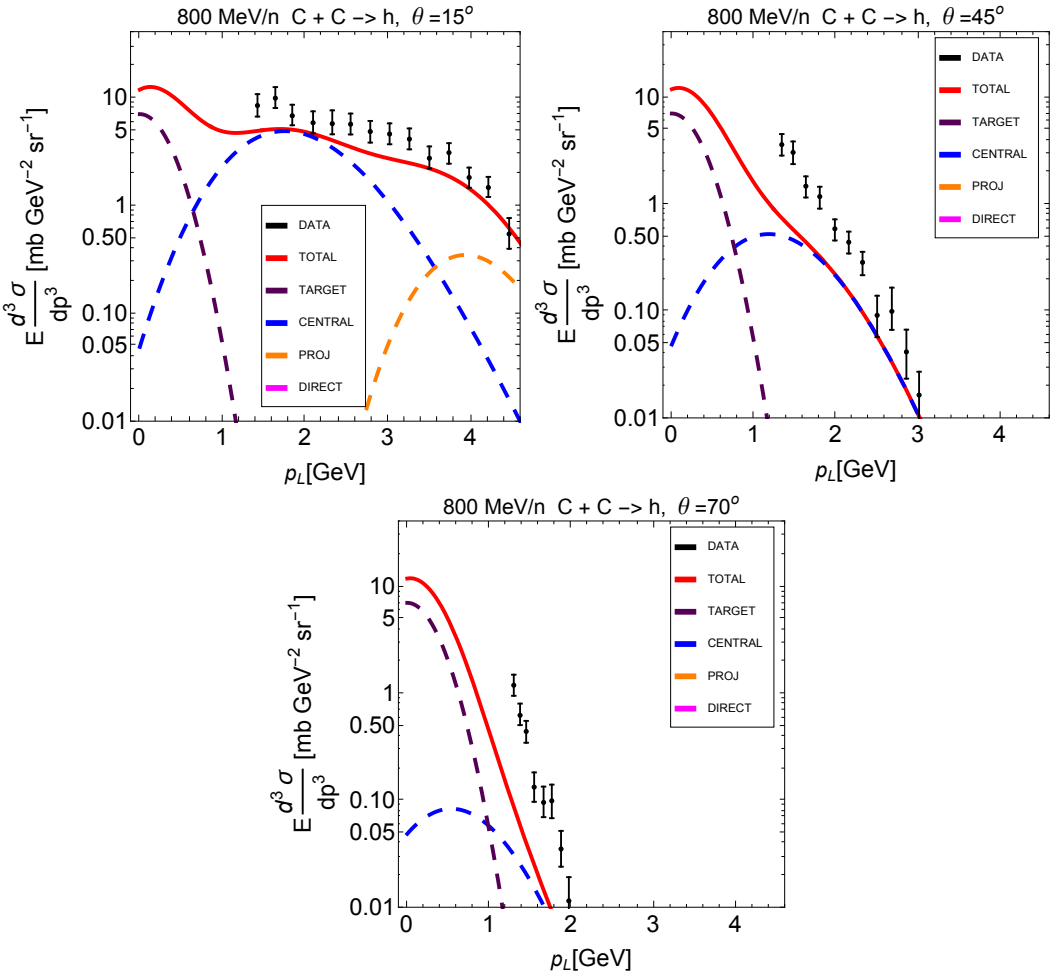

Figure 37: Hybrid coalescence model cross-sections for helion production at various angles as a function of lab momentum for C + C reactions compared to experimental data [13]. Individual contribution labeling and addition is the same as Figure 35. Direct knockout does not make any visible contribution for these large angles.

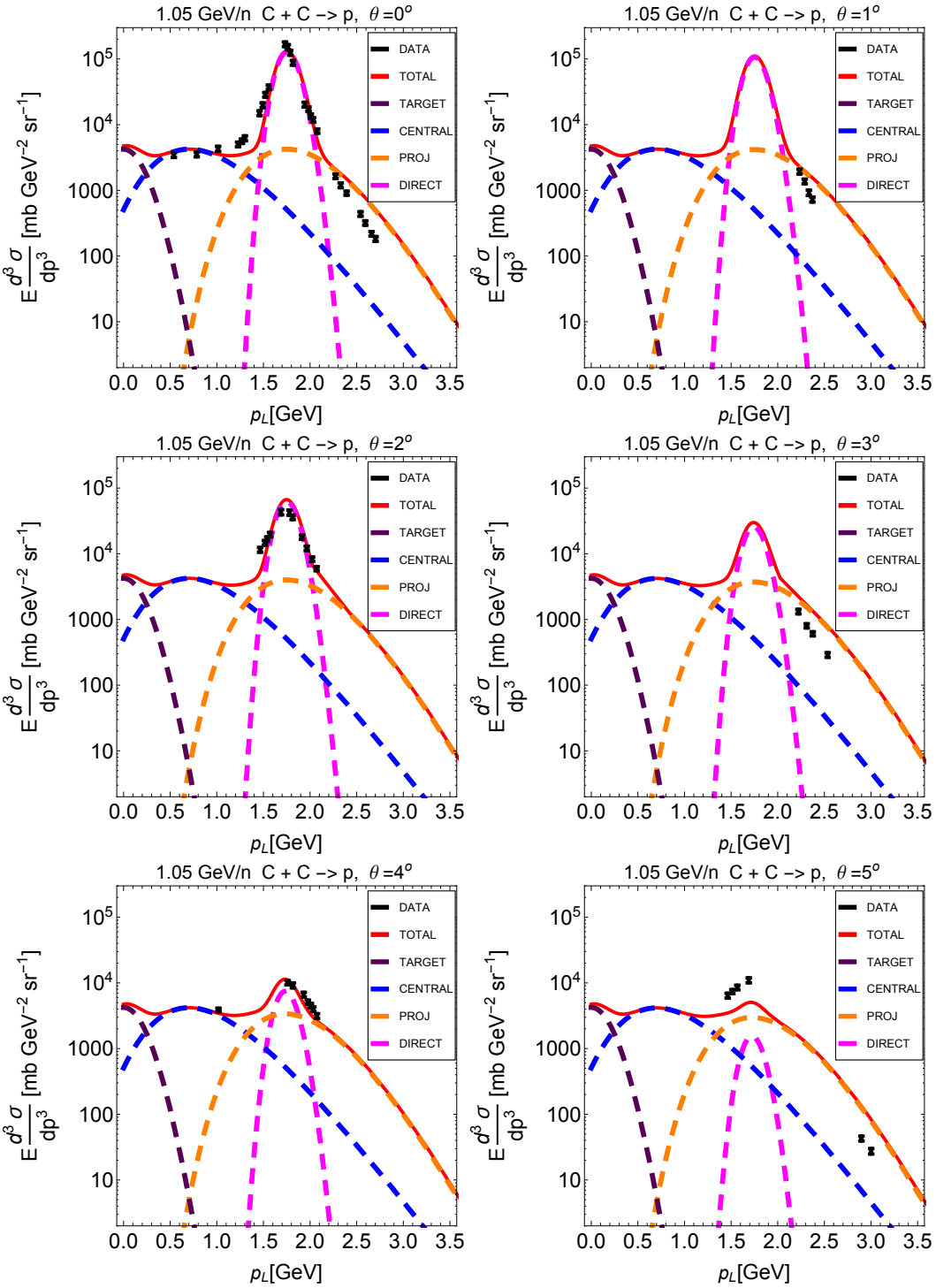

Figure 38: Thermal plus direct knockout model cross-sections for proton production at various angles as a function of lab momentum for C + C reactions compared to experimental data [16]. Individual contribution labeling and addition is the same as Figure 29. Figure is continued on the next page.

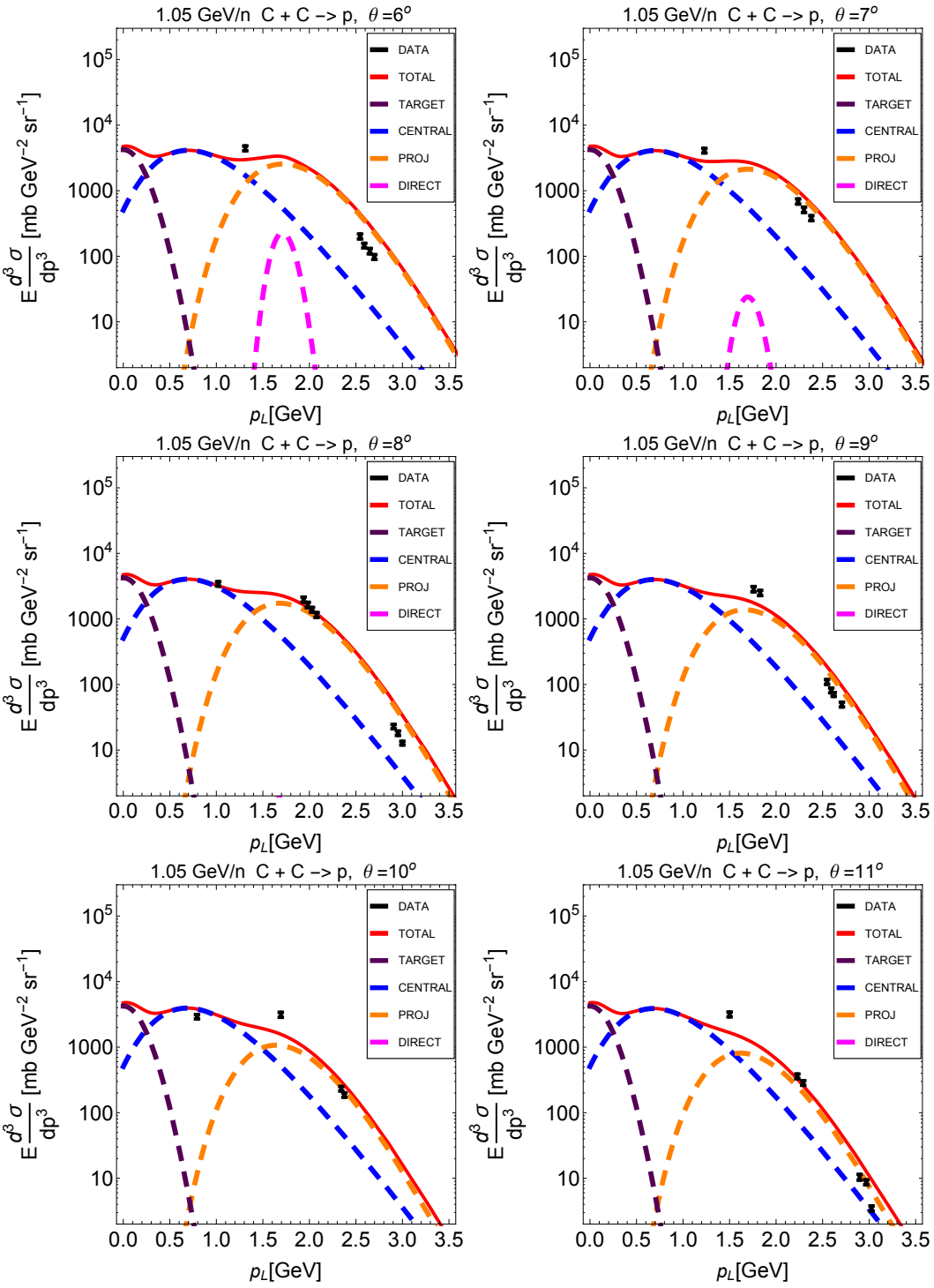

Figure 38 continued.

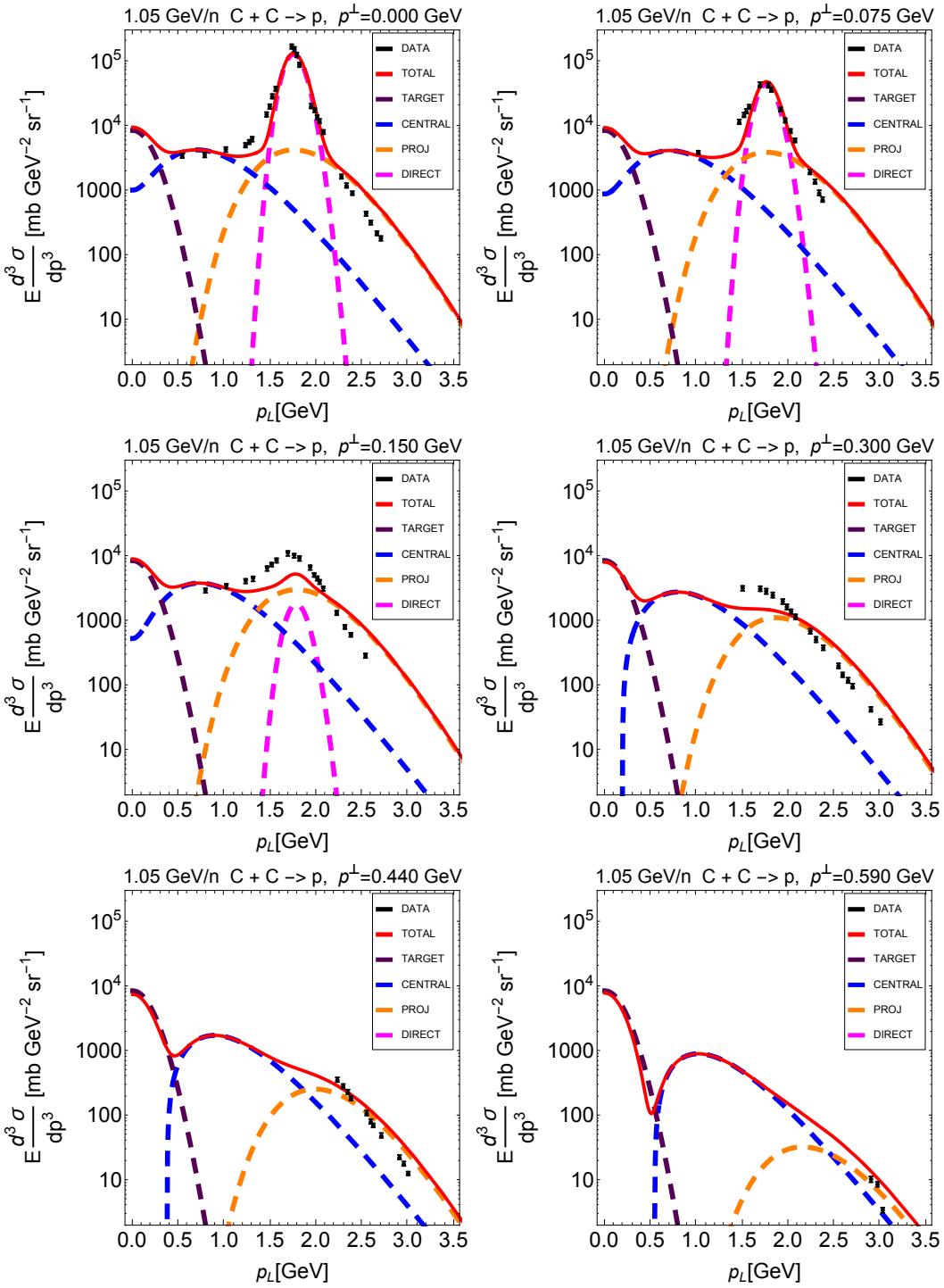

Figure 39: Same as Fig. 38, except that each frame represents a different value of transverse momentum, $p^{\perp}$, rather than angle.

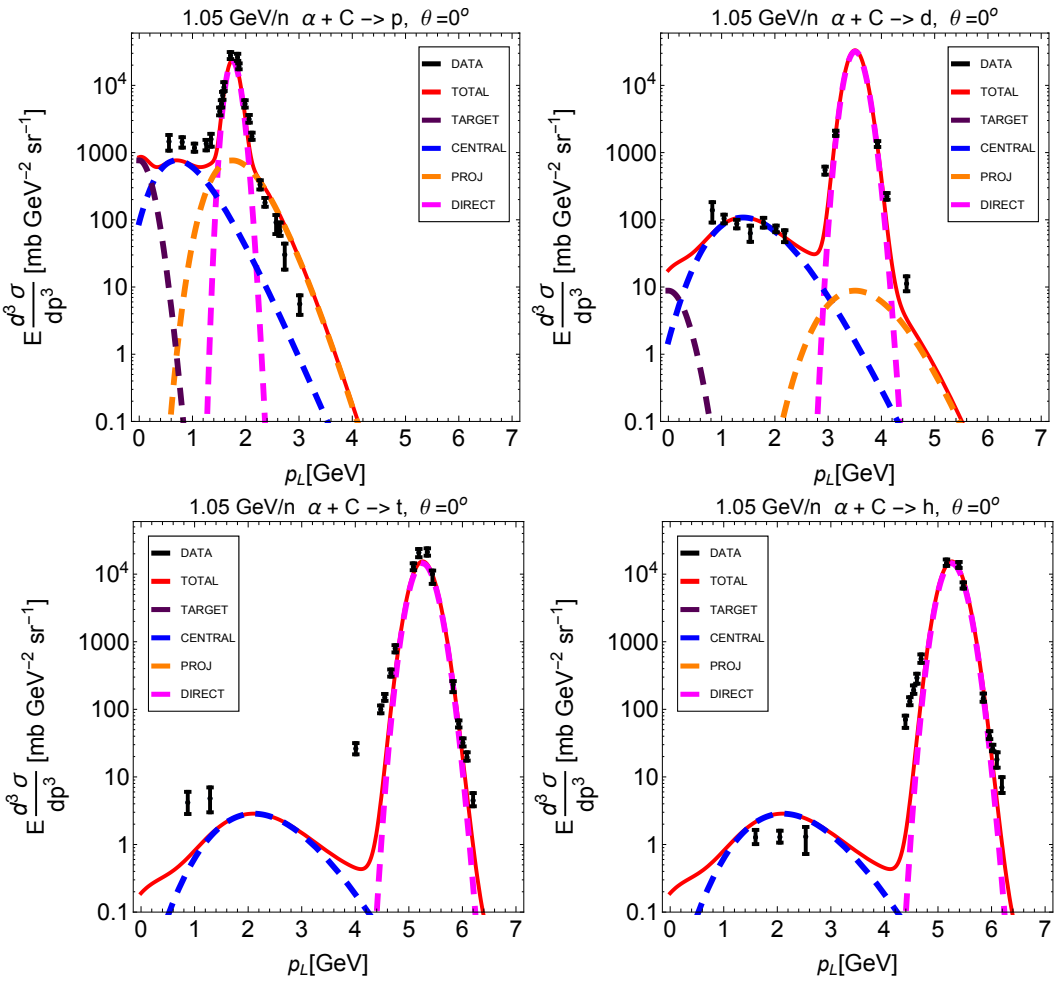

Figure 40: *Top Left:* Thermal plus direct knockout model cross-sections for proton production at an angle of 0° as a function of lab momentum for α + C reactions compared to experimental data [16]. Individual contribution labeling and addition is the same as Figure 29. *Top Right and Bottom:* Hybrid coalescence model cross-sections for deuteron, triton, and helion production at an angle of 0° as a function of lab momentum for C + C reactions compared to experimental data [16]. Individual contribution labeling and addition is the same as Figure 31.

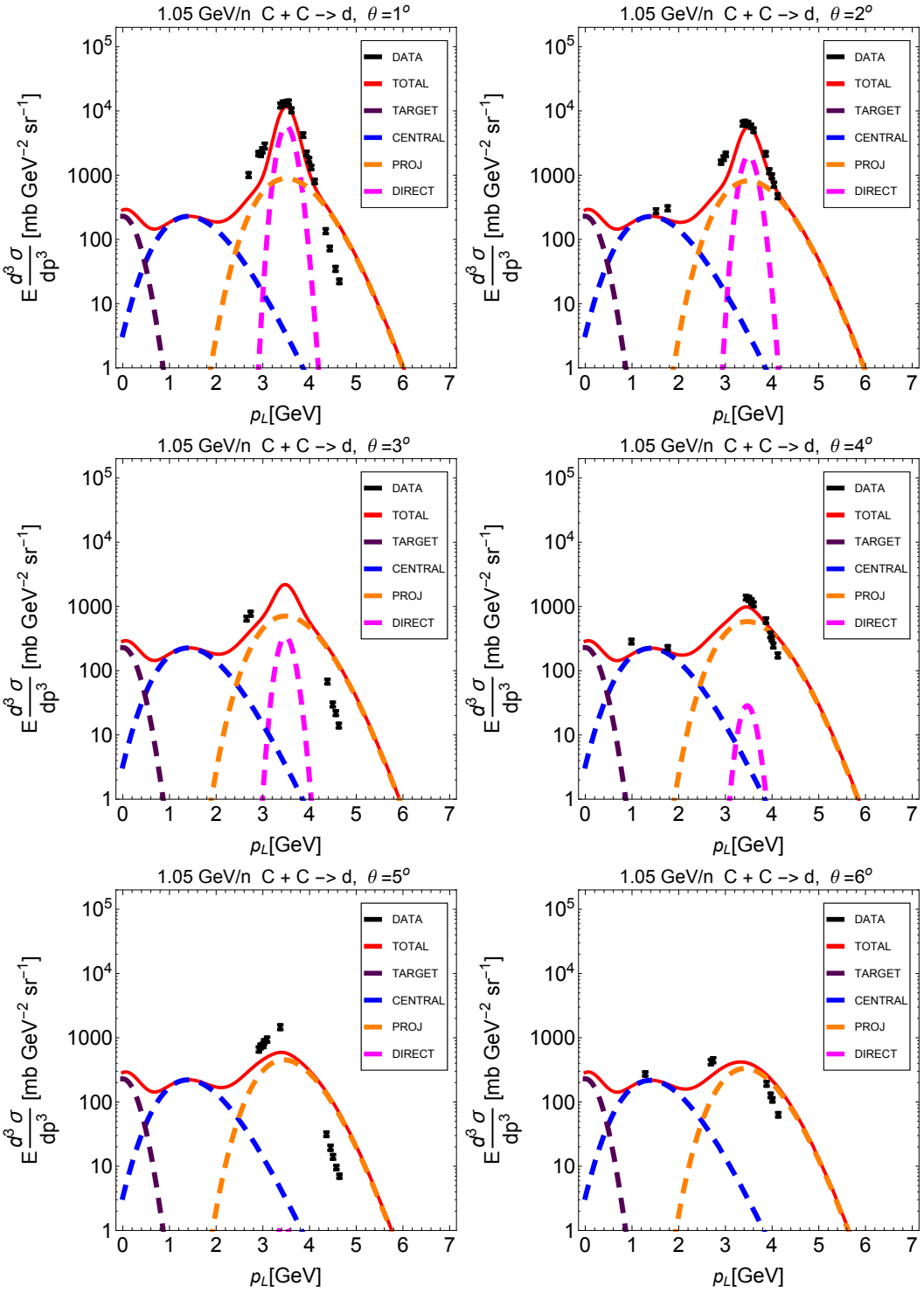

Figure 41: Hybrid coalescence model cross-sections for deuteron production at various angles as a function of lab momentum for C + C reactions compared to experimental data [13]. Individual contribution labeling and addition is the same as Figure 31.

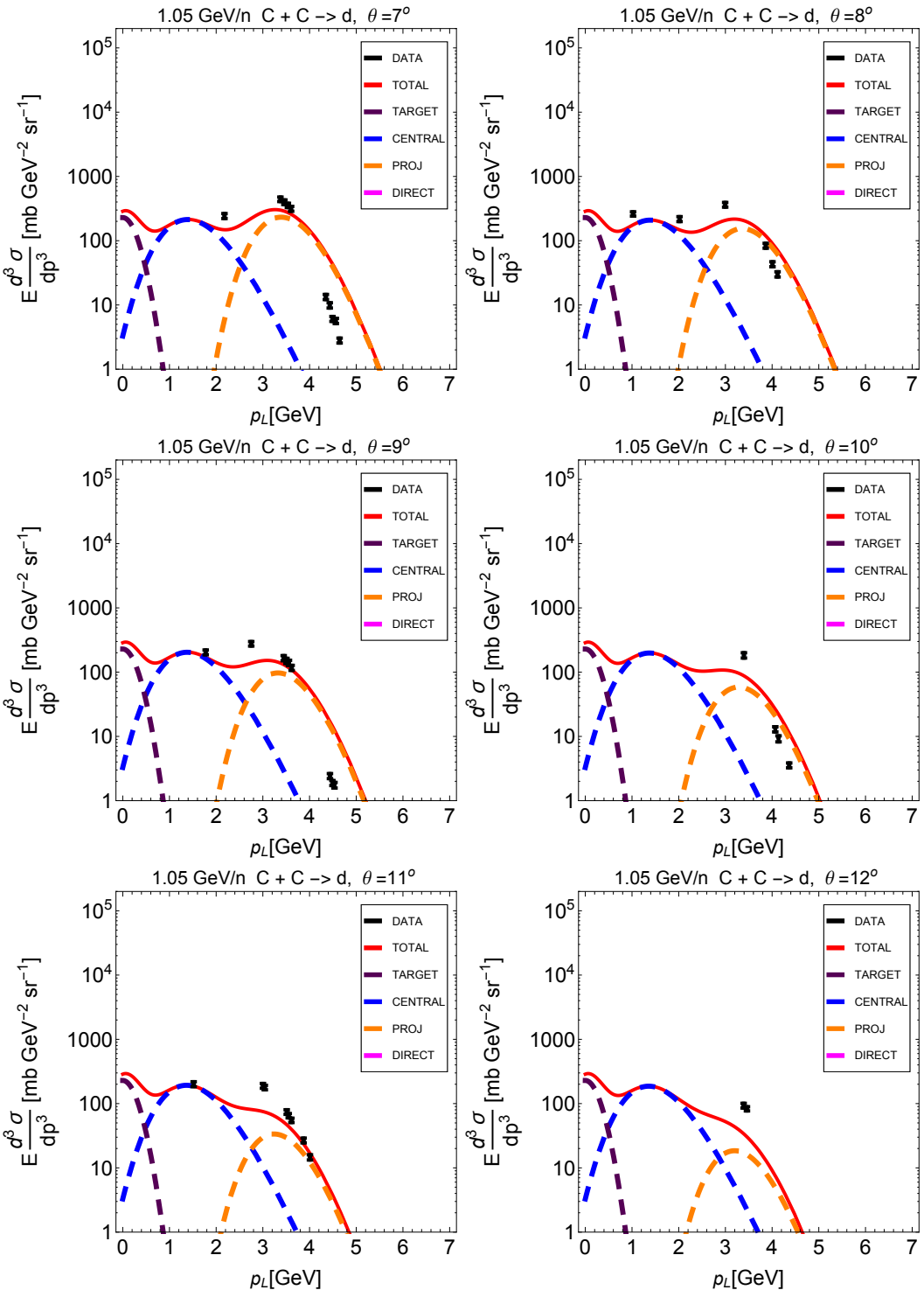

Figure 41 continued.

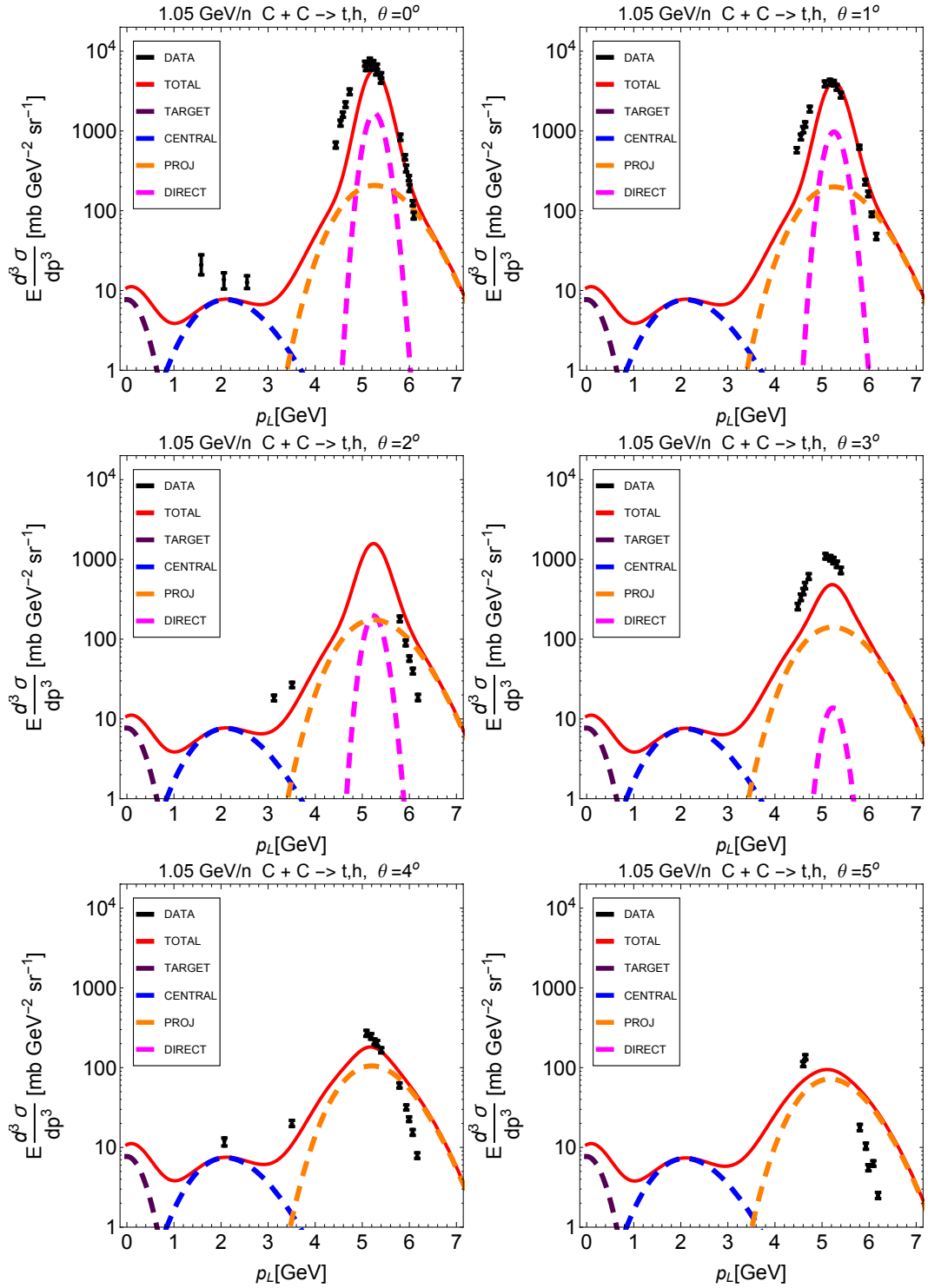

Figure 42: Hybrid coalescence model cross-sections for triton or helion production at various angles as a function of lab momentum for C + C reactions compared to experimental data [13]. Individual contribution labeling and addition is the same as Figure 31.

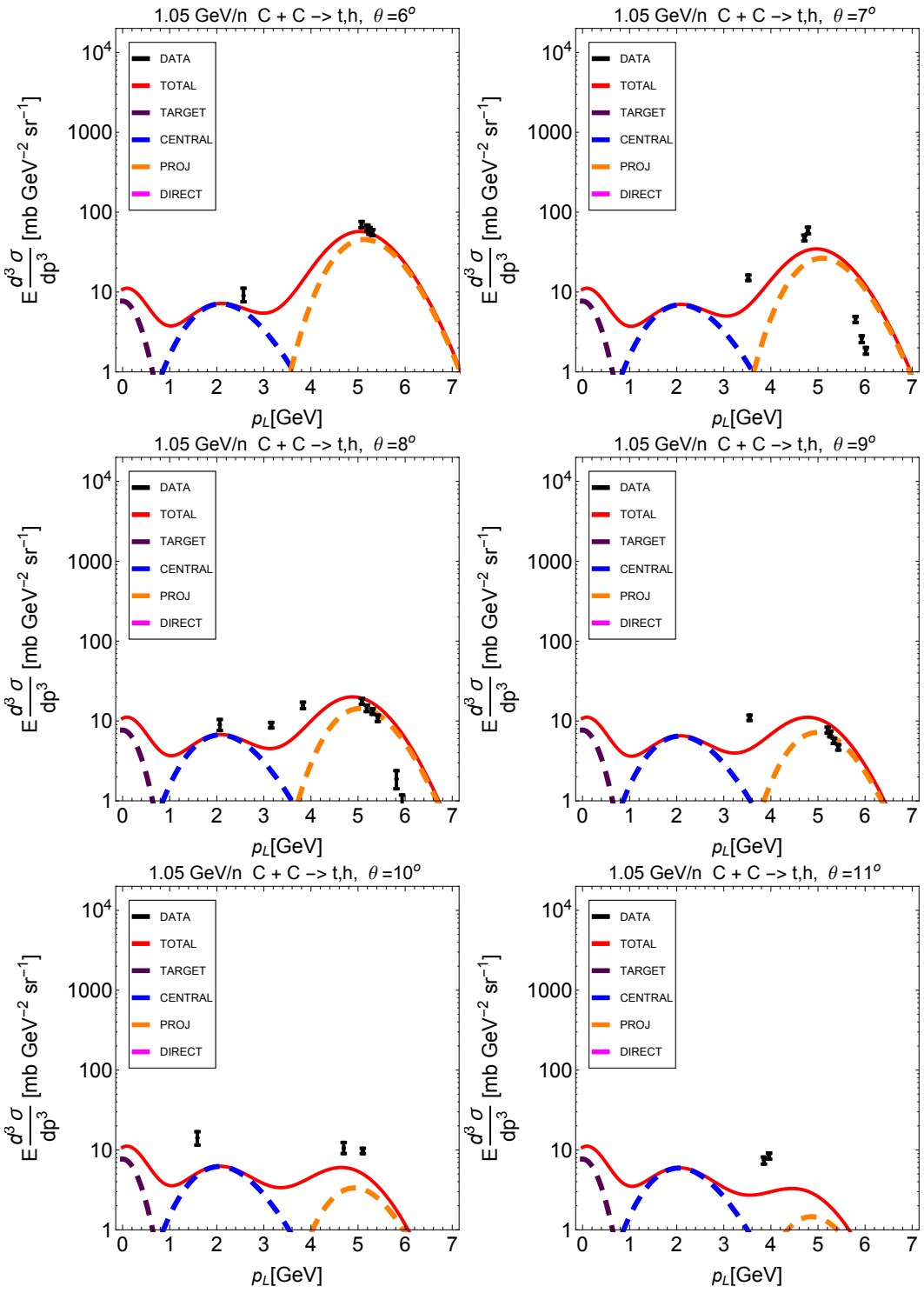

Figure 42 continued.

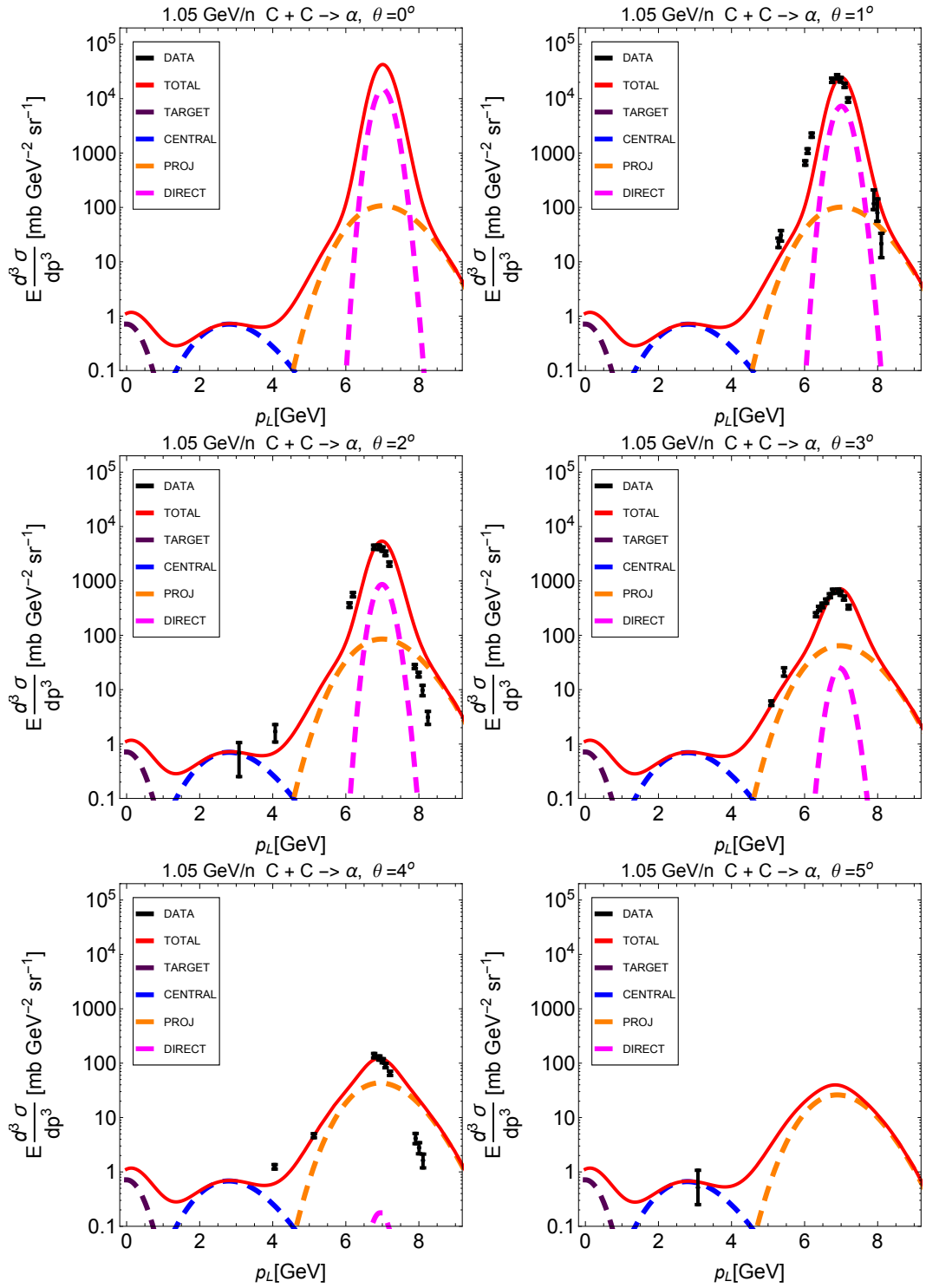

Figure 43: Hybrid coalescence model cross-sections for alpha production at various angles as a function of lab momentum for C + C reactions compared to experimental data [13]. Individual contribution labeling and addition is the same as Figure 31.

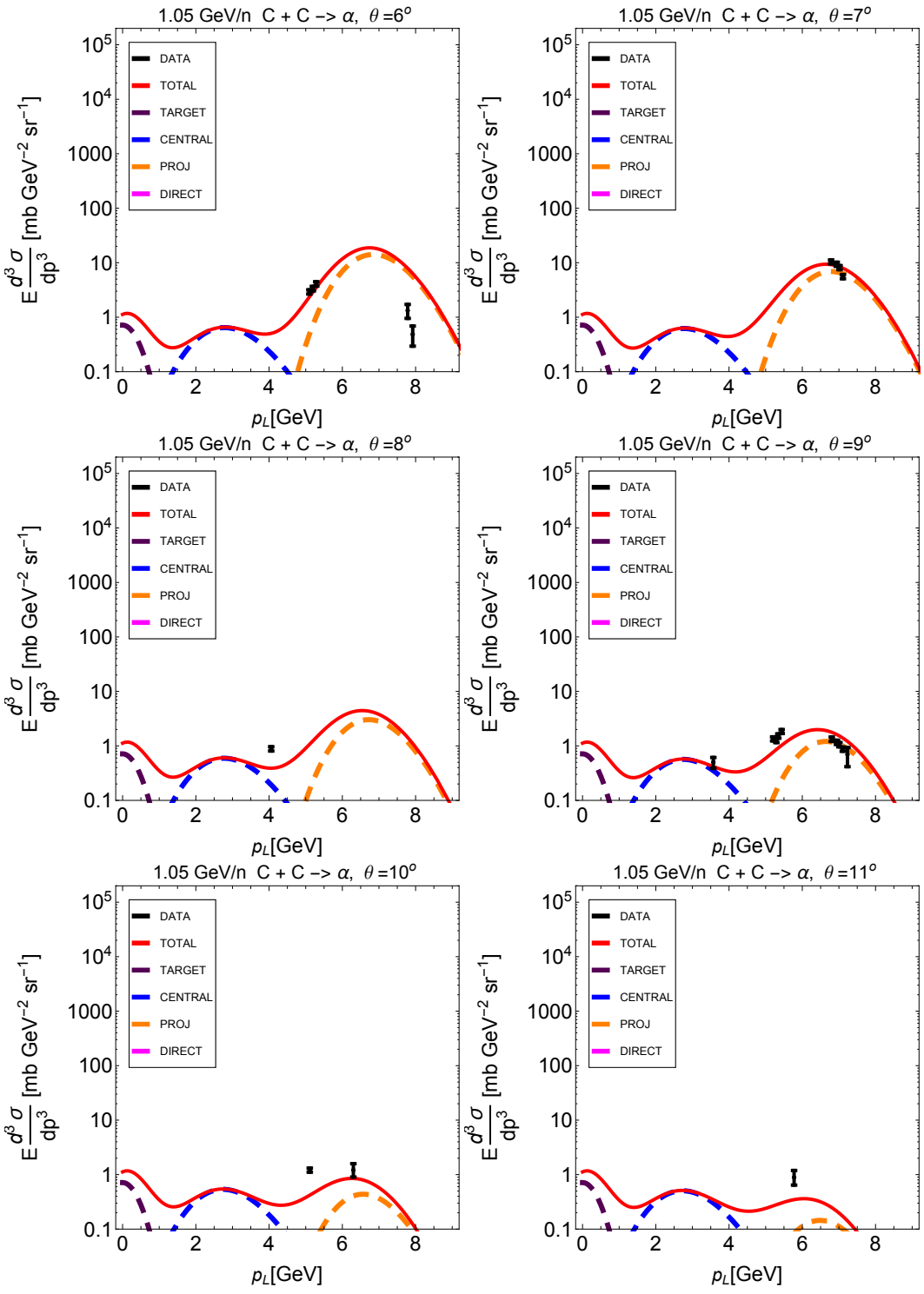

Figure 43 continued.

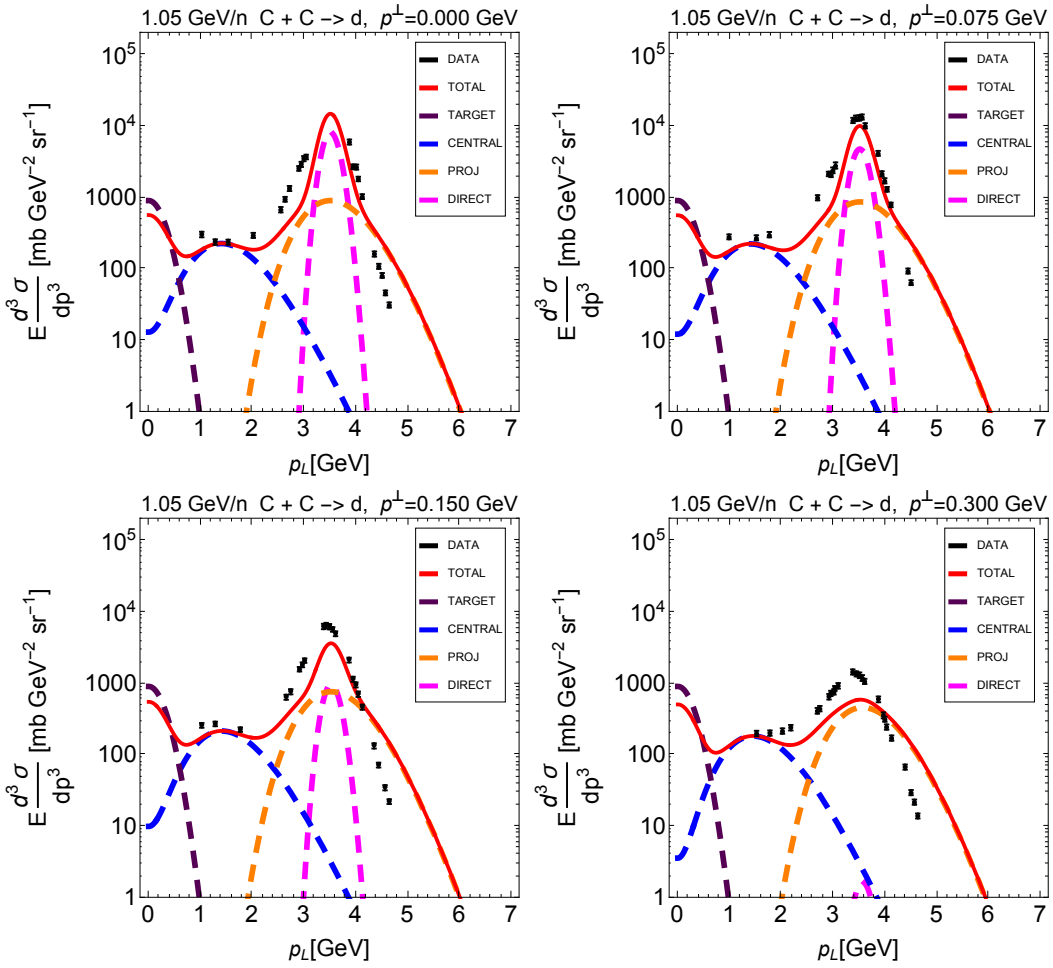

Figure 44: Same as Fig. 41, except that each frame represents a different value of transverse momentum, $p^{\perp}$, rather than angle.

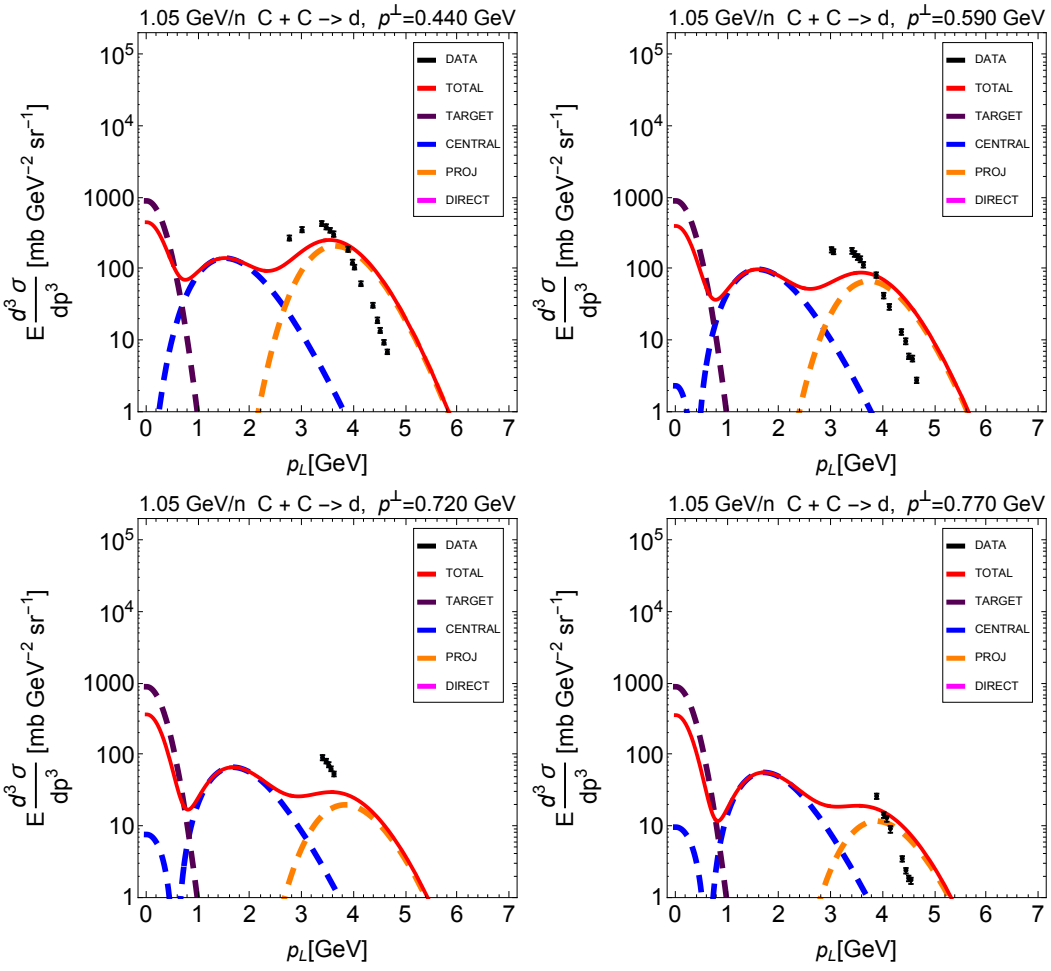

Figure 44 continued.

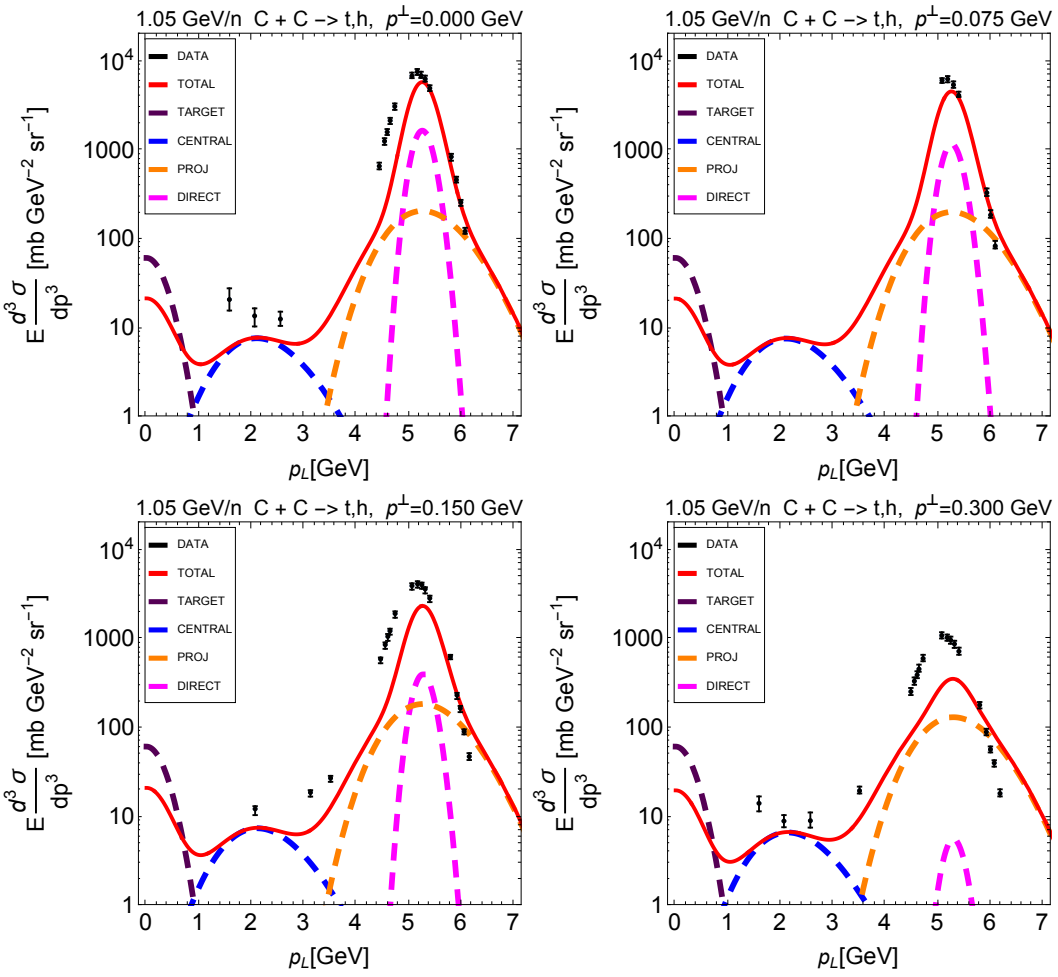

Figure 45: Same as Fig. 42, except that each frame represents a different value of transverse momentum, $p^{\perp}$, rather than angle.

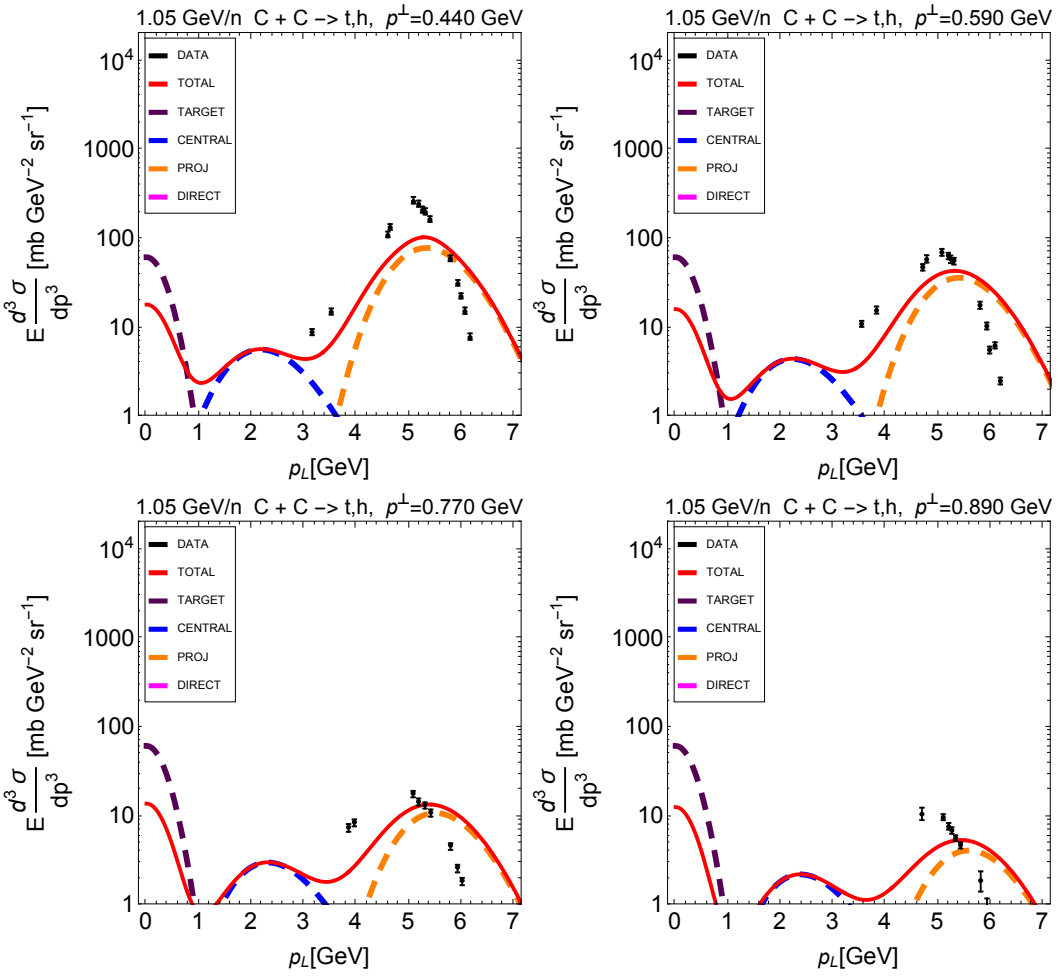

Figure 45 continued.

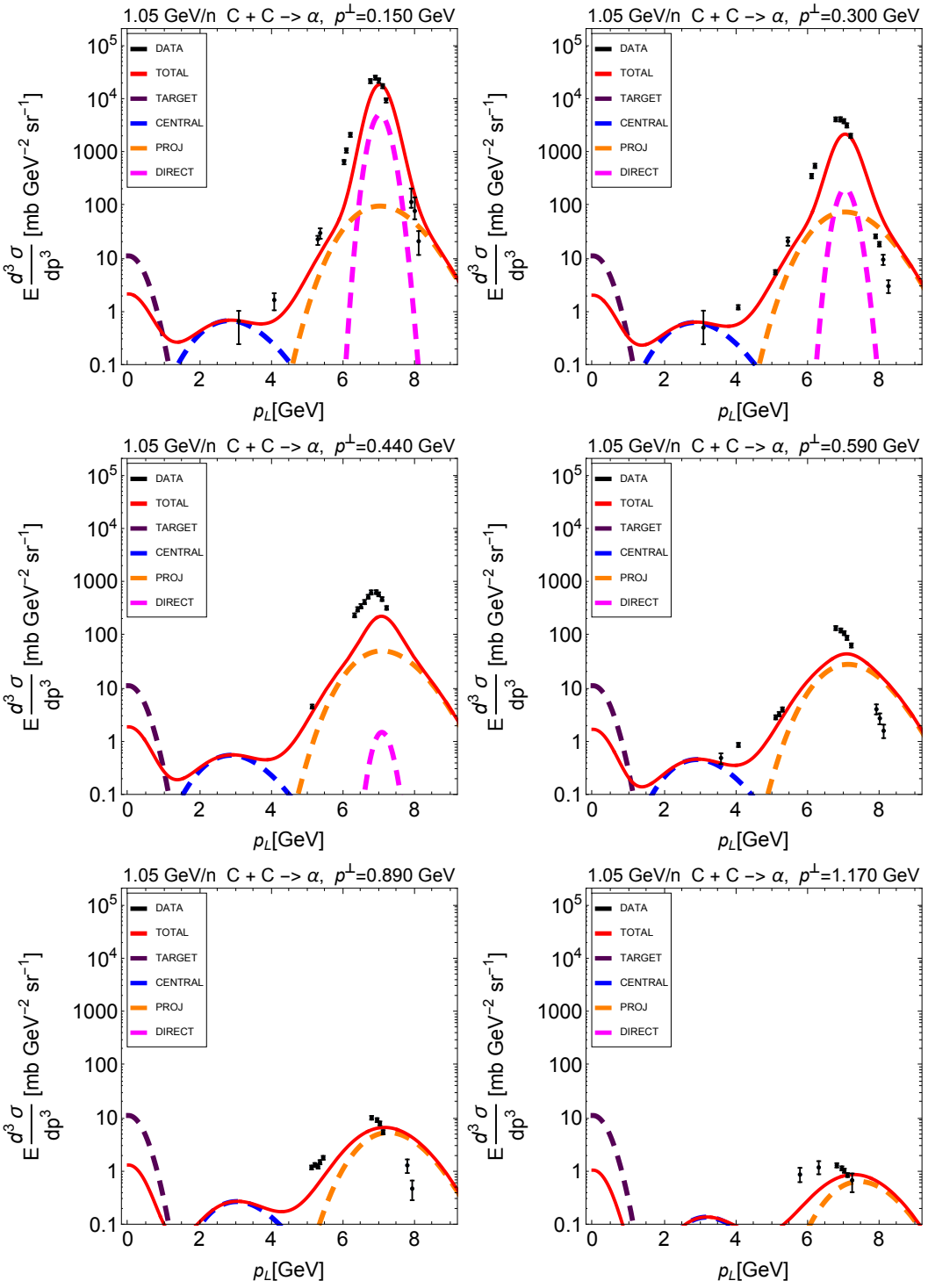

Figure 46: Same as Fig. 43, except that each frame represents a different value of transverse momentum, $p^{\perp}$, rather than angle.

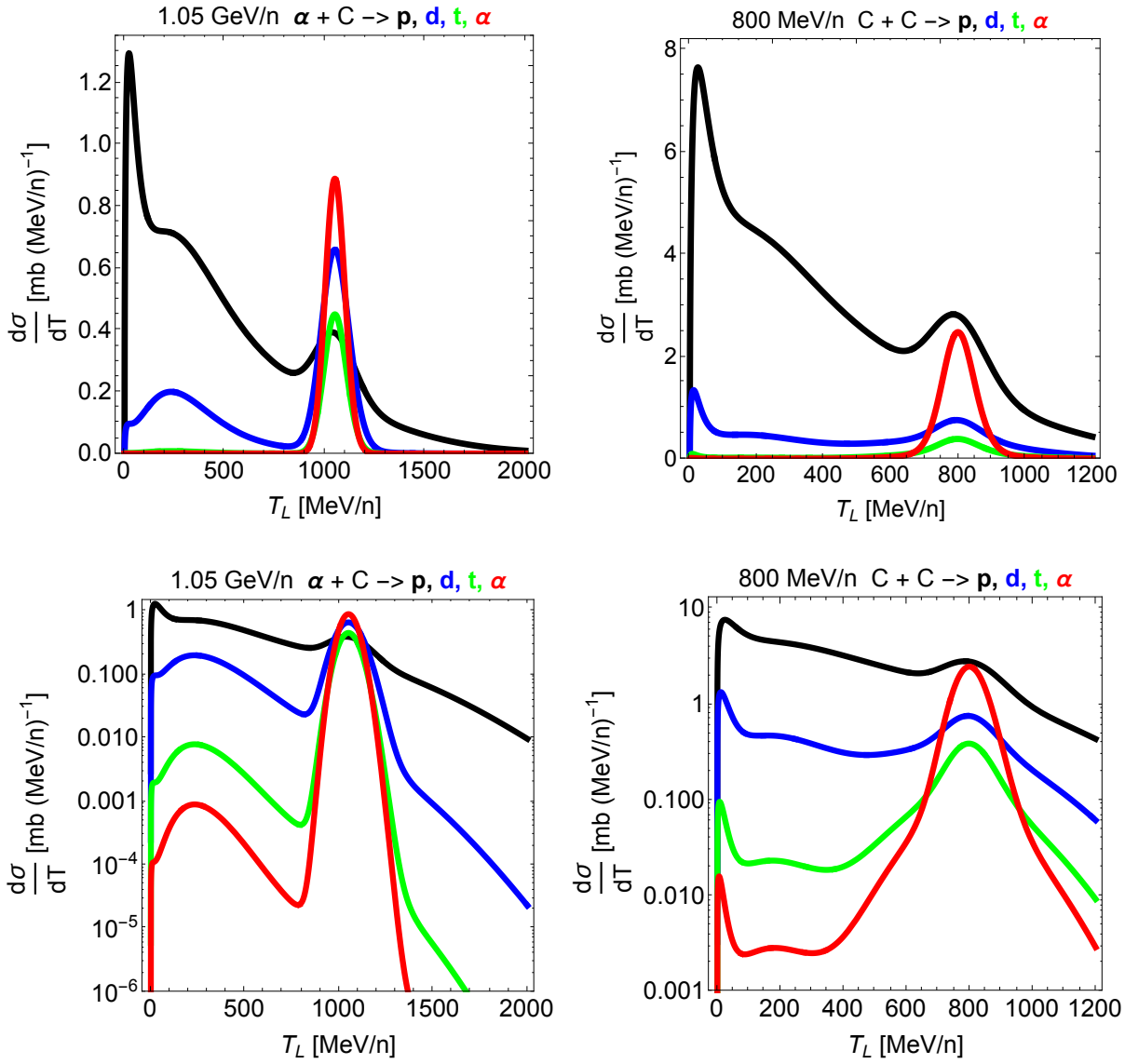

Figure 47: Linear (upper panel) and logarithmic (lower panel) lab frame spectral distributions for light ion production calculated for α + C reactions at 1.05 GeV/n and C + C reactions at 800 MeV/n.

References

[1] J.W. Norbury, T.C. Slaba, Life Sci. Space Res. 3 (2014) 90.

[2] S.A. Walker, L.W. Townsend, J.W. Norbury, Adv. Space Res. 51 (2013) 1792.

[3] J.W. Norbury, T.C. Slaba, N. Sobolevsky, B. Reddell, Life Sci. Space Res. 14 (2017) 64.

[4] J.W. Norbury, N., Sobolevsky, C.M. Werneth, Nucl. Instr. Meth. Phys. Res. B 418 (2018) 13.

[5] D. Matthia, et al., J. Space Weath. Space Clim. 6 (2016) A13.

[6] J.W. Wilson, T.C. Slaba, F.F. Badavi, B.D. Reddell, A.A. Bahadori, Life Sci. Space Res. 2 (2014) 6.

[7] J.W. Wilson, T.C. Slaba, F.F. Badavi, B.D. Reddell, A.A. Bahadori, Life Sci. Space Res. 4 (2015) 46.

[8] J.W. Wilson, T.C. Slaba, F.F. Badavi, B.D. Reddell, A.A. Bahadori, Life Sci. Space Res. 7 (2015) 27.

[9] J.W. Wilson, T.C. Slaba, F.F. Badavi, B.D. Reddell, A.A. Bahadori, Life Sci. Space Res. 9 (2016) 69.

[10] T.C. Slaba, J.W. Wilson, F.F. Badavi, B.D. Reddell, A.A. Bahadori, Life Sci. Space Res. 9 (2016) 77.

[11] J.W. Norbury, L. Latysheva, N. Sobolevsky, Nucl. Instr. Meth. Phys. Res. A 947 (2019) 162576.

[12] J.W. Norbury, NASA Technical Publication 2018-220077.

[13] S. Nagamiya, M.C. Lemaire, E. Moeller, S. Schnetzer, G. Shapiro, H. Steiner, I. Tanihata, Phys. Rev. C 24 (1981) 971.

[14] M.C. Lemaire, S. Nagamiya, O. Chamberlain, G. Shapiro, S. Schnetzer, H. Steiner, I. Tanihata, Lawrence Berkeley Laboratory report number LBL-8463, 1978.

[15] T. Nakamura, L. Heilbronn, Handbook on secondary particle production and transport by high-energy heavy ions, World Scientific, Singapore, 2006.

[16] L. Anderson, W. Bruckner, E. Moeller, S. Nagamiya, S. Nissen-Meyer, L. Schroeder, G. Shapiro, H. Steiner, Phys. Rev. C 28 (1983) 1224.

[17] T.C. Slaba, S.R. Blattnig, Space Weather 12 (2014) 217.

[18] M.R. Spiegel, Mathematical Handbook, Schaum's Outline Series, McGraw-Hill, New York, 1968.

[19] A.S. Goldhaber, Phys. Lett. B 53 (1974) 306.

[20] A.S. Goldhaber, H.H. Heckman, Ann. Rev. Nucl. Part. Sci. 28 (1978) 161.

[21] H. Feshbach, K. Huang, Phys. Lett. B 47 (1973) 300.

[22] Y. Iwata, T. Murakami, H. Sato, H. Iwase, T. Nakamura, T. Kurosawa, L. Heilbronn, R.M. Ronningen, K. Ieki, Y. Tozawa, K. Niita, Phys. Rev. C 64 (2001) 054609.

[23] T.C. Awes, G. Poggi, S. Saini, C.K. Gelbke, R. Legrain, G.D. Westfall, Phys. Lett. B 103 (1981) 417.

[24] B.A. Remington, G. Caskey, A. Galonsky, C.K. Gelbke, L. Heilbronn, J. Heltsley, M.B. Tsang, F. Deak, A. Kiss, Z. Seres, J. Kasagi, J.J. Kolata, Phys. Rev. C 34 (1986) 1685.

[25] H.R. Schelin, A. Galonsky, C.K. Gelbke, H. Hama, L. Heilbronn, D. Krofcheck, W. Lynch, D. Sackett, M.B. Tsang, X. Yang, F. Deak, A. Horvath, A. Kiss, Z. Seres, J. Kasagi, T. Murakami, Nucl. Sci. Eng. 113 (1993) 184.

[26] T. Kato, T. Kurosawa, T. Nakamura, Nucl. Instr. Meth. Phys. Res. A 480 (2002) 571.

[27] R.L. Auble, Phys. Rev. C 28 (1983) 1552.

[28] A.M. Adamczyk, R.B. Norman, S. Sriprisan, L.W. Townsend, J.W. Norbury, S.R. Blattnig, T.C. Slaba, Nucl. Instr. Meth. Phys. Res. A 678 (2012) 21.

[29] C.M. Werneth, X. Xu, R.B. Norman, K.M. Maung, Nucl. Instr. Meth. Phys. Res. B 413 (2017) 75.

[30] J.W. Norbury, F. Dick, NASA Technical Publication 2008-215543.

[31] J.W. Norbury, Nucl. Instr. Meth. Phys. Res. A 703 (2013) 220.

[32] F.A. Cucinotta, M. Kim, S. Schneider, D. Hassler, Rad. Environ. Biophys. 46 (2007) 101.

[33] L. Heilbronn et al., to be published.

[34] D.M. Hassler, J.W. Norbury, G. Reitz, Life Sci. Space Res. 14 (2017) 1.

[35] D. Matthia et al., Life Sci. Space Res. 14 (2017) 18.

[36] T.C. Slaba, S.R. Blattnig, F.F Badavi, N.N. Stoffle, R.D. Rutledge, K.T. Lee, E.N. Zapp, Ts.P. Dachev, B.T. Tomov, Adv. Space Res. 47 (2011) 600.

[37] T.C. Slaba, S.R. Blattnig, B. Reddell, A. Bahadori, R.B. Norman, F.F. Badavi, Adv. Space Res. 52 (2013) 62.

[38] M. Beach, L. Castellanos, M. Clowdsley, L. Heilbronn, C. La Tessa, N. McGirl, J.W. Norbury, M. Sivertz, A. Srikrishna, H. Ratliff, A. Rusek, H. Wang, C. Zeitlin, Nucl. Instr. Meth. Phys. Res. B (submitted).

[39] T. Sato, K. Niita, N. Matsuda, S. Hashimotot, Y. Iwamoto, S. Noda, T. Ogawa, H. Iwase, H. Nakashima, T. Fukahori, K. Okunura, T. Kai, S. Chiba, T. Furuta, L. Sihver, J. Nucl. Sci. Tech. 50 (2013) 913.

[40] J.W. Norbury, J. Miller, A.M. Adamczyk, L.H. Heilbronn, L.W. Townsend, S.R. Blattnig, R.B. Norman, S.B. Guetersloh, C.J. Zeitlin, Rad. Meas. 47 (2012) 315.

[41] S.R. Blattnig, S.R. Swaminathan, A.T. Kruger, M. Ngom, J.W. Norbury, Phys. Rev. D 62 (2000) 094030.

[42] J.W. Norbury, L.W. Townsend, Phys. Rev. D 75 (2007) 034001.

[43] J.W. Norbury, Phys. Rev. C 79 (2009) 037901.

[44] J.W. Norbury, A.M. Adamczyk, Nucl. Instr. Meth. Phys. Res. B 254 (2007) 177.

[45] J.W. Norbury, S.R. Blattnig, R. Norman, R.K. Tripathi, NASA Technical Publication 2002-211766.

[46] J.P. Schneider, J.W. Norbury, F.A. Cucinotta, NASA Technical Memorandum 4675, 1995.

[47] J.W. Norbury, Phys. Rev. C 79 (2009) 037901; ibid. 83 (2011) 059903(E).

[48] C.M. Werneth, J.W. Norbury, S.R. Blattnig, Nucl. Instr. Meth. Phys. Res. B 298 (2013) 86.

REPORT DOCUMENTATION PAGE

Form Approved
OMB No. 0704-0188

1. REPORT DATE *(DD-MM-YYYY)*	2. REPORT TYPE	3. DATES COVERED *(From - To)*
1-05-2020	Technical Publication	

4. TITLE AND SUBTITLE

Double-Differential FRaGmentation (DDFRG) Models for Proton and Light Ion Production in High Energy Nuclear Collisions Valid for Both Small and Large Angles

5a. CONTRACT NUMBER

5b. GRANT NUMBER

5c. PROGRAM ELEMENT NUMBER

6. AUTHOR(S)

Norbury, John W.

5d. PROJECT NUMBER

5e. TASK NUMBER

5f. WORK UNIT NUMBER

651549.01.07.01

7. PERFORMING ORGANIZATION NAME(S) AND ADDRESS(ES)

NASA Langley Research Center
Hampton, VA 23681-2199

8. PERFORMING O ORGANIZATION REPORT NUMBER

9. SPONSORING/MONITORING AGENCY NAME(S) AND ADDRESS(ES)

National Aeronautics and Space Administration
Washington, DC 20546-0001

10. SPONSOR/MONITOR'S ACRONYM(S)

NASA

11. SPONSOR/MONITOR'S REPORT NUMBER(S)

NASA-TP-2020-5001740

12. DISTRIBUTION/AVAILABILITY STATEMENT

Unclassified-
Subject Category
Availability: NASA STI Program (757) 864-9658

13. SUPPLEMENTARY NOTES

14. ABSTRACT

A new set of Double-Differential FRaGmentation (DDFRG) models for pro-ton and light ion production from high energy nucleus-nucleus collisions, rel-evant to space radiation, is introduced. The proton model employs thermalproduction from the projectile, central fireball and target sources, as well asquasi-elastic direct knockout production. The light ion model uses a hybridcoalescence model. The data show a prominent quasi-elastic peak at small an-gles which becomes highly suppressed at large angles. The models are able todescribe this wide range of experimental data with only a limited set of modelparameters. Closed-form analytic formulas for double-differential energy andangle cross-sections as well as single-differential spectral cross-sections are de-veloped. These analytic formulas enable highly efficient computation for spaceradiation transport codes.

15. SUBJECT TERMS

16. SECURITY CLASSIFICATION OF:			17. LIMITATION OF ABSTRACT	18. NUMBER OF PAGES	19a. NAME OF RESPONSIBLE PERSON
a. REPORT	b. ABSTRACT	c. THIS PAGE			STI Help Desk (email: help@sti.nasa.gov)
U	U	U	UU	112	19b. TELEPHONE NUMBER *(Include area code)* (757) 864-9658